Control of innate olfactory valence by segregated cortical amygdala circuits

James R. Howe[1,2,3,9], Chung-Lung Chan[1,9], Donghyung Lee[1], Marlon Blanquart[1], Haylie K. Romero[2,3,4], Abigail N. Zadina[5,†], Mackenzie E. Lemieux[6], Fergil Mills[6,††], Paula A. Desplats[3,4,7], Kay M. Tye[1,6,8], & Cory M. Root[1,*]

[1] Department of Biological Sciences, Section of Neuroscience, University of California, San Diego, La Jolla, CA 92093, USA

[2] Neurosciences Graduate Program, University of California, San Diego, La Jolla, CA 92093, USA

[3] Department of Neurosciences, University of California, San Diego, La Jolla, CA 92093, USA

[4] Center for Circadian Biology, University of California, San Diego, La Jolla, CA 92093, USA

[5] Zuckerman Mind Brain Behavior Institute, Columbia University, New York, NY, 10027, USA

[6] Salk Institute for Biological Sciences, La Jolla, CA 92037, USA

[7] Department of Pathology, University of California, San Diego, La Jolla, CA 92093, USA

[8] Howard Hughes Medical Institute, La Jolla, CA 92037, USA

[9] These authors contributed equally

† Current affiliation: Department of Neuroscience and Behavior, Barnard College of Columbia University, New York City, NY 10027, USA

†† Current affiliation: Department of Neurobiology, University of Utah School of Medicine, Salt Lake City, UT 84112, USA

* To whom correspondence should be addressed:

Cory M. Root, PhD
University of California, San Diego
9500 Gilman Drive
3119 Pacific Hall
La Jolla, CA 92093-0357
cmroot@ucsd.edu

SUMMARY

Animals perform innate behaviors that are stereotyped responses to specific evolutionarily relevant stimuli in the absence of prior learning or experience. These behaviors can be reduced to an axis of valence, whereby specific odors evoke approach or avoidance. The cortical amygdala (plCoA) mediates innate attraction and aversion to odor. However, little is known about how this brain area gives rise to behaviors of opposing motivational valence. Here, we sought to define the circuit features of plCoA that give rise to innate olfactory behaviors of valence. We characterized the physiology, gene expression, and projections of this structure, identifying a divergent, topographic organization that selectively controls innate attraction and avoidance to odor. First, we examined odor-evoked responses in these areas and found sparse encoding of odor identity, but not valence. We next considered a topographic organization and found that optogenetic stimulation of the anterior and posterior domains of plCoA elicits attraction and avoidance, respectively, suggesting a functional axis for valence. Using single cell and spatial RNA sequencing, we identified the molecular cell types in plCoA, revealing an anteroposterior gradient in cell types, whereby anterior glutamatergic neurons preferentially express *Slc17a6* and posterior neurons express *Slc17a7*. Activation of these respective cell types recapitulates appetitive and aversive valence behaviors, and chemogenetic inhibition reveals partial necessity for valence responses to innate appetitive or aversive odors. Finally, we identified topographically organized circuits defined by projections, whereby anterior neurons preferentially project to medial amygdala, and posterior neurons preferentially project to nucleus accumbens, which are respectively sufficient and necessary for innate negative and positive olfactory valence. Together, these data advance our understanding of how the olfactory system generates stereotypic, hardwired attraction and avoidance, and supports a model whereby distinct, topographically distributed plCoA populations direct innate olfactory valence responses by signaling to divergent valence-specific targets, linking upstream olfactory identity to downstream valence behaviors, through a population code. This represents a novel circuit motif in which valence encoding is represented not by the firing properties of individual neurons, but by population level identity encoding that is routed through divergent targets to mediate distinct valence.

INTRODUCTION

Innate behaviors are ubiquitous across the animal kingdom, allowing specific sensory stimuli to yield stereotypical behavioral responses even in the absence of learning or past experience. These behaviors include feeding, fighting, fleeing, and mating, among others, and many can be simplified onto an axis of positive or negative valence representing approach and avoidance. Innate behaviors are the result of evolutionary selection, guiding initial behaviors that can be updated by future experiences. Given that innate behaviors are genetically hardwired, it is thought they should be mediated by simple circuits with specified connections between layers of the nervous system. Innate behaviors are common across sensory modalities but are especially prominent in olfaction, whereby diverse chemical signals, critical to survival and reproduction, must be quickly and robustly detected and processed, in the absence of prior experience. For instance, predator odors represent a potentially imminent threat and necessitate a quick, decisive, aversive response.[1] Conversely, innately appetitive odors represent potentially rewarding stimuli like food or heterospecifics, inducing attraction.[2–4] These odors comprise a small subset of perceptible chemical space, and the detection of specific odorants is both species-specific and under genetic control.[5–7]

Valence is a fundamental perceptual feature of olfaction. Motivational valence can be defined as seeking or avoiding specific stimuli, and it is observed across sensory stimuli in both innate and learned responses. Multiple circuit motifs have been proposed to mediate such valence responses.[8] In the simplest form, labeled line motifs segregate information from sensation to action throughout the nervous system. This has been observed in the taste and somatosensory systems, as well as hints of labeled lines in the olfactory system, where individual glomeruli are necessary and sufficient for innate responses consistent with this model.[9–11] Many circuits are organized along divergent path motifs, where a region receives the same sensory input but instead acts akin to a switchboard, processing and sorting its output to distinct downstream targets to convey positive or negative signals. This motif is most associated with the BLA and associated learning processes.[8,12] Still other circuits contain opposing components motifs, in which opposing inputs target a single effector region to control the balance of one target. It remains unclear which, if any, of these generalized circuit motifs are present in the olfactory system.

Olfactory sensation begins with olfactory sensory neurons (OSNs) in the olfactory epithelium (OE) that express a single receptor, projecting to spatially stereotyped glomeruli in the olfactory bulb (OB). Postsynaptic mitral/tufted cells within the OB project in parallel to third-order olfactory areas, including the posterolateral cortical amygdala (plCoA). Unlike in other third-order olfactory areas, such as piriform cortex, projections from individual glomeruli from the OB to plCoA are spatially restricted and stereotyped, consistent with genetically hardwired circuits.[13–16] Past work has demonstrated that plCoA is necessary and sufficient for innate olfactory responses, with spatially ordered labeling of responsive neurons via immediate early gene labeling.[3] However, other work suggests that there is no spatial organization to odor responses or valence encoding in plCoA.[17] Thus, a further investigation of plCoA organization is necessary to understand how this structure controls innate olfactory responses.

Distinct brain areas employ distinct coding strategies to represent information. Neuronal ensembles within all other major olfactory regions observed thus far, such as the anterior olfactory nucleus, OB, OE, olfactory tubercle (OT), piriform cortex (PIR), and tenia tecta all generally perform sparse population encoding of odor identity, despite the major differences in neuronal composition, organization, and function between the six regions.[12,17–30] On the other hand, ensembles within amygdala subnuclei, most notably the basolateral amygdala (BLA), instead tend to represent the valence of stimuli instead, with considerable heterogeneity based on a given population's projection target, molecular identity, and topography.[12,18,19] A complete investigation of the encoding properties and organization of plCoA is needed to determine how innate olfactory valence emerges from this region.

To identify the plCoA circuitry that underlies innate valence, we investigated multiple intersecting scales of organization, from single cell transcriptomes and spatial gene expression, to circuit mapping, manipulation, and physiology. First, we used 2-photon calcium imaging to find that plCoA ensembles encode odor identity, but not valence. Next, we identify a functional gradient in plCoA where activation of anterior and posterior neurons drives responses of opposing valence. Next, we characterized the cell types within plCoA, identifying novel, molecularly defined populations specific to each domain of plCoA, which are respectively sufficient and partially necessary for innate olfactory valence. Further, we perform comprehensive projection mapping to identify downstream projection targets of plCoA, identifying projections to the medial amygdala (MeA) and nucleus accumbens (NAc) that are enriched based on molecular and topographic identity. Finally, manipulations of neuronal ensembles projecting to these targets are sufficient and necessary to control innate olfactory valence responses. Together, these findings identify a novel topographically distributed circuit from plCoA to MeA and NAc that controls innate olfactory aversion and attraction, respectively, consistent with a hybrid model mixing features of labeled lines and divergent path circuit motifs.

RESULTS

Population Encoding of Odor Identity in plCoA

To better understand how plCoA circuitry mediates innate olfactory valence, we first decided to examine the relationship between its spatial organization and odor-evoked activity. Prior analysis of immediate early gene expression following minutes-long odor exposure suggests that activity in the anterior and posterior domains of plCoA could respectively mediate innate aversive and appetitive odor responses.[3] However, *in vivo* electrophysiology with high-density electrode arrays found no evidence for spatial organization or valence encoding in plCoA.[17] These two studies propose contradictory models of plCoA encoding properties that are both plausible, given that the former is common in the extended amygdala and insular cortex, and the latter is ubiquitous across olfactory regions.[22,31,32] We speculated that technical differences could be responsible for these opposing findings. Immediate early gene labeling has extremely low temporal resolution and likely requires a high amount of neural activity to activate gene expression. On the other hand, the recording sites in the latter study appear biased towards the middle of plCoA, and odor was given for 2 seconds in interleaved trials, whereas olfactory valence behavior evolves on a minutes-long timescale.[3,33] We wondered if the apparent contradictions in these studies could be resolved by applying a longer odor delivery protocol that both matches the timescale of behavior and balances spatial and temporal resolution.

Therefore, we developed an approach to image neural activity in plCoA with a modified odor delivery schedule, expressing GCamP8s targeted towards either the anterior or posterior subsection of plCoA and implanting a gradient-index relay (GRIN) lens above to allow *in vivo* imaging of calcium transients via head-fixed two-photon microscopy (**Figure 1A-C, S1A-B**). We then examined calcium responses in these mice during a long odor exposure, where odors were presented repeatedly in 20-trial blocks for 5 seconds each in counterbalanced order (**Figure 1D**). We chose two odorants of each innate valence: the appetitive odors 2-phenylethanol (2PE) and peanut oil (PEA), the neutral odors heptanol (HEP) and isoamyl acetate (IAA), and the aversive odors trimethylthiazoline (TMT) and 4-methylthiazoline (4MT).[3,17] In total, we recorded Ca^{2+} signals from 345 neurons across 13 mice.

First, we pooled anterior and posterior plCoA neurons together and performed hierarchical clustering of their trial-averaged responses to the 6 odors to categorize odor responses in an unbiased manner (**Figure 1E**). Consistent with the previous *in vivo* electrophysiology study, we found that the majority of plCoA neurons did not seem to selectively respond to odors of one valence group (**Figure 1E-F**). Across mice, a majority of plCoA neurons did not reliably respond to any of the six odors, and activity was sparse: only 34.5% of plCoA neurons responded to 1 of the 6 odors and 10% to 2 odors, while a much smaller portion of plCoA neurons responded to 3 or more odors (**Figure 1G**). Further, we found no significant relationship between the valence of odor and proportion of responsive neurons, and no difference in the proportion responsive to the different odors across anterior and posterior plCoA, suggesting a lack of bias in responsiveness to aversive or appetitive odors across the anterior-posterior axis (**Figure 1H, S1C**).

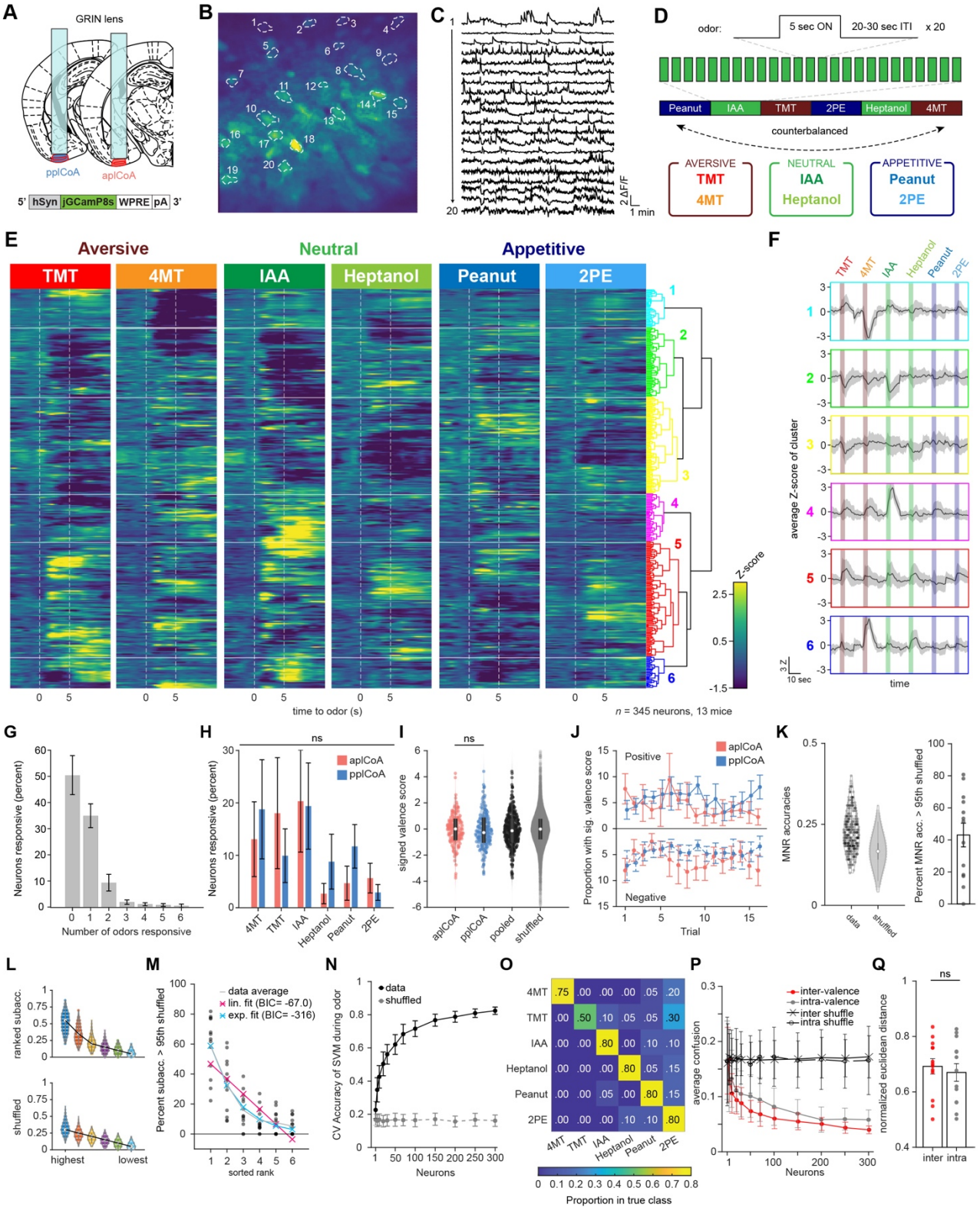

Figure 1. The plCoA encodes innately-valenced odor identity using a population code.

(A) Schematic representation of virus injection and GRIN lens implantation into aplCoA or pplCoA for two-photon microscopy.
(B-C) Representative images (**B**) and traces (**C**) of fluorescence changes in individual neurons over an approximately 20-minute period.
(D) Schematic of odor exposure paradigm. Each trial presented 5 seconds of odor followed by a variable inter-trial interval (20-30s). Odors were present in blocks of 20 trials per odor, with 2 counterbalanced block schedules (1 & 2). Six odors were used: the appetitive odors 2-phenylethanol (2PE) and peanut oil (PEA), the neutral odors heptanol (HEP) and isoamyl acetate (IAA), and the aversive odors trimethylthiazoline (TMT) and 4-methylthiazoline (4MT).
(E) Heatmap of trial-averaged and Z-scored odor-evoked activity over time from pooled plCoA neurons. Responses are grouped by hierarchical clustering, with the dendrogram (right). Odor delivery marked by vertical red lines.
(F) Average of trial-averaged and Z-scored odor-evoked activity for each cluster concatenated. The order of color-coded blocks corresponds to the order of clusters in (**E**).
(G) Proportion of neurons responsive to different numbers of odors. Bars represent the mean across 13 animals and the error bars show SEM.
(H) Proportion responsive to each odor for aplCoA (red) or pplCoA (blue).
(I) Valence scores of individual neurons. White circles show the median of each distribution, whereas the gray rectangle shows the 25th-75th percentile range.
(J) Proportion of neurons with significant valence scores calculated as a function of trial number. Calculated with a 10-trial moving window. Top half shows those with significant positive valence scores, the bottom half shows those with significant negative valence scores.
(K) Left, MNR accuracies for all pooled plCoA neurons (data) and a control distribution where the training labels are shuffled (shuffled) in a violin plot. Right, proportion of neurons in each animal that have MNR accuracy greater than the 95th percentile of the shuffled MNRs.
(**L**) Ranked sub-accuracies for single-neuron MNR classifiers in violin plots for those trained on real (top) or shuffled (bottom) data. Black lines connect the median across each rank.
(**M**) Scatter plot of percentage of sub-accuracies above the 95th percentile of the shuffled controls for each animal plotted against the rank of the sub-accuracy. Red and blue lines show the linear and exponential fit, respectively, and a gray dashed line connects data averages.
(**N**) Cross-validated average accuracies of multinomial SVM's plotted as a function of the number of neurons used for training during the odor period. Circles represent the mean across 100 iterations of random sampling of neurons and error bars show the standard deviation.
(**O**) An example confusion matrix for a multinomial SVM trained with 200 neurons.
(P) Comparison of inter-valence and intra-valence confusion across number of neurons used in training the classifiers. Filled circles show the average of the data across 100 iterations, open circles show shuffled controls.
(Q) The normalized average distance between odor pairs that have different valence (inter) or same valence (intra).
Across panels, ns, not significant. Additional specific details of statistical tests can be found in Supplemental Table 1.

We next attempted to quantify valence encoding by calculating a valence score for each neuron by subtracting the average integrated aversive odor response from the average integrated appetitive odor response and dividing this resulting difference in valence by the integrated odor response ($V = \frac{\Sigma_{appetitive} - \Sigma_{aversive}}{\Sigma_{total}}$). Although the valence score was more negatively skewed amongst anterior neurons than posterior ones, there was no significant difference in their distributions, failing to support a model in which anterior and posterior plCoA neurons broadly encode opposing innate olfactory valence (**Figure 1I**). Given that the innate aversive and appetitive behaviors evolve over time in freely moving animals, we wanted to assess if odor responses changed between early and late trials. Using a moving window of 5 trials, we examined if the proportion of neurons with significant aversive or appetitive valence scores differed over time in anterior or posterior plCoA but found no significant interaction between time and imaging location (**Figure 1J**).

We further investigated odor encoding at the single neuron level using multinomial regression (MNR) 6-odor classifiers trained on single neuron data and found that they perform only marginally better than chance, indicating that the majority of single plCoA neurons do not broadly encode discriminatory information about odor identity (**Figure 1K**). Across mice, only 43.1% have overall classification rates above the 95th percentile of shuffled controls, indicating that the majority of single plCoA neurons do not broadly encode discriminatory information about odor identity. Interestingly, when comparing the ranked sub-accuracies for single odors compared to shuffled controls, we found the discrepancy between data and shuffled controls to be accentuated in the 2 highest performing sub-accuracies (**Figure 1L**). Quantifying the proportion of neurons with sub-accuracies higher than the 95th percentile of the shuffled across biological replicates, we found that the decrease of sub-accuracies down the rank falls exponentially, rather than linearly (**Figure 1M**). This, paired with the observation that most plCoA neurons respond to one or none of the six odors tested, indicates that individual plCoA neurons are sparsely responsive and carry little information about identity or valence.

Surprisingly, we saw no evidence of valence encoding at the single neuron level in either the anterior or posterior plCoA. Instead, the plCoA neurons appear to primarily encode odor identity in a sparse manner much like the other higher-order olfactory areas, known to use a population code. Thus, we next considered identity and valence encoding at the population level. In contrast to the poor single neuron classification, SVMs trained on population-level data vastly outperform the shuffled data, indicating good encoding of identity at the population level (**Figure 1N**). We further used a confusion matrix to ask whether training the classifier with a given odor could accurately predict the identity of another odor. In the matrix each column corresponds to a predicted class and each column corresponds to the actual class (**Figure 1O**). If the population level activity is similar between odor pairs, we expect the confusion to be higher than less similar pairs. The output of a confusion matrix yields a proportion of true class labels, whereby a high proportion indicates good prediction. We found no difference between the confusion rates for intra-valence classification or inter-valence classification, suggesting a lack of valence encoding at the population level (**Figure 1P**). The similarity between inter-valence and intra-valence confusion was mirrored when quantifying the range-normalized pairwise Euclidean distance across biological replicates (**Figure 1Q, S1D**). Thus, plCoA

appears to encode odor identity in a population code like other higher order olfactory regions, with no apparent encoding of valence.

A Functional Axis for Valence in plCoA

Since we did not observe clear evidence for valence encoding, we considered other organizational principles that could support behaviors of opposing valence. Spatial organization for valence processing has been previously observed in the insular cortex and BLA, whereby discrete subsections of the region contain neurons wired to preferentially signal positive or negative valence.[18,19,34,35] Given plCoA's spatially-ordered afferent projections from OB, we next hypothesized that plCoA circuitry could still be organized along the anterior-posterior (AP) axis to generate innate olfactory valence. If true, it follows that activation of small ensembles of neurons along the AP axis should generate behavioral responses along a corresponding axis of valence. We tested this prediction by expressing channelrhodopsin (ChR2) in subsets of neurons at different positions along this axis and photostimulating them during behavioral testing in the previously established four-quadrant open field arena.[3]

Based on cytoarchitecture, we more formally parcellated plCoA into three domains: the anterior plCoA (aplCoA), a two-layered region on the ventral surface lateral to the anterior cortical amygdala, the posterior plCoA (pplCoA), a three-layered region on the ventrolateral surface lateral to the posteromedial cortical amygdala, and a middle transition zone (mplCoA) between them (**Figure 2A**).[3,36] To determine the potential relationship between position on the anterior-posterior axis of plCoA and evoked valence, we performed optogenetic stimulation at points along this entire axis, expressing channelrhodopsin (ChR2) and implanting fibers into each zone (**Figures 2B-C, S2A**). Valence using the four-quadrant open field assay, where mice freely explored a chamber with or without stimulation, and valence was scored with a performance index measuring quadrant occupancy relative to chance, as well as the mean distance to the corner port. Mice experience a 10 minute baseline period followed by 15 minutes of closed loop optogenetic (470nm, increasing up to a maximum of 10 Hz as the mouse proceeds closer to the corner port) stimulation in one quadrant (**Figure 2D**).[3]

Throughout the trial period, we observed a negative linear relationship between the anterior-posterior position of the photostimulation site and the evoked change in performance index and distance to the corner port in ChR2, but not eYFP-infected mice, where evoked valence shifted from positive to negative as stimulation became more anterior. (**Figure 2E-F**). We grouped these responses to determine whether these bidirectional responses were specific to the identified plCoA zones. We found that photostimulation in aplCoA significantly reduced time spent in the 'on' quadrant and increased the average distance to the corner port during the treatment period, indicating activation of aplCoA neurons is aversive and leads to avoidance of the quadrant paired with stimulation (**Figure 2G-I**). We also found the opposite was true in pplCoA, where stimulation in that zone instead increased the time in the 'on' quadrant and decreased average distance to the corner port, indicating pplCoA neuron activation instead is appetitive and leads to attraction to the stimulation quadrant (**Figure 2J-L**).

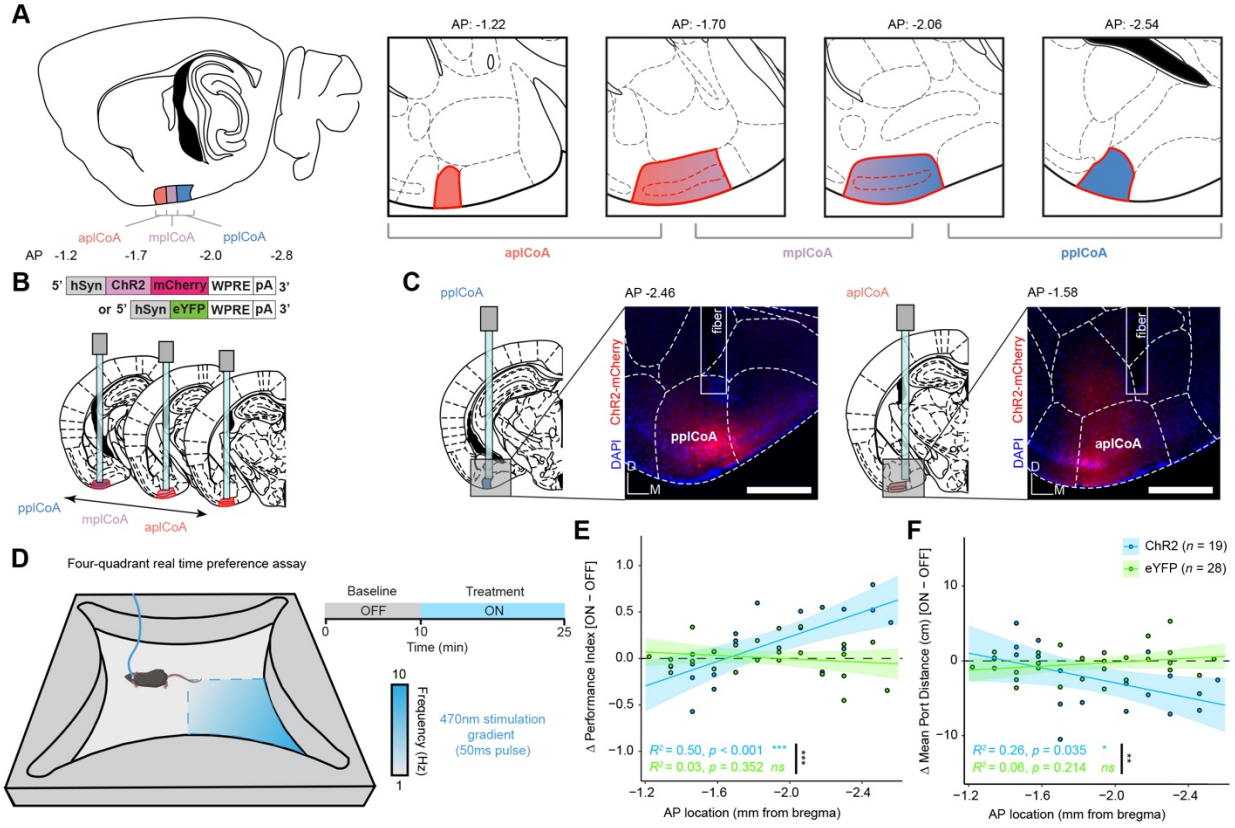

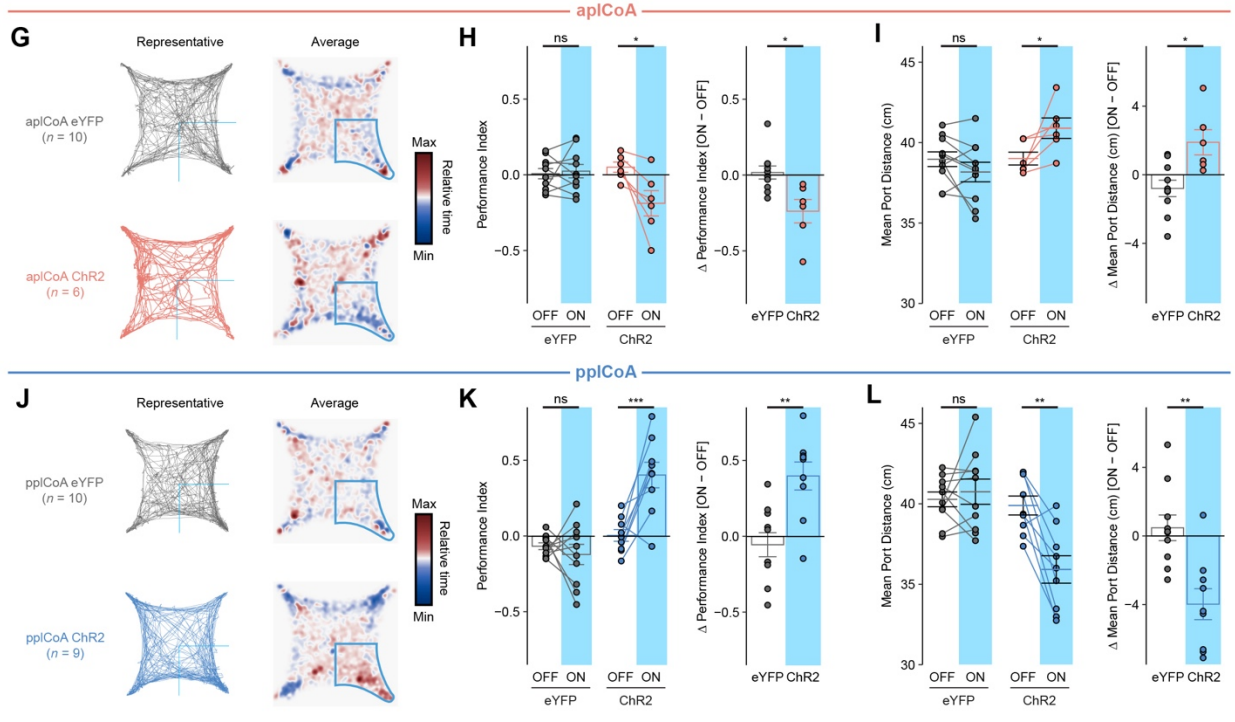

Fig. 2. The plCoA has topographic organization capable of driving approach and avoidance behaviors.

(A) Schematic of plCoA domains divided into anterior (aplCoA), middle (mplCoA), and posterior (pplCoA) regions based on histology, positioning, and gradients observed in past observations.[3,15]
(B) Strategy to activate anterior-posterior topographical ensembles via optogenetics.
(**C**) Representative histology and fiber/virus placement for aplCoA and pplCoA ChR2 animals.
(**D**) Schematic of four-quadrant open field behavioral assay with closed-loop photostimulation.
(E-F) Linear-fit of change in performance index (**E**) or mean port distance (**F**) as a function of anterior-posterior position along plCoA for optical stimulation.
(G) Paths traveled during the stimulus period for a representative mouse (left) and baseline-normalized collective heatmaps (right) from both the ChR2- and eYFP-infected groups with aplCoA-localized fiber implants. Lower right stimulus quadrant indicated in blue.
(H-I) Mean effect of Photostimulation of aplCoA neurons on time spent in stimulated quadrant (performance index) (**K**) and distance from the corner (port distance) (**I**).
(J) Paths traveled during the treatment period for a representative mouse (left) and baseline-normalized collective heatmaps (right) from both the ChR2- and eYFP-infected groups with pplCoA-localized fiber implants. Lower right stimulus quadrant marked in blue.
(**K-L**) Mean effect of photostimulation of pplCoA neurons infected with ChR2, but not eYFP, is sufficient to increase time spent in the stimulation quadrant (**K**) and reduce its average distance from the stimulation port during the stimulation period (**L**).
Abbreviations: aplCoA, anterior zone of posterolateral cortical amygdala; mplCoA, middle zone of posterolateral cortical amygdala; pplCoA, posterior zone of posterolateral cortical amygdala.
Across panels, ns, not significant; * $p < 0.05$; ** $p < 0.01$; *** $p < 0.001$. Specific details of statistical tests can be found in Supplemental Table 1.

We further examined the effects of anterior-posterior plCoA stimulation on other behaviors to determine whether these effects were specific to valence, or if they extended to other affective or motor phenomena. Using the elevated plus maze, we found no change in anxiety based on open arm time or entries, across both the length of plCoA or within either aplCoA or pplCoA (**Figure S3A-C, S3E-F, S3H-I**). In the open field test, we similarly found no changes to thigmotaxis, based on time spent in corners of the open field, or exploration, based on time spent in the center of the open field (**Figure S3K-M, S3EO-P, S3R-S**). Further, locomotion remained constant during stimulation across both assays and the entirety of plCoA (**Figure S3D, S3G, S3J, S3N, S3Q, S3T**). Together, these data indicate that the effects of plCoA neuron activation across the entire anterior-posterior axis are specific to valence, with few other behavioral effects. Overall, we find activation of plCoA neurons is sufficient to drive valence behaviors in a topographically organized and bidirectional manner, where aplCoA drives aversion and pplCoA drives attraction.

Molecular Diversity of Transcriptomic plCoA Cell Types Along the Anteroposterior Axis

Having identified a functional axis sufficient to produce valence behaviors (**Figure 2**) that does not appear to encode valence (**Figure 1**), we next considered if the plCoA could be topographically organized by molecular cell type to support behaviors of opposing valence. Thus, we sought to determine if there is an axis of molecular cell types along the anteroposterior domains of plCoA. To investigate this phenomenon, we performed single-nucleus RNA sequencing (snRNA-seq) to determine the cell type composition and its relationship to the anterior-posterior axis of plCoA.[37] To simultaneously profile these cell types and identify domain-specific patterns, we separately extracted tissue samples from aplCoA and pplCoA by microdissection, verified accurate dissection by histology, and pooled qualifying samples from the selected plCoA domain for each sequencing run (**Figure 3A, S4A-D**). We also confirmed there were few region- or batch-specific differences in sequencing depth or nuclear quality markers (**Figure S4E-M**). Clustering of sequenced nuclei by gene expression allowed us to initially identify all major canonical neuronal and glial cell types in plCoA based on known marker genes identified in past scRNA-seq studies (**Figure 3B-C**).[38,39] Neurons in plCoA are 80% glutamatergic, while 20% of neurons are GABAergic (**Figure 3D**). We also identified large numbers of vascular leptomeningeal cells (VLMCs) and arachnoid barrier cells (ABCs), two fibroblast-like meningeal cell types that interface with vasculature and form a barrier between the brain and CSF, likely due to meningeal presence on the cortical surface during extraction.[39–41]

We further characterized the heterogeneity of glutamatergic and GABAergic neurons within plCoA by re-processing and subclustering both major neuronal cell types. Within glutamatergic neurons, we identified 14 distinct subtypes by gene expression, with largely continuous variation between glutamatergic subtypes (**Figure 3E**). However, when examining the relationships between these subtypes, we identified two broader groups of glutamatergic neurons via hierarchical clustering, where subtypes within each group displayed a lower Euclidean distance from one another in high-dimensional gene expression space (**Figure 3F**).

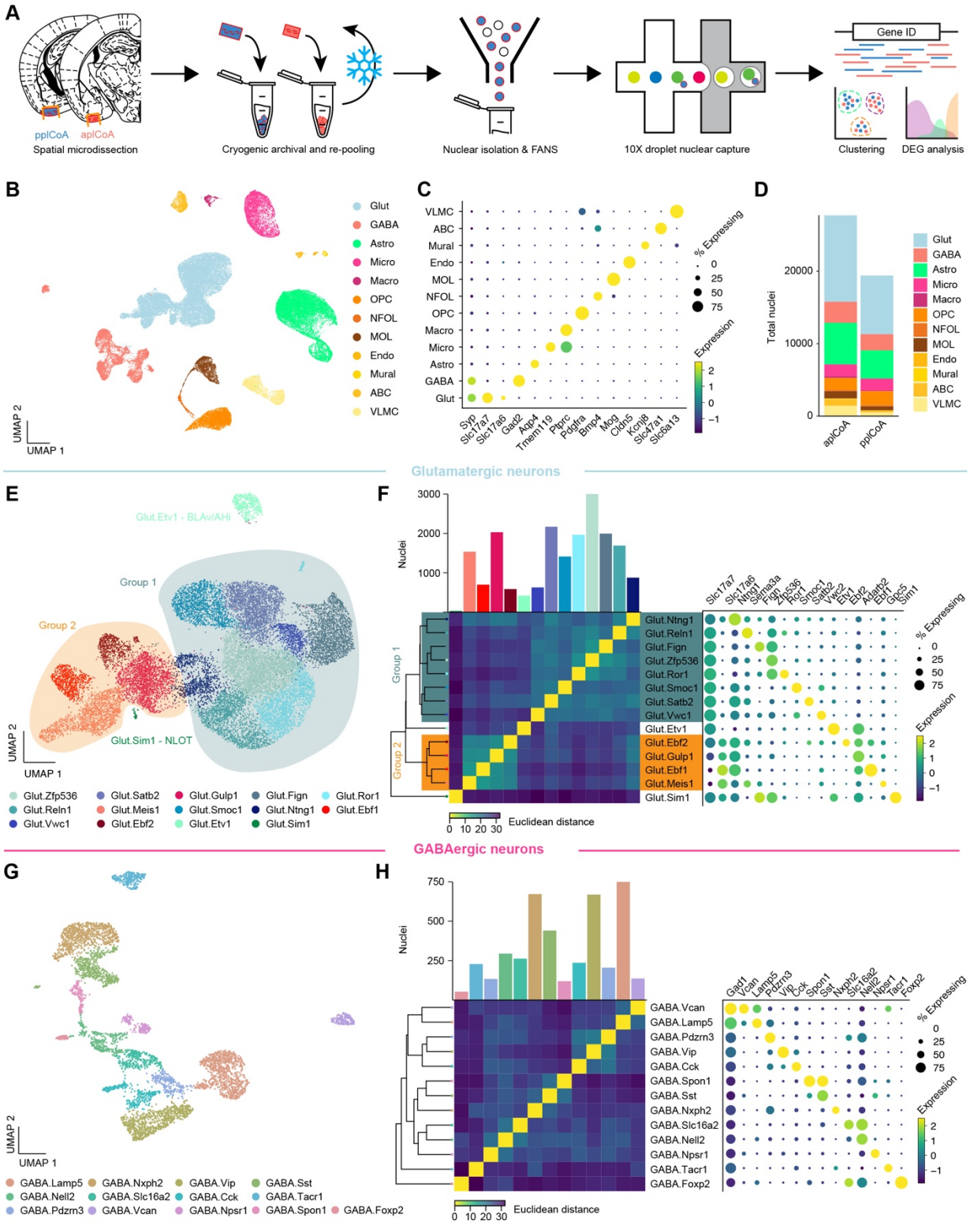

Fig. 3. Transcriptomic heterogeneity of plCoA molecular cell types.

(A) Schematic of freeze and-re-pool strategy for snRNA-seq.
(B) Two-dimensional UMAP (n = 47,132 nuclei, see also **Figure S4.3**), colored by broad cellular identity assigned by graph-based clustering of neuronal and non-neuronal nuclei.
(**C**) Cell-type-specific expression of canonical marker genes indicating broad cellular identity in the brain. Dot size is proportional to percentage of nuclei expressing the marker, with color scale representing normalized expression level.
(**D**) Total proportion of cells of each identified type in each domain of plCoA.
(E) Two-dimensional UMAP of glutamatergic neurons, colored by molecular cell type.
(F) Clustered heatmap showing Euclidean distance between averages of each subtype positioned based on hierarchical clustering (left), and dot plot of marker genes for all glutamatergic subtypes (right).
(G) Two-dimensional UMAP of GABAergic neurons, colored by molecular cell type, like in (**E**).
(H) Clustered heatmap showing Euclidean distance between averages of each subtype positioned based on hierarchical clustering (left), and dot plot of marker genes for all GABAergic subtypes (right), like in (**F**).

Each of these two broader groups had a marker for every type within either group, where the larger Group 1 of glutamatergic neurons express *Slc17a7 (VGLUT1)*, and the smaller Group 2 expresses *Slc17a6 (VGLUT2)*. Within each of these glutamatergic groups, most observed marker genes are non-canonical in the amygdala and cortex, suggesting unique glutamatergic ensembles or patterns of gene expression within glutamatergic neurons in plCoA compared to other regions previously described. Two subtypes did fall outside of either broad glutamatergic group, varying in a more discrete manner than most plCoA glutamatergic neuron subtypes. Interestingly, examination of data from the Allen ISH Atlas for their respective marker genes *Etv1* and *Sim1* showed these two groups fall into adjacent regions outside of plCoA, where Glut.Etv1 neurons localize to the posterior basomedial amygdala and Glut.Sim1 neurons localize to the nucleus of the lateral olfactory tract (**Figure S5A-B**). However, gene expression patterns for GABAergic neurons displayed an opposing form of heterogeneity, where subtypes are far more discrete, without broad groups linking related subtypes (**Figure 3G**). Marker genes for GABAergic neurons are also more canonical than those in glutamatergic neurons, whereby most GABAergic neurons in plCoA have interneuron-like identities, expressing canonical marker genes such as *Vip, Sst,* and *Cck* (**Figure 3H**).

We hypothesized that differences in these populations' abundance could potentially be responsible for the difference observed between different plCoA domains, and thus examined potential domain-specific enrichment of certain cell types within plCoA. Visualization of these nuclei showed little clear region-specific structure in dimension-reduced space for any major cell types (**Figure 4A**). This lack of structure was broadly confirmed quantitatively, where a few low-abundance glial cell types showed significant domain-specific enrichment, but the high-abundance major cell types did not (**Figure 4A-B**). When looking to other regions, however, heterogeneity is usually more pronounced between subsets of the major cell types, instead of by the quantities of the major cell types themselves.[42,43] We then examined abundance of differentially expressed genes (DEGs) between plCoA domains for each major cell type. Here, we found that both major neuronal cell types had more abundant DEGs than all major glial cell types (**Figure 4C**). Glutamatergic neurons DEGs exceeded all other major cell types by a factor of 4, making it likely that differences between the anterior and posterior domains are most likely to be observed via variation in glutamatergic neurons.

Upon examination of domain-specific variation in plCoA glutamatergic neurons, we initially observed a greater degree of domain-specific clustering in dimension-reduced space (**Figure 4D**). Glutamatergic neuron subtypes correspondingly displayed domain-specific enrichment, where more than half of glutamatergic neuron subtypes were significantly enriched in either the anterior or posterior plCoA domain (**Figure 4E**). Upon closer examination, we found that every glutamatergic subtype in the *Slc17a6*-expressing Group 1 was enriched in anterior plCoA, while *Slc17a7*-expressing Group 2 subtypes are evenly distributed across fields or biased towards the posterior, with one exception, Glut.Fign, which likely derives from the aplCoA-adjacent cortex-amygdala transition area CxA, based on Allen ISH data of *Fign* expression (**Figures 4F, S5A**). In contrast to glutamatergic neurons, we did not observe significant plCoA domain-specific variation for any GABAergic neuron subtypes (**Figure S5D-E**). We also found additional heterogeneity within glial cell types, including additional subtypes in

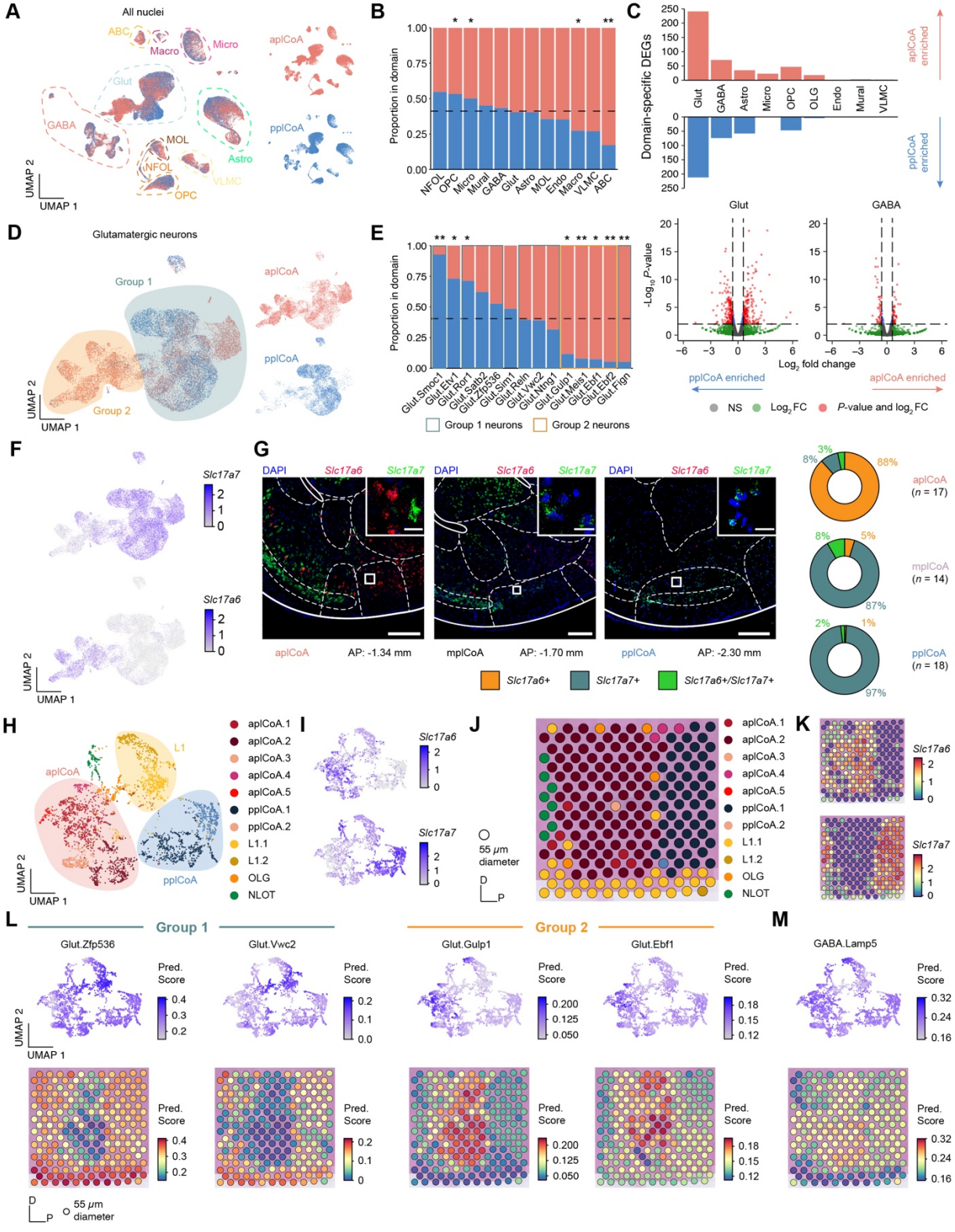

Fig. 4. Glutamatergic neurons subtypes in plCoA are spatially distributed along an anteroposterior molecular gradient.

(**A**) UMAP of all plCoA nuclei colored by zone of origin, with dotted outlines and labels denoting the major cell types.
(**B**) Relative proportion of nuclei from each domain within each broad identity class. Dotted line indicates chance level for all plCoA nuclei.
(**C**) Top, abundance of domain-specific DEGs for each major cell type, either enriched in aplCoA nuclei (top) or pplCoA nuclei (bottom). Bottom, volcano plots for domain-specific DEGs for glutamatergic (left) and GABAergic neurons (right), the two cell types with the greatest degree of domain specific gene expression, where negative log-fold changes indicate enrichment in pplCoA and positive log-fold changes indicate enrichment in aplCoA.
(**D**) UMAP of plCoA glutamatergic neurons colored by domain of origin, with dotted outlines and labels denoting the subtypes on the graph. Groups of glutamatergic neuron types identified previously via Euclidean distance and hierarchical clustering are overlaid on top of the neuron types of interest.
(**E**) Relative proportion of molecular subtypes from each domain within glutamatergic neurons, where relevant subtypes are outlined according to their glutamatergic neuron group. Dotted line indicates chance level for plCoA glutamatergic neuron nuclei.
(**F**) UMAP of all glutamatergic neuron nuclei, colored by expression levels of *Slc17a6* (top) or *Slc17a7* (bottom).
(**G**) Left, representative images of *in situ* RNAscope labeling of *Slc17a6* RNA (red) and *Slc17a7* RNA (green) across plCoA domains. Right, proportions of glutamatergic neurons expressing *Slc17a6, Slc17a7,* or both. Scale bars, 500 μm (main image), 50 μm (inset).
(**H**) UMAP of all plCoA-overlapping Visium capture spots, colored by cluster. Broad spatial position of groups of clusters are overlaid on top of the capture spots of interest.
(**I**) UMAP of all plCoA-overlapping Visium capture spots, colored by expression levels of *Slc17a6* (top) or *Slc17a7* (bottom).
(**J**) Representative plCoA-overlapping region of one section on a Visium slide capture area, with capture spots colored by cluster.
(**K**) Representative plCoA-overlapping region of one section on a Visium slide capture area, with capture spots colored by expression levels of *Slc17a6* (top) or *Slc17a7* (bottom).
(**L**) Prediction scores for representative glutamatergic neuron subtypes within Group 1 (left) and Group 2 (right), shown on a UMAP of all plCoA-overlapping capture spots across all sections (top) and on a representative plCoA-overlapping region of one section (bottom).
(**M**) Prediction scores for a representative GABAergic neuron subtype, shown on a UMAP of all plCoA-overlapping capture spots across all sections (top) and on a representative plCoA-overlapping region of one section (bottom).
Across panels: * $p < 0.05$; ** $p < 0.01$; *** $p < 0.001$; ns, not significant. Additional specific details of statistical tests can be found in Supplemental Table 1.

astrocytes and VLMCs (**Figure S5G-J, O-R**). We also observed high-dimensional domain-specific divergence in gene expression for OPCs and astrocytes corresponding to domain-specific DEG differences, though they did not correspond to any observable differences in subtype enrichment (**Figure S5F, K-N**).

To confirm these findings and validate our snRNA-seq data, we directly examined spatial RNA expression patterns. First, we used RNAscope labelling to examine the expression of *Slc17a6* and *Slc17a7 in situ* in the plCoA, quantifying the number of nuclei expressing these genes. We found that anterior plCoA had a much greater proportion of RNAscope-labelled *Slc17a6*+ nuclei (88%) than *Slc17a7*+ nuclei (11%) compared to the rest of plCoA, where *Slc17a7*+ neurons predominate; posterior plCoA nuclei were almost entirely *Slc17a7*+ (97%) expressing (**Figure 4G**). It is noteworthy that these numbers were generally consistent with those in our sequencing data. Next, we analyzed spatial gene expression in the plCoA from an existing Visium spatial transcriptomics dataset that contained sagittal sections bisecting the plCoA along the midline (Romero et al., in preparation; **Figure S5S**). We asked if the domain-specific molecular cell type composition can be recovered directly from spatial information, without depending on inference from dissection histology. All sections used were of similarly high quality and did not display any clearly observable batch effects, with all but one having more than 100 spots covering the plCoA (**Figure S5T-W**). When clustering directly on spatial data, we observed significant heterogeneity separating into three broad groups (**Figure 4H**). Like in scRNA-seq, we found highly specific expression of *Slc17a6* and *Slc17a7* to two of the three broad spot groups (**Figure 4I**). When examining the spatial configuration of these groups, we found the *Slc17a6*-expressing group of clusters was in aplCoA, while the *Slc17a7*-expressing group was in pplCoA**,** with the third intermediate group corresponding to layer 1 (**Figure 4J-K**). When computationally projecting transcriptomic cell type identities onto spatial data, we observed that Group 1 glutamatergic neuron types would project onto pplCoA spots and Group 2 glutamatergic neuron types would project onto aplCoA spots, while negligible anteroposterior bias could be observed when projecting GABAergic neuron types onto plCoA spots (**Figure 4L-M**). Overall, these data demonstrate that plCoA contains an extremely diverse population of numerous glutamatergic and GABAergic neuron subtypes, whereas glutamatergic neuron subtypes vary significantly along the anteroposterior axis, such that aplCoA-enriched subtypes express *Slc17a6* and pplCoA-enriched subtypes express *Slc17a7.*

Molecularly Defined plCoA Glutamatergic Neuron Populations Are Sufficient to Drive Valence Behavior

Given this spatial distribution bias of plCoA$^{Slc17a6+}$ neurons into aplCoA and plCoA$^{Slc17a7+}$ neurons into pplCoA, we further hypothesized that these glutamatergic neuron subtypes could be responsible for the opposing valence responses observed during topographic plCoA stimulation (**Figure 2**). If distinct molecular cell types mediate opposing valence, the topography-independent activation should elicit opposing responses. To investigate this, we expressed ChR2 in a non-spatially-biased, cell type-specific manner using a Cre-dependent viral construct in *Slc17a6::Cre* and *Slc17a7::Cre* transgenic mice, targeting AAV-DIO-hSyn-ChR2 into mplCoA and implanting optic fibers above the injection site (**Figures 5A-B, S2B**).[44,45] Using the prior four-quadrant open field task, we found that photostimulation of plCoA$^{Slc17a6+}$

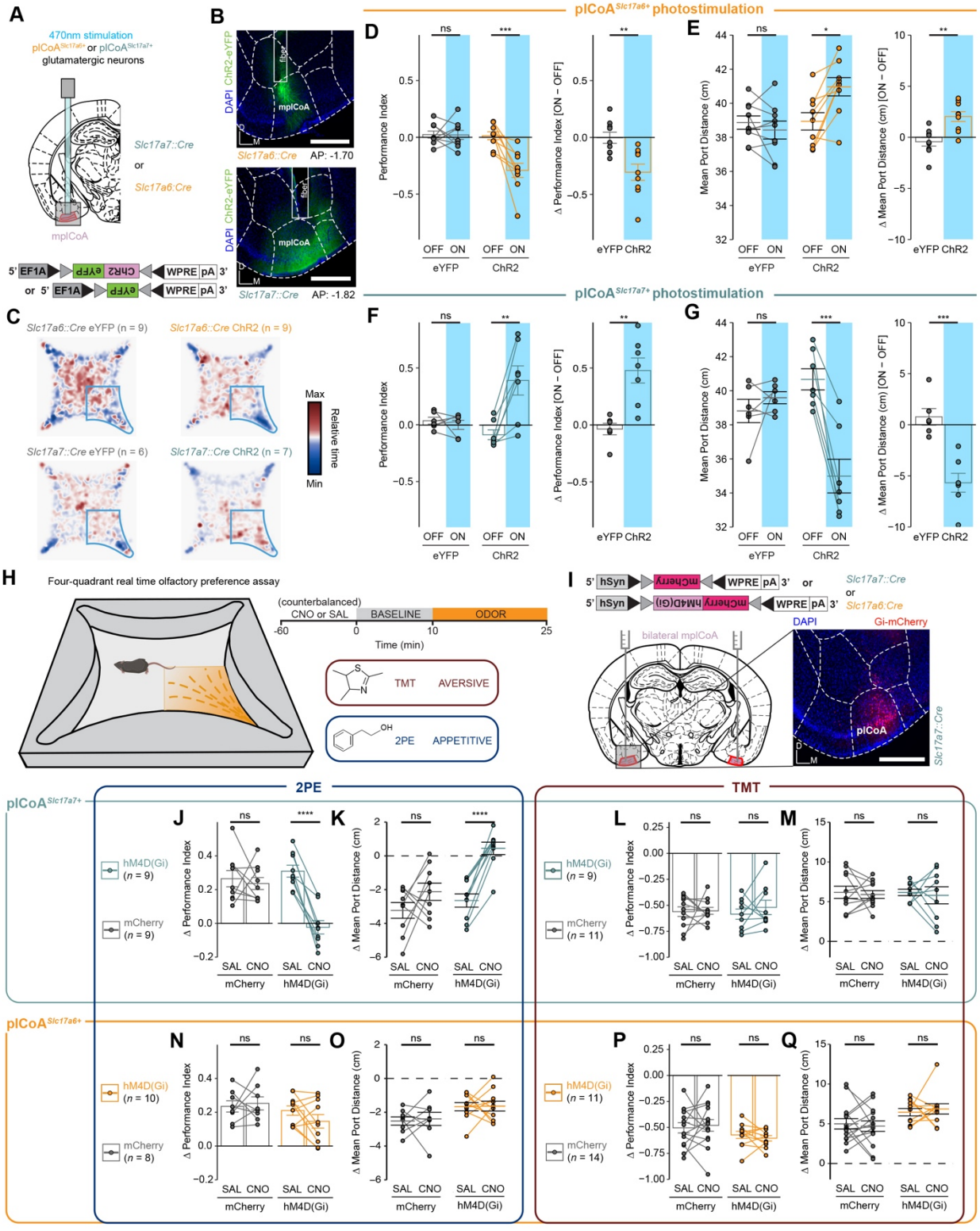

Fig. 5. Glutamatergic plCoA$^{Slc17a6+}$ and plCoA$^{Slc17a7+}$ neurons contribute to innate olfactory behaviors of opposing valence.

(**A**) Schematic for selective photostimulation of distinct glutamatergic cell type. *Slc17a6::Cre* and *Slc17a7::Cre* animals were injected with Cre-dependent viral vectors into mplCoA with a fiber optic implant placed just above the injection site.
(**B**) Representative histology from ChR2 viral injection and fiber implantation site in an *Slc17a6::Cre* animal (top) and an *Slc17a7::Cre* animal (bottom).
(**C**) Baseline-normalized collective heatmaps from both the ChR2- and eYFP-infected groups in *Slc17a6::Cre* and *Slc17a7::Cre* animals with plCoA-localized fiber implants. Lower right stimulus quadrant marked in blue.
(D-G) Effect of photostimulation of plCoA$^{Slc17a6+}$ neurons (**D-E**) or plCoA$^{Slc17a7+}$ neurons (**F-G**) on time spent in the stimulation quadrant (**D, F**) and distance from the corner (**E, G**).
(**H**) Behavioral paradigm to assess innate valence responses to odor. Left, schematic of four-quadrant open field behavioral assay for spatially-specific odor delivery. Upper right, within-trial timeline. Lower right, odors delivered and their associated innate valence.[3]
(**I**) Schematic of strategy for selective chemoinhibition of molecularly defined glutamatergic plCoA neurons.
(**J-M**) Effect of chemoinhibition of plCoA $^{Slc17a7+}$ neurons on time spent in the odor quadrant (**J, L)** or decrease in mean port distance (**K, M**) in response to 2PE (**J-K**) or TMT (**L-M**)**.**
(**N-Q**) Effect of chemoinhibition of plCoA $^{Slc17a6+}$ neurons on time spent in the odor quadrant (**N, P)** or decrease in mean port distance (**O, Q**) in response to 2PE (**N-O**) or TMT (**P-Q**)**.**
Across panels, ns, not significant; * $p < 0.05$; ** $p < 0.01$; *** $p < 0.001$, **** $p < 0.0001$.
Additional specific details of statistical tests can be found in Supplemental Table 1.

neurons significantly reduced time spent in the 'on' quadrant and increased the average distance to the corner port during the treatment period , indicating activation of plCoA$^{Slc17a6+}$ neurons is aversive and leads to avoidance of the quadrant when paired with stimulation (**Figure 5C-E**). In contrast, photostimulation of the plCoA$^{Slc17a7+}$ neurons instead increased the time in the 'on' quadrant and decreased average distance to the corner port, indicating plCoA$^{Slc17a7+}$ neuron activation instead is appetitive and leads to attraction to the stimulation quadrant (**Figure 5C,F-G**). These data indicate that the divergent domain-specific valence effects of plCoA activity are likely due to the divergent molecularly defined neuronal ensembles predominant in each topographical field of plCoA.

Next, we sought to determine whether these two glutamatergic populations are respectively required for innate olfactory aversion and/or attraction. We used the above transgenic mouse lines to drive expression of a viral Cre-dependent hM4D(Gi) construct to selectively inhibit these neurons' activity via chemogenetics (**Figure 5I, Figure S6A-C**).[46] We administered clozapine-N-oxide (CNO) or a vehicle control and used the four-quadrant open field assay to deliver odorants in a quadrant-specific manner to assess their behavioral responses to the innately-attractive 2PE or the innately-aversive TMT to determine the difference in the magnitude of temporally-counterbalanced valence responses when the respective populations are chemogenetically silenced.[3]

We observed that while both transgenic mouse lines preserved the baseline attraction and aversion to both 2PE and TMT following administration of the vehicle control, silencing plCoA$^{Slc17a6+}$ neurons did not affect the response to either odorant (**Figure 5J-Q**). However, silencing plCoA$^{Slc17a7+}$ neurons abolished the positive valence response to 2PE, without having any effect on TMT-evoked aversion (**Figure 5J-Q**). In other words, neither group of plCoA glutamatergic neurons are necessary for TMT aversion, but plCoA$^{Slc17a7+}$ neurons are required for expression of 2PE attraction behaviors. Further, silencing of either population did not lead to any broader non-olfactory behavior effects as measured by the EPM and OFT assays, including anxiety, exploration, and motility, showing the effects of silencing these neurons are likely limited to valence and/or olfaction alone, instead of exploratory or defensive behaviors (**Figure S5C-N**). The necessity of plCoA$^{Slc17a7+}$ neurons for 2PE attraction, combined with their ability to drive positive valence responses indicates that these of plCoA$^{Slc17a7+}$ neurons control innate olfactory attraction, but plCoA$^{Slc17a6+}$ neurons do not completely control innate olfactory aversion, instead proving sufficient but not necessary.

A Topographic Organization of plCoA Defined by Limbic Projection Targets

While comprehensively characterizing the circuit features of plCoA, we noted that the anatomical connectivity of the plCoA has not yet been defined in the mouse brain. Further, we posited that the differences in necessity of plCoA cell types could be due to divergent downstream connections instead of divergent molecular features, which may partially, but not completely overlap. Thus, we next sought to identify distinct downstream outputs of plCoA that could explain the bidirectional valence effects of its topography. We first characterized the downstream outputs of plCoA by co-injecting the anterograde viral tracer AAV-DIO-hSyn-mRuby2-T2A-synaptophysin-EGFP and a constitutive AAV-Cre virus into mplCoA to label

presynaptic terminals with EGFP (**Figure S7A-B**). We observed a high amount of terminal fluorescence within plCoA itself, suggesting the presence of recurrent connections within the region (**Figure S6B**). In addition, we observed long-range projections to a diverse set of regions, including surrounding extended amygdala subregions, such as MeA and the amygdalo-hippocampal transition area (AHi), regions controlling valence and emotion, like the NAc and the bed nucleus of the stria terminalis (BNST), and regions involved in olfactory processing, primarily PIR and OT (**Figure 6A-D**).

Among these outputs, we hypothesized that the NAc and the MeA could be responsible for the behavioral divergence between anterior and posterior plCoA, given their known involvement in reward expectation and aversion, respectively.[47,48] We sought to confirm these differences using retrograde tracing from MeA or NAc, where red retrobeads were injected into MeA or NAc and labeled neurons were quantified along the anterior-posterior axis (**Figure 6E**). For both downstream targets, we observed opposing gradients of retrobead projector labeling throughout the entire plCoA anteroposterior axis (**Figure 6F**). MeA-projecting neurons are enriched in aplCoA, and NAc-projecting neurons are enriched in pplCoA, with each having a frequency of around chance level in mplCoA (**Figure 6G**). Further, the majority of labeled plCoA-MeA projection neurons were in aplCoA, while the majority of labeled plCoA-NAc projection neurons were in pplCoA (**Figure 6H**). To further confirm the spatial bias in projection targets, we performed anterograde tracing from the aplCoA and pplCoA by injecting viruses expressing either eYFP or mCherry into either domain of plCoA in a counterbalanced manner (**Figure S6D-E**). Anterograde projection strength from aplCoA and pplCoA revealed that projections to MeA were most dense from aplCoA, and projections to NAc were most dense from pplCoA (**Figure 6I-K**). Proportionally, aplCoA sent a significantly higher proportion of its projections to MeA than pplCoA, whereas pplCoA sent a significantly higher proportion of its projections to NAc (**Figure 6L**).

We reasoned that the topographical valence sufficiency we observed could be explained by cell type-specific divergence in projection target, whereby the topographical biases in downstream targets are recapitulated by their underlying molecular cell type. To determine the relationship between cell types and projection targets, we injected Cre-dependent eYFP into mplCoA in *Slc17a6::Cre* and *Slc17a7::Cre* transgenic mice, targeting the middle to ensure differences result from cell type, instead of simply redundant topography (**Figure S7F-G)**. Interestingly, the relationship was not as simple as one cell type, one primary projection target. Instead, both cell types project to both structures in different proportions. The plCoA$^{Slc17a6+}$ neurons primarily project to MeA with a significant bias for that target over NAc, while plCoA$^{Slc17a7+}$ neurons project to both MeA and NAc, with a statistically insignificant bias toward NAc (**Figure 6M,P**). These findings demonstrate that NAc primarily receives projections plCoA$^{Slc17a7+}$ neurons, whereas the MeA receives input from both populations. Moreover, projection of both cell types to the MeA may explain why neither population was selectively required for innate aversion (**Figure 5J-Q**).

Given that both cell types project to both MeA and NAc, we sought to determine the extent of collateralization in neurons composing the two pathways. To test whether plCoA-MeA and plCoA-NAc projection neurons also project to multiple or overlapping downstream targets,

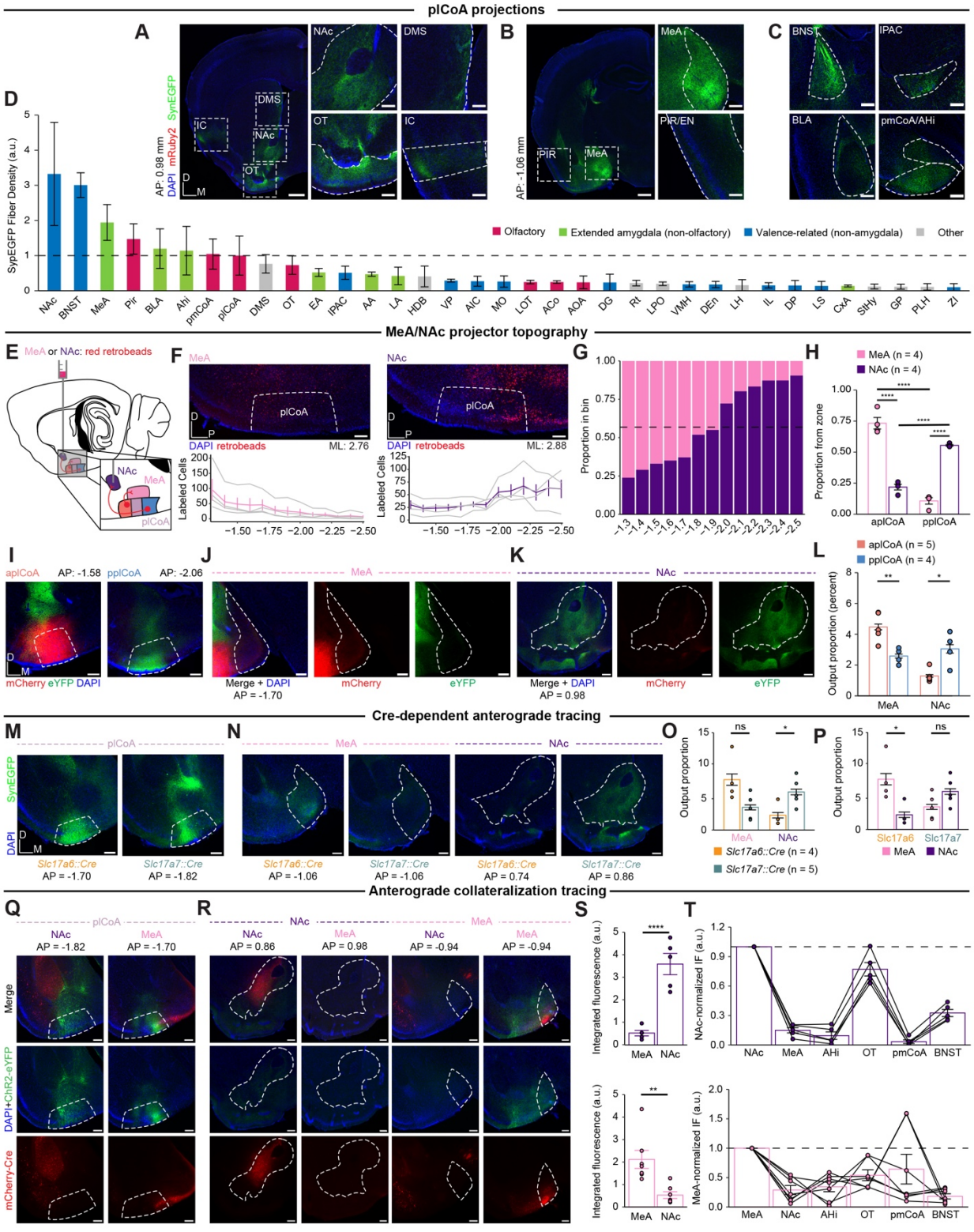

Fig. 6. Projections to MeA and NAc from plCoA are Topographically Organized

(**A**) Right, whole-hemisphere view at AP = 0.98 mm from bregma. Scale bar, 500 μm. Left, Magnified images of the areas highlighted inside white dashed lines. Scale bar, 200 μm.
(**B**) Right, whole-hemisphere view at AP = -1.06 mm from bregma. Scale bar, 500 μm. Left, Magnified images of the areas highlighted inside white dashed lines. Scale bar, 200 μm.
(**C**) Other plCoA projections not found in cross-sections of the brain found in **(A)** and **(B)**. Scale bar, 200 μm.
(**D**) Magnitude of anterograde synaptophysin-eYFP fluorescence in primary downstream targets of plCoA projection neurons ordered by total output strength, colored based on each region's function.
(**E**) Schematic for topographic retrograde mapping strategy from MeA and NAc into plCoA. Red retrobeads are injected into MeA or NAc and topographical projection bias is examined along the anterior-posterior axis.
(**F**) Representative images (top) for injection into MeA (left) or NAc (right) and number of neurons labeled along the anterior-posterior axis as distance (mm) from bregma (bottom). Gray lines denote individual replicates, where colored lines indicate mean ± s.e.m.
(**G**) Proportion of retrobead-labeled neurons projecting to MeA or NAc for each 100 μm segment as a function of distance from bregma. Dashed line indicates overall balance of all retrobead-labeled neurons across entire plCoA.
(**H**) Proportion of retrobead-labeled neurons from either target within each plCoA zone. MeA-labeled neurons are significantly enriched in aplCoA compared to NAc-labeled neurons, while NAc-labeled neurons are significantly enriched in pplCoA compared to those labeled from MeA.
(**I**) Representative histological images for the injection sites in aplCoA (left) and pplCoA (right) from a representative animal. Scale bar, 200 μm.
(**J**) Representative histological images for MeA from the animal in (**J**). Scale bar, 200 μm.
(**K**)**.** Representative histological images for NAc from the animal in (**J**). Scale bar, 200 μm.
(**L**) Output strength as a proportion of total fluorescence from aplCoA and pplCoA to MeA and NAc.
(**M**) Representative histological images for the injection site in plCoA from a representative *Slc17a7::Cre* and *Slc17a6::Cre* animal. Scale bar, 200 μm.
(**N**) Representative histological images from MeA and NAc from a representative animal of either genotype. Scale bar, 200 μm.
(**O**) Left, output strength as a proportion of total fluorescence from plCoA$^{Slc17a6+}$ and plCoA$^{Slc17a7+}$ neurons to MeA and NAc. Right, comparison of same data, but by target region within genotype.
(**P**) Same data as **(O)**, but by target region within genotype.
(**Q-V**) Mapping collateral projections from NAc- and MeA projecting neurons.
(**Q**) Representative histological images for the injection site in plCoA from a representative animal receiving retrograde virus into MeA or NAc. Scale bar, 200 μm.
(**R**) Representative histological images of NAc and MeA retro-Cre targeting (red) and outputs (green).
(**S**) Comparison of absolute integrated fluorescence intensities in MeA and NAc when retroAAV was injected into NAc (top) or MeA (bottom).

(**T**) Quantification of fluorescence in selected downstream brain regions from plCoA originating from plCoA-NAc neurons proportional to eYFP fluorescence in NAc (top) or MeA (bottom). Abbreviations: NAc, nucleus accumbens; BNST, bed nucleus of stria terminalis; MeA, medial amygdala; Pir, piriform cortex; BLA, basolateral amygdala; Ahi, amygdalo-hippocampal transition area; pmCoA, posteromedial cortical amygdala; Str, striatum; OT, olfactory tubercle; EA, extended amygdala; IPAC, inferior peduncle of the anterior commissure; AA, anterior amygdala; LA, lateral amygdala; HDB, horizontal limb of the diagonal band; VP, ventral pallidum; AIC, anterior insular cortex; mfb, medial forebrain bundle; MO, medial orbitofrontal cortex; LOT, lateral olfactory tract; ACo, anterior cortical amygdala; AOA, anterior olfactory area; DG, dentate gyrus; Rt, reticular nucleus; LPO, lateral preoptic area; VMH, ventromedial hypothalamus; DEn, dorsal endopiriform claustrum; LH, lateral hypothalamus; IL, infralimbic cortex; DP, dorsal peduncular cortex; LS, lateral septum; CxA, cortex-amygdala transition area; sox, supraoptic decussation; StHy, striohypothalamic nucleus; GP, globus pallidus; PLH, perirhinal cortex; ZI, zona incerta.
Across panels, ns, not significant; * $p < 0.05$; ** $p < 0.01$; **** $p < 0.0001$. Additional specific details of statistical tests can be found in Supplemental Table 1.

we employed a combination of retrograde Cre and Cre-dependent anterograde tracer viral vectors. A retroAAV-hSyn-Cre-mCherry virus was into either MeA or NAc, and AAV-DIO-ChR2-eYFP was injected into plCoA to label outputs of MeA- or NAc-projecting neurons (**Figure 6Q-R, S7H-I**). We focused on MeA and NAc, as well as the ancillary primary downstream targets implicated in valence or olfaction.[25,49–51] We found different collateralization patterns for both populations, where NAc-projecting neurons did not collateralize to MeA, but very strongly collateralized to OT. In contrast, MeA-projecting neurons minimally collateralized to NAc and most strongly collateralized to pmCoA (**Figure 6S-T**). Notably, neither projection of interest significantly collateralized to the other. These data indicate that plCoA-MeA and plCoA-NAc projection neurons are non-overlapping, spatially biased populations that output to different downstream subnetworks.

Projections from plCoA NAc to MeA and Respectively Control Innate Olfactory Attraction and Aversion to Odor

The topographic separation of MeA- and NAc-projecting neurons are consistent with a model of divergence valence that could support the observed topographic divergence in valence behaviors. To investigate the behavioral contributions of these projections, we first determined whether the neurons projecting to the MeA and NAc are able to drive behavior with optogenetic stimulation. We expressed ChR2 in a non-spatially biased manner by injecting AAV-hSyn-ChR2 into mplCoA, and we placed an optic fiber above MeA or NAc for selective optogenetic stimulation at plCoA axon terminals (**Figure S1C**). We found that photostimulation of the plCoA-MeA circuit in the four-quadrant open field task significantly reduced time spent in the ‘on’ quadrant and increased the average distance to the corner port during the treatment period, indicating activation of the plCoA-MeA circuit is aversive and leads to avoidance of the quadrant paired with stimulation (**Figure 7A-D**). The opposite was true for the plCoA-NAc projection, where stimulation in that zone instead increased the time in the ‘on’ quadrant and decreased average distance to the corner port, indicating activation of the plCoA-NAc circuit is instead appetitive and leads to attraction to the stimulation quadrant (**Figure 7B,E-F**). We next asked if the effects of stimulating these circuits affected other non-valence behaviors by testing the mice in the EPM and OFT. Using the EPM, we found no change in anxiety based on open arm time or entries when stimulating either projection to the MeA or NAc (**Figure S8A-C,E-F,H-I**). Similarly, stimulation in the OFT did not cause any change to thigmotaxis, based on time spent in corners of the open field, or exploration, based on time spent in the center of the open field (**Figure S8K-M,O-P,R-S**). Further, locomotion remained constant during stimulation across both assays (**Figure S8D, S8G, S8J, S8N, S8Q, S8T**). These data indicate that the divergent projections from plCoA to the MeA and the NAc evoke valence-specific behaviors without modulating anxiety.

Finally, we sought to determine whether plCoA-MeA or plCoA-NAc projections are necessary for the expression of odor-evoked appetitive or aversive behaviors. To target these projection neurons for chemogenetic silencing, we injected a retroAAV bearing an hSyn-EBFP-Cre construct into MeA or NAc, along with an AAV in plCoA bearing a Cre-dependent hM4D(Gi) construct (**Figure 7G,H**). We then tested the innate responses of these animals to 2PE or TMT

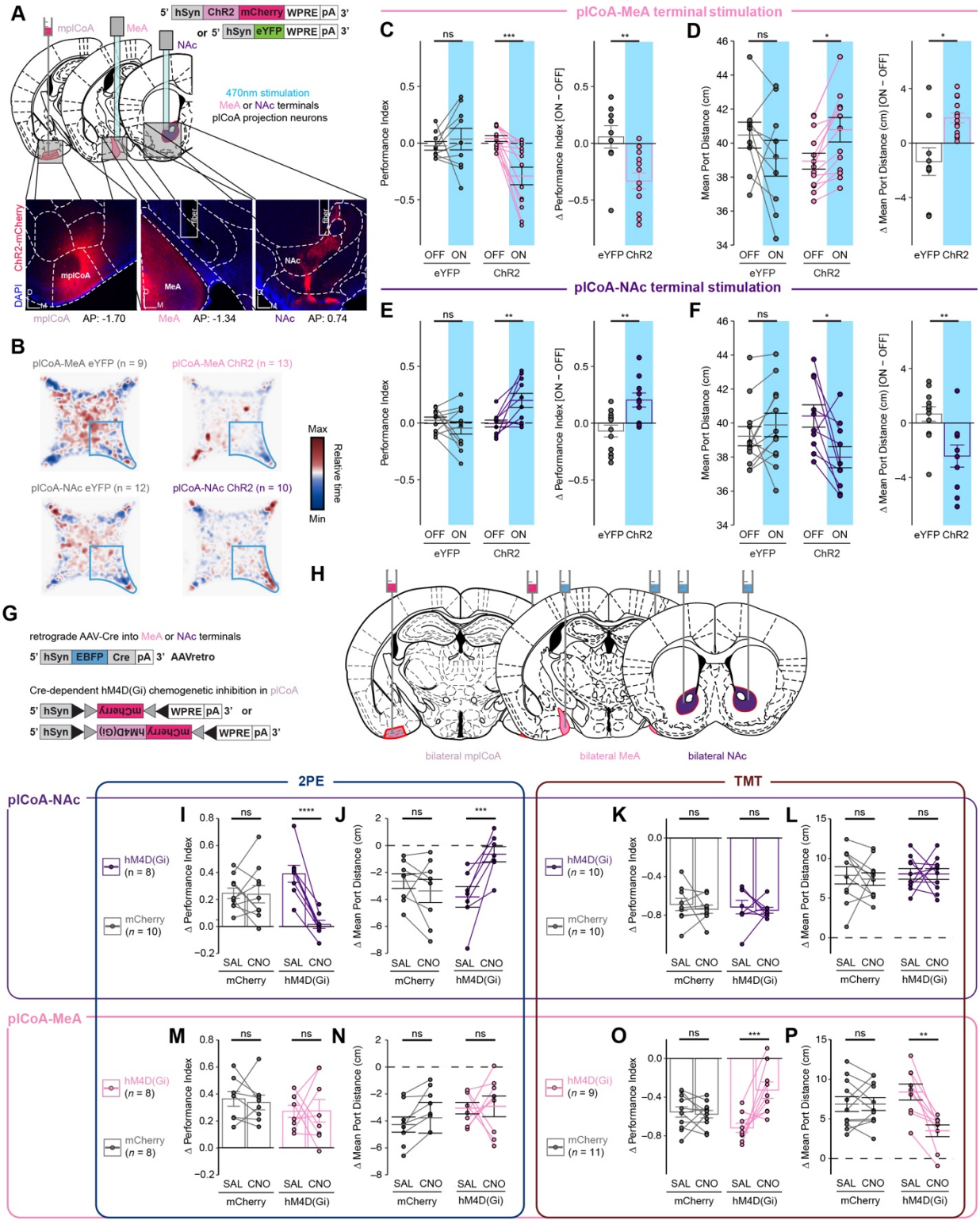

Fig. 7. Projections from plCoA to NAc and MeA control innate olfactory attraction and aversion.

(**A**) Schematic for optogenetic MeA terminal stimulation in plCoA neurons. Strategy to activate MeA-projecting plCoA neuron terminals via optogenetics (top) and representative histology from ChR2 viral injection and fiber implantation site (bottom).
(**B**) Baseline-normalized collective heatmaps from both the ChR2- and eYFP-infected plCoA groups with MeA- and NAc-localized fiber implants. Lower right stimulus quadrant marked in blue.
(C-D) Optogenetic MeA terminal stimulation of plCoA neurons infected with ChR2, but not eYFP, is sufficient to reduce time spent in the stimulation quadrant (**C**) and increase its average distance from the port (**D**) during the stimulation period.
(E-F) Optogenetic NAc terminal stimulation of plCoA neurons infected with ChR2, but not eYFP is sufficient to increase time spent in the stimulation quadrant (**E**) and decrease its average distance from the stimulation port (**F**) during the stimulation period.
(**G**) Viral strategy for selective retrograde chemoinhibition of projection-defined plCoA neurons.
(**H**) Schematic for selective retrograde chemoinhibition of projection-defined plCoA neurons.
(**I-L**) Chemoinhibition of NAc-projecting plCoA neurons significantly eliminates the 2PE-evoked increase in time spent in the odor quadrant (**I)** and decreases in mean port distance (**J).** The response to TMT is unaffected in time spent in odor quadrant (**K**) or port distance (**L**).
(**M-P**) Chemoinhibition of MeA-projecting plCoA neurons does not affect 2PE-evoked increase in time spent in the odor quadrant (**M)** or decrease in mean port distance (**N)** significantly decreases the TMT-evoked reduction in time spent in the odor quadrant (**O)** or increase in mean port distance (**P).**
Across panels, ns, not significant; * $p < 0.05$; ** $p < 0.01$; *** $p < 0.001$. Additional specific details of statistical tests can be found in Supplemental Table 1.

in the four-quadrant assay following administration of CNO or a vehicle control, as above. Inhibition of plCoA-NAc projection neurons abolished innate attraction to 2PE without having any effect on aversion to TMT (**Figure 7I-L**). Conversely, inhibition of plCoA-MeA projection neurons had no effect on innate 2PE attraction, but significantly decreased the aversion to TMT (**Figure 7M-P**). Silencing these neurons had no effect in the EPM and OFT assays, indicating the effects of silencing these neurons are limited to valence or olfaction, and not anxiety or exploration (**Figure S8M-X**). Thus, plCoA-MeA projection neurons are necessary and sufficient for innate olfactory aversion, whereas plCoA-NAc projection neurons are necessary and sufficient for innate olfactory attraction.

DISCUSSION

Topographic Organization of Valence in plCoA

The neural circuits mediating innate valence responses to odor have not been fully defined. Here, we have advanced our knowledge of the circuitry underlying innate olfactory behaviors by defining its activity and organization within plCoA and further extending the innate olfactory pathway from a third order olfactory brain area to limbic structures. We have identified a novel functional axis for valence with the plCoA that is defined by histologically and functionally distinct domains along the anteroposterior axis. We have characterized odor encoding in plCoA, identifying a sparse population code for identity of an odor, but not its innate valence. We have also determined the composition of molecular cell types in plCoA and identified spatially biased populations enriched within each domain, which we find sufficient to drive their respective domain-specific behaviors, though only partially necessary for their functions in olfaction. Moreover, we identified the outputs of plCoA and quantitatively characterized the relative strength of each, as well as how it relates to plCoA topography and domain-specific molecular cell types, demonstrating that neurons projecting to the MeA and NAc are topographically and molecularly biased. Finally, we demonstrate that neurons projecting to the to the NAc and MeA are capable of driving approach and avoidance responses, and loss of function experiments demonstrate that the neurons projecting to the NAc or MeA are selectively involved in innate olfactory attraction and avoidance, respectively. Thus, plCoA is composed of dissociable, spatially segregated ensembles for divergent valence, defined by their downstream projection target.

Spatial organization for features of sensory stimuli is common in sensory cortex, and has been previously proposed as fundamental to sensory processing.[52] Visual cortex is topographically organized by retinotopic locations in space, somatosensory cortex contains a map of the body, auditory cortex has a crude tonotopic organization by frequency, and gustatory cortex is segregated by taste qualities.[34,35,53–55] However, topographic organization by perceptual feature has not been observed in the olfactory system, which has been attributed to the high dimensional nature of olfactory information.[56,57] Our findings identify a topographically organized divergence motif for valence in plCoA, where activation of apICoA evokes aversive behavioral responses, while activation of ppICoA evokes attractive behavioral responses, with a graded transition between the two domains. This is consistent with prior studies implicating a spatial organization to inputs from the OB to plCoA, where glomerulus-specific anterograde tracing from OB shows specific glomeruli send fibers to invariant, densely clustered, anatomically distinct locations within plCoA, and retrograde tracing from plCoA shows that upstream glomeruli are spatially biased within OB and closer examination reveals that OB input can co-vary with plCoA anteroposterior position.[15] Interestingly, spatial segregation of divergent features is present elsewhere in olfaction as well, although not by perceptual feature. Olfactory sensory receptors display stereotyped spatial organization even within zones of the olfactory epithelium, with a corresponding spatially-stereotyped glomerular topography in OB.[16,24,58–60] Further, these topographic domains in OB have functional relevance, where region-specific OB manipulations selectively alter different olfactory valence behaviors.[61–63] However, the piriform cortex generally lacks apparent spatial organization or spatial patterning for odor reponses.[22] To

our knowledge, the topographical organization of valence observed here in plCoA represents one of the first descriptions of these spatial patterns occurring in central olfactory areas.

Topographic gradients for valence have been observed in other limbic regions, including the BLA for overall valence, the medial amygdala for innate social behaviors, *Drosophila* dopaminergic mushroom body neurons for general valence, and the gustatory insular cortex for taste valence.[19,34,35,64,65] The gustatory insular cortex is of particular interest, given that it also primarily encodes taste identity and hedonics in a spatially-nonspecific manner.[31,35,66–69] Our results extend this phenomenon of spatially segregated valence into both olfaction and into a less well-described amygdala nucleus, and suggest that it could serve as a potential common motif within the limbic system to organize motivational information, especially for innate behaviors, which require stereotyped neurocircuitry. We believe a model where aplCoA and pplCoA are parts of the same region with similar underlying composition, but with a gradual change in the factor that defines the valence output for a given part of the gradient would best explain the underlying gradient-like effect on positive and negative valence. We considered two such organizational principles underlying this topography: molecular cell types and projection targets. We found that broad divisions of cell types by Slc17a6 and Slc17a7 did not fully define valence, though more specific subtypes could be responsible. Our results demonstrate that the projection targets of plCoA neurons are a fundamental feature for imparting valence on this circuitry.

Molecular Cell Types in plCoA Segregate Topographically and Drive Behaviors of Divergent Valence

While examining the cell types composing plCoA, we noticed numerous notable, novel features. First, despite its small area (~1.04 mm^3 and ~170,000 cells), plCoA displays remarkable diversity, hosting dozens of distinct, robustly separable cell types.[70] The plCoA appears to have multiple domains positioned at the transition between highly dissimilar brain tissue types. Interestingly, the high-dimensional structure of molecular variation differs between glutamatergic and GABAergic neurons. Glutamatergic molecular variation within plCoA is continuous, with two broadly nested groups generally marked by either *Slc17a6* or *Slc17a7* along with one or more additional marker gene(s), though it should be noted that expression of the two broad glutamatergic markers is not necessarily mutually exclusive and a few low abundance “transition” cell types can express both. This leaves open the possibility that a more specific cell type could be necessary for aversion, given that this necessity for this behavior did not perfectly map onto either broad molecular cell type. In contrast, molecular variation in GABAergic neurons is far more discretized, with ensembles expressing one of a few well-characterized interneuron markers found throughout the brain, such as *Sst, Vip,* and *Pvalb*, among others. This is consistent with other studies in neocortex, hippocampus, and subiculum that find similar patterns of variation, where variation within glutamatergic neurons is more continuous than in GABAergic neurons.[42,43,71] In this way, we find the continuous gradient-like structure of valence in plCoA is recapitulated with gradient-like variation in glutamatergic neuron gene expression in plCoA.

In these molecular datasets, we further observed highly specific differences in cell type enrichment within aplCoA and pplCoA within glutamatergic neurons, but not GABAergic neurons or glia. Within plCoA, *Slc17a6*+ neurons are enriched in aplCoA and *Slc17a7*+ neurons are enriched in pplCoA, though there is gradient-like intermingling of populations, especially toward the middle of plCoA, and all glutamatergic neuron types are present, albeit with high variability along the anteroposterior axis. This molecularly defined order suggests a programmed organization, rather than stochastically distributed populations within the region, especially given that its boundaries match the domains previously identified based on behavior and histology.[72] This phenomenon also broadly matches observations in the neocortex, hippocampus, and subiculum, where glutamatergic neurons across subdivisions molecularly diverge to a greater degree than GABAergic neurons or glia, albeit across a correspondingly greater area than within plCoA, which is generally accompanied by distinct morphological and electrophysiological properties broadly corresponding to these transcriptomic differences.[42,43,71,73–76] Spatial segregation of molecular cell types is also observed within deeper brain regions including BLA, thalamus and habenula, and these molecular differences are also accompanied by extended phenotypic differences.[19,77–80] Investigation of such properties held in common and diverging within and between *Slc17a6*+ and *Slc17a7*+ glutamatergic neuron types could also serve to further define the local neurocircuitry and information processing dynamics within plCoA and along its anteroposterior axis.

Interestingly, few if any populations within plCoA are clearly separable from most of the regions surrounding it (e.g. piriform cortex, basomedial amygdala, and MeA) based on primary marker gene identity. Instead, plCoA ensembles seem to be defined by the interplay of all three regions within the same tissue. The predominance of populations resembling different regions does appear related to this anteroposterior organization, though, where *Slc17a6*+ neurons predominate in both aplCoA and MeA, and more specific marker genes like *Meis2* are expressed in both regions as well.[81] Conversely, *Slc17a7*+ neurons predominate in both pplCoA and piriform cortex, and the major marker genes like *Satb2* are similarly expressed in both regions.[82] Such phenomena also cohere with more general characterizations made in whole-brain molecular taxonomies, which divide plCoA along its axis, grouping aplCoA with MeA and pplCoA with paleocortex.[83–85] It would be misleading to characterize plCoA populations as mere extensions of surrounding populations into an adjacent region, though. *Slc17a7*+ neurons from the cortex-amygdala transition zone are also present in the dataset and are continuously separable from *Slc17a7*+ plCoA neurons based on the expression of marker genes like *Fign*. Instead, plCoA may itself be a transition region, given that such a relationship with its neighboring regions is very similar to that of the amygdalostriatal transition area, one of the only transition regions to undergo high-resolution molecular profiling.[86] Given such commonalities between these two putatively dissimilar regions, molecular characterization of additional transition regions could potentially uncover similar organizational motifs, especially if compared with adjacent regions of interest, and allow for a much more in-depth exploration and characterization of the boundaries and transitions between proximally located, distantly related brain regions.

These broad molecular groups of glutamatergic cell types themselves do not completely explain valence in the plCoA. While aplCoA-enriched *Slc17a6*+ neurons are sufficient to drive

aversion and pplCoA-enriched *Slc17a7*+ neurons are sufficient to drive attraction, as would be predicted from the valence responses evoked from each anterior-posterior domain enrichments, it might be expected that these populations would also be necessary for the respective odor-evoked valence. However, only *Slc17a7*+ neurons are necessary for 2PE attraction, whereas the *Slc17a6*+ neurons were not required for aversion to TMT. Given that the plCoA is necessary for TMT aversion, it is unlikely that such a difference is due to additional redundant function within other regions for TMT aversion.[3] Instead, although *Slc17a6*+ neurons likely contribute to the valence behavior, other populations within the region not expressing the marker gene could also contribute to the behavioral response. Thus, although these two broad glutamatergic groups can drive innate responses of valence, the *Slc17a6*+ population doesn't fully represent the population that control aversive responses, which is supported by other findings presented here showing that both *Slc17a6*+ and *Slc17a7*+ neurons project to MeA, while the projection to NAc is almost entirely composed of *Slc17a7*+ neurons. Regarding more specific molecular cell types, it could be possible that only a subset of *Slc17a7*+ neurons are required for 2PE attraction. Similarly, the neurons required for TMT aversion could be marked by a gene orthogonal to the observed *Slc17a6*/*Slc17a7* gradient, and genetic access to olfactory aversion could potentially be established by investigating these more sparsely expressed marker genes. In both cases, though, further investigation into these other cell types would enhance our understanding of both plCoA and innate olfactory valence and allow more precise manipulations in the future.

Downstream Projection Targets of plCoA Divergently Control Innate Olfactory Valence

In this work, we perform the first characterization of plCoA's downstream outputs in the mouse brain. These outputs are dominated by regions generally involved in valence and emotion, such as the NAc, BNST, MeA, BLA, and other amygdalar nuclei, or olfactory areas, such as the pmCoA, OT, and PIR. These outputs are consistent with a role for plCoA in motivational valence for odor. The plCoA also appears to form numerous intra-regional connections, where a significant proportion of synapses formed with other neurons are within the region itself. This raises the possibility that plCoA is not simply a feedforward relay but performs local recurrent processing as well. Recurrent networks in other sensory systems expand the dimensionality of encoding schemata and incorporate additional features to generate mixed, continuously updating representations of relevant information.[87] This raises a number of interesting questions regarding information processing within plCoA. For instance, how does odor representation change based on differences in experience and internal state? Further explorations of information transformation and encoding within plCoA will certainly enrich our understanding of both this region and olfaction in general.

The NAc and MeA are interesting downstream targets given their pre-existing known relationships to attraction and aversion, respectively. NAc has historically been critical to the manifestation and processing of reward and motivated behaviors, though this view has been expanded and made more subtle with a recent focus on action selection in general.[88] On the other hand, MeA has been linked to defensive and stress-related behaviors at baseline and in response to aversive stimuli, as well as chemosensation.[89] MeA has also been specifically linked to olfactory aversion in past studies, as TMT has previously been shown to activate the

MeA, which is necessary for TMT-induced defensive behaviors, though the upstream circuits and processing were not yet investigated.[48,90,91] These circuits are also notable regarding other features of plCoA spatiomolecular organization, as the projections to the downstream regions of interest are the two that diverge to the greatest extent between aplCoA and pplCoA, and between plCoA$^{Slc17a6+}$ and plCoA$^{Slc17a7+}$ glutamatergic neurons. Given the relationship between spatiomolecular patterning and the simple wiring and organizational rules used to structure innate circuits it would be interesting to investigate the plCoA through the lenses of development and genetic variation. These intersect in recent discussions of genetic bottlenecking, where the genome encodes general rules for circuit organization and development that nevertheless yield specific responses to specific stimuli.[92] Such networks have numerous theoretical advantages, such as reduced information requirements and higher performance at criterion, providing a conceptual basis for why spatiomolecularly stereotyped circuits yield innate behaviors, and why these innate behaviors are adaptive in naturalistic settings.[92–94]

Neuronal Activity in plCoA Encodes Odor Identity Via Sparse Population Code

The plCoA receives spatially-ordered inputs and has a cell-type-specific topographical organization with divergent outputs that mediate responses of opposing valence. This anatomical organization is consistent with either labeled-line or divergent paths motifs, though precise connectivity from OB has not yet been described. However, label line coding motif is not apparent in neural activity, but instead there is a sparse population code for odor identity with no apparent valence-specific responses, indicating that the plCoA cannot function as a pure labeled-line relay. Moreover, the absence of valence encoding is distinct from that seen in other divergent path motifs, suggesting the plCoA represents a different circuit model for valence.

We were surprised to find that despite a robust organization of plCoA cell types and projections that support behaviors of valence, the neurons do not appear to encode valence at the single neuron or population level. However, when put in the context of the olfactory system, these results are less surprising. Sparse, distributed population encoding appears to be a general feature of all olfactory regions observed thus far, regardless of their specific structure or computational function within olfaction. In the OE, epithelium-resident OSNs expressing a single receptor will bind multiple odorants and establish odor identity through a combinatorial code.[21,23] In the OB, axon terminals from OSNs expressing the same receptor gather into specific stereotyped glomeruli, where mitral/tufted cells (M/T) then transmit this information to third-order olfactory regions, where both steps represent the odor identity via a sparse population code in a spatially-distributed manner.[24,26,32,95] The primary olfactory cortex further represents odor identity and chemical space similarly through sparse, spatially distributed combinatorial population activity in a similar manner to its M/T inputs.[17,22,32,96] The OT, a striatal region primarily composed of *Drd1*- or *Drd2*-expressing medium spiny neurons, also broadly represents odor identity across both cell types, despite their opposing roles elsewhere in striatum, though a secondary contribution by hedonic value is currently debated.[25,97–101] Although direct comparisons of olfactory regions find some differences in features like sparsity, clustering, or correlation structure, these are generally reported as differences in degree, not in kind.[17,30,32,95,99,100] Given the remarkable similarity in encoding between these structurally and functionally distinct regions, it logically follows that an olfactory region with amygdalar structure

would follow similar population encoding principles. Indeed, were plCoA to predominantly encode stimulus valence in a manner akin to other amygdalar regions, it would reflect a greater divergence from olfactory coding principles than what we observe. Instead, the olfactory encoding scheme employed by plCoA reveals a novel framework for valence encoding that is distinct from that in the extended amygdala.

How does innate valence arise from a population code imposed on stereotyped valence circuitry? One possibility is that the valence of an odor is defined by the proportion of NAc and MeA-projecting neurons activated, mixing features of divergent paths and opposing components motifs. In this model a given odor will activate some balance of NAc and MeA projecting neurons and the proportional balance determines the valence. If true, one should be able to predict the valence of the odor by recording from a large sample of these neurons, which is beyond the scope of this study. Another possibility is that activity could evolve over the time course of behavior such that a mixture of inputs from local circuitry and long-range circuits could function like attractor networks to shape output into one of a few convergent states. A third possibility is that valence may emerge in combination with behavior and internal state. In this model, the plCoA integrates sensory information with other state variables to shift the activity towards one output. If either of these latter two models is correct, recording activity over longer time scales in freely moving animals could provide insight into how activity correlates with behavior. Alternatively, valence may arise downstream of plCoA, but molecular mechanisms to support this model are currently undescribed, and such a model would be at odds with our finding of divergent valence-specific circuitry required for innate valence responses. Innate behavior is indeed dynamic and more complex than attraction and avoidance. These different models for valence encoding could serve to increase the flexibility of the system to adapt to changes in experience or internal state.

A Novel Circuit Motif for Valence

The widespread circuit model for valence encoding centers on divergence, in which information is routed to different pathways depending on the valence of the stimulus. The plCoA circuit we have identified is anatomically similar, but unique in its encoding properties. Most divergent circuits function to generalize stimuli, discarding information about stimulus identity to simplify to low dimensional valence signals from distinct neuronal populations. In contrast, the plCoA groups stimuli, using a high dimensional code of odor identity that is routed through divergent projections to mediate opposing valence responses. In this model, the valence of an odor could be determined based on the population dynamics and composition within a distributed, sparse population code that ultimately funnels information through divergent pathways corresponding to their innate valence. Such a model could serve to increase the flexibility of the system while retaining the ability to yield stereotyped responses.

ACKNOWLEDGMENTS

We thank the entire Root lab for helpful discussion and support. We thank B. Lim for provision of the AAVDJ-hSyn-Flex-mRuby-T2A-SynEGFP virus. We thank G. Pekkurnaz, N. Spitzer, and M. Pratelli for reagents and facilities support. We also thank C. O'Connor and L. Boggeman at the Salk flow cytometry core, and N. Hah at the Salk next-generation sequencing core. We thank D. Jimenez for assistance with histology and colony management. This publication includes data generated at the UC San Diego IGM Genomics Center utilizing an Illumina NovaSeq 6000 that was purchased with funding from a National Institutes of Health SIG grant (#S10 OD026929). This work was generously supported by the National Defense Science and Engineering Fellowship (J.R.H.), CIHR Postdoctoral Fellowship (F.M.), JPB Foundation, the PIIF, PNDRF, JFDP, New York Stem Cell Foundation, Klingenstein Foundation, McKnight Foundation, Salk Institute, Howard Hughes Medical Institute, Clayton Foundation, Kavli Foundation, Dolby Family Fund (K.M.T.), the Hellman Fellowship (C.M.R.), and the National Institutions of Health, via grants through the NIA (RF1AG061831-01S1, P.A.D.), NIMH (K99MH121563-02, F.M.; R01MH115920-03 and R37MH102441, K.M.T.), NIDDK (DP2DK102256-01S1, K.M.T.), and NCCIH (DP1AT009925-04, K.M.T.), and the NIDCD (R00DC014516-05 and R01DC018313-01A1, C.M.R.).

AUTHOR CONTRIBUTIONS

J.R.H. and C.M.R. conceived the project. J.R.H., C.L.C., D.L., M.B., and A.N.Z. performed surgeries and analyzed histological data. J.R.H., C.L.C., and A.N.Z. performed behavioral experiments, managed the colony, and analyzed behavioral data. J.R.H. and D.L. performed calcium imaging experiments and analyzed calcium imaging data. J.R.H. performed sequencing experiments, analyzed sequencing data, and prepared all figures. H.K.R. and P.A.D. designed and performed spatial transcriptomics experiments and provided data for analysis. F.M., M.E.L., and K.M.T. provided the CellProfiler processing pipeline, as well as intellectual, facilities, and logistic support and guidance. C.M.R. supervised the project. J.R.H., D.L., M.B., H.K.R., and C.M.R. wrote the manuscript. All authors edited the manuscript.

DECLARATION OF INTERESTS

The authors declare no competing interests.

RESOURCE AVAILABILITY

Lead contact

Further information and requests for resources and reagents should be directed to and will be fulfilled by the Lead Contact, Cory M. Root (cmroot@ucsd.edu).

Materials availability

This study did not generate new unique reagents.

Data and code availability

All snRNA-seq and Visium spatial sequencing data generated for this study is deposited on Gene Expression Omnibus (GEO): GSE270798. All other data reported in this paper will be shared by the lead contact upon request. The code used to analyze all data and generate all graphs can be found online at Zenodo: . Any additional information required to reanalyze the data reported in this paper is available from the lead contact upon request.

EXPERIMENTAL MODEL AND SUBJECT DETAILS

All procedures at the University of California, San Diego, and Columbia University were performed in accordance with Institutional Animal Care and Use Committee protocols in accordance with NIH guidelines. All mice were provided food and water ad libitum and maintained on a regular 12-hour reverse light/dark cycle at room temperature, with weight, health, and immune status monitored daily and verified to be within normal ranges. Mouse cages were changed regularly based on degree of soiling. All mice were group-housed with randomly assigned littermates prior to surgery, and single-housed after surgery. All animals were used in a single experiment each, except for a subset of mice who underwent 4-quad, EPM, and OFT experiments, who performed each test in no specific order.

Subject Details for Sequencing Experiments

Subject details for single-nucleus sequencing

All mice for snRNA-seq in the study were males on the wild-type C57BL/6J background (RRID:IMSR_JAX:000664) and received directly from Jackson Laboratories at 6 weeks of age and acclimated to the colony prior to experiments. Animals were single-housed and placed into sensory deprivation 24 hours prior to sacrifice to reduce artifactual immediate early gene expression. Sacrifice was performed at P60 ± 3 days (n = 5-10 mice per pool). Sample size was determined based on number of expected nuclei per region per mouse: estimates of expected nuclei were determined empirically, though nuclear recovery was approximately 20% of total based on cellular density estimates from the Blue Brain Cell Atlas.[70] 20,000 nuclei were targeted per combination of assay, condition, and region, which was determined using SCOPIT v1.1.4, allowing potential detection of at least 10 nuclei from 10 rare subpopulations at 0.1% frequency with 95% probability.[103] A total of 50 mice were used for this purpose.

Subject details for spatial transcriptomics

In the separate study for spatial transcriptomics, APP23 (B6.Cg-Tg(Thy1-APP)3Somm/J; C57BL/6J background, RRID:IMSR_JAX:030504) non-transgenic (NTG) littermates control mice were housed in light-tight enclosures.[104] The mice were given ad libitum food and water access. This study used a total of 17 mice almost equally distributed across sex, of which sections from 11 sagitally bisected the plCoA and were used in downstream analysis. No analysis of sex differences was performed due to inaccessibility of that information on a per-section basis.

However, no such differences were apparent from per-section gene expression correlations reported in supplementary information.

Subject Details for Calcium Imaging, Tracing, and Activity Manipulations

Subject details for wild-type experiments

All mice for topographic and projection-defined manipulation and tracing experiments, as well as calcium imaging, were males on the wild-type C57BL/6J background and received directly from Jackson laboratories before 12 weeks of age. After surgery, mice incubated for at least 21 days if injected with virus or at least 7 days if injected with a retrograde tracer (e.g. retrobeads, cholera toxin B) to allow virus to express and tracers to travel in retrograde, respectively. All surgeries and downstream experiments were performed on mice at least 8 weeks of age.

Subject details for transgenic experiments

We used VGlut2-IRES-Cre (Slc17a6tm2(cre)Lowl; C57BL/6J background, RRID:IMSR_JAX:028863; *Slc17a6::Cre*) and VGlut1-IRES2-Cre-D (Slc17a7tm1.1(cre)Hze; C57BL/6J background, RRID:IMSR_JAX:023527; *Slc17a7::Cre*) strain mice for molecularly defined optogenetic stimulation experiments and genotype-specific tracing.[44,45] These mice were bred on-site at UCSD and were genotyped in-house using genomic DNA from ear tissue amplified with the default primer sets listed by Jackson Laboratories. All mice used for experiments had a heterozygous genotype for the transgenic construct of interest. After surgery, mice incubated for at least 21 days to allow viral expression.

METHODS DETAILS

Stereotactic surgery procedures

All surgeries were performed under aseptic conditions using a model 1900 digital small animal stereotaxic instrument (Kopf Instruments). Mice were initially anesthetized in a sealed box containing 5% gaseous isoflurane, and then deeply anesthetized using isoflurane (2.5% in 1L/min of O_2) during surgeries (VetFlo, Kent Scientific Corporation). We immobilized and leveled the head in a stereotaxic apparatus (Kopf Instruments), removed fur from the scalp by shaving, applied eye lubricant (Optixcare), cleaned the incision site with 70% ethanol and betadine prior to incision, peeled off connective tissue, and dried the surface of the skull prior to craniotomy before proceeding with injections and implantations specific to certain experiments. All virus injections were performed at 2 nL/sec using a pulled glass pipette (Drummond) and a Nanoject III pressure injector (Drummond). To prevent backflow, the pipette was left in the brain for 15 minutes after injection.

Surgeries for calcium imaging

Surgeries for imaging experiments were performed in a manner similar to that previously described.[33] The skull was prepared with OptiBond™ XTR primer and adhesive (KaVo Kerr)

prior to the craniotomy. After performing a craniotomy 1 mm in diameter centered around the virus injection site, a 27G blunt needle was used to aspirate ~2.5 mm below the brain surface. 600 ul of AAV9-hSyn-FLEX-jGCaMP8s-WPRE (2.5×10^{13} gc/ml, Addgene) was diluted to ~1×10^{12} gc/ml gc/ml and injected into the left middle plCoA in two 300 ul boli, one in layer 2 and one 400 um dorsal (+0.4 DV) in layer 3. Following the viral injection, a head-plate (Model 4, Neurotar) was secured to the mouse's skull using light-curing glue (Tetric Evoflow, Ivoclar Group). At least 30 minutes after viral injection, a 1 mm GRIN lens (NA, ~1.9 pitch, GrinTech) was sterilized with Peridox-RTU then slowly lowered at a rate of 500 um/min into the craniotomy until it was 200 um dorsal (+0.2 DV) to the injection coordinate. The lens was adhered to the surface of the skull using Tetric Evoflow. We then placed a hollow threaded post (AE825ES, Thorlabs) to act as a housing for the lens and adhered it using Tetric Evoflow. Any part of the skull that was still visible was covered using dental cement (Lang Dental). Finally, the housing was covered with a Nylon cap nut (94922A325, McMaster-Carr) screwed onto the thread post to protect the lens in between imaging. Animals were left on the heating pad until they fully recovered from anesthesia.

Surgeries for optogenetic stimulation

For optogenetic topographic- or projection-specific stimulation experiments, we injected wild-type C57BL/6J mice between 2-4 months of age with 100 (if topographic) or 150 (if projection-specific) nL of either AAV5-hSyn-eYFP (3.3×10^{12} gc/ml, UNC Vector Core) or AAV5-hSyn-ChR2-mCherry-WPRE-PA (4.1×10^{12} gc/ml, UNC Vector Core). For Cre-dependent molecularly defined optogenetic stimulation, we injected 200 nl AAV5-EF1A-DIO-hChR2(H134R)-eYFP (5.5×10^{12} gc/ml, UNC Vector Core) or AAV5-EF1A-DIO-eYFP (4.0×10^{12} gc/ml, UNC Vector Core) All such injections were left unilateral, into either aplCoA or pplCoA for topographic photostimulation, and into middle plCoA for projection- or genotype-specific photostimulation. For topographic and genotype-specific photostimulation animals, we implanted the fiber 300 um (+0.3 DV) directly above the injection site with all other coordinates remaining constant. Anterior-posterior axis positioning arose from stochastic variation in virus and fiber placement. For projection-specific photostimulation animals, we implanted the fiber 300 um (+0.3 DV) directly above either the MeA or NAc, holding all other coordinates for the two regions constant as described above. For all optogenetic stimulation experiments, we implanted a fiber optic cannula (2.5 mm ferrule outer diameter, 200 um core, 0.39 numerical aperture; RWD) 300 um above the targeted stimulation site. These fibers were affixed onto the skull using OptiBond XTR (Kerr) and stably secured with Tetric Evoflow (Ivoclar Vivadent) coated with cyanoacrylate (Toagosei). After surgery, we injected all mice with 0.04 mL Buprenorphine SR (Ethiqa XR, Fidelis) for pain management. All mice were given their own cage immediately after surgery and returned to the colony once ambulatory.

Surgeries for chemogenetic inhibition

For all plCoA inhibition experiments, we bilaterally injected C57BL/6J mice between 2-4 months of age with 250 nL of either AAV2-hSyn-DIO-hM4D(Gi)-mCherry (7.1×10^{12} gc/ml, Addgene) or AAV2-hSyn-mCherry (1.8×10^{13} gc/ml, Addgene) virus. For projection-specific inhibition experiments, wild-type C57BL6/J mice were used, and AAVretro-hSyn-EBFP-Cre (1.5×10^{12}

gc/ml, Addgene) either 50 µL were injected into MeA or 300 µL were injected into NAc. For genotype specific inhibition experiments, *Slc17a6::Cre* or *Slc17a7::Cre* mice were used. All injections were bilateral and targeted to middle plCoA.

Surgeries for fluorescent tracing

For non-topographic anterograde tracing experiments, we bilaterally co-injected of mixed 50 nl AAVDJ-hSyn-FLEX-mRuby-T2A-SynEGFP (4.0×10^{12} gc/ml, Addgene, a gift from Byungkook Lim) and AAV5-EF1A-mCherry-IRES-Cre-WPRE (1.9×10^{12} gc/ml, UNC Vector Core) into middle plCoA (-1.8 AP, +/-2.9 ML, -5.95 DV).[105,106] For topographic anterograde tracing experiments, we unilaterally injected 20 nl AAV8-hSyn-hChR2(H134R)-mCherry (2.1×10^{13} gc/ml, Salk GT3 Viral Vector Core) and AAV8-hSyn-hChR2(H134R)-eYFP (3.2×10^{13} gc/ml, Salk GT3 Viral Vector Core) into aplCoA (-1.4 AP, -2.8 ML, -5.95 DV) and pplCoA (-2.1 AP, -3.0 ML, -5.95 DV), counterbalancing region by fluorophore. For retrograde topographic tracing experiments, we unilaterally injected Red Retrobeads IX (Lumafluor) into either MeA (50 nl, -1.2 AP, -2.0 ML, -5.5 DV) or NAc (+1.1 AP, -1.35 ML, -4.5 DV), at volumes of 50 nl or 300 nl, respectively. For anterograde collateralization experiments, AAVretro-EF1A-IRES-Cre (1.3×10^{13} gc/ml, Addgene) into either MeA or NAc, and AAVDJ-EF1A-DIO-hChR2(H134R)-eYFP-WPRE-pA (4.03×10^{13} gc/ml, Salk GT3 Viral Vector Core) was injected into middle plCoA. For genotype-specific anterograde tracing experiments we injected 50 µl AAVDJ-Ef1a-DIO-ChR2(H134R)-eYFP-WPRE-pA into middle plCoA in Slc17a6::Cre or Slc17a7::Cre mice.

Calcium Imaging

Odor exposure

Odor exposure for imaging experiments was adapted from methods previously described elsewhere.[25] Odor was delivered to the mouse using a custom-built olfactometer. Compressed medical air was split into 2 gas-mass flow controllers (Aalborg). One flow controller directed a constant rate of 1.5 L/min to a hollowed out teflon cylinder. The other flow regulator was connected to a 3-way solenoid valve (The Lee Co.). Prior to odor delivery, the 3-way valve directs clean air at 0.5 L/min to the teflon cylinder. During odor delivery, the 3-way valve directs air to an odor manifold, which consists of an array of 2-way solenoid valves (The Lee Co.), each connected to a different odor bottle. The kinetics and consistency of odor delivery were characterized using a miniature Photoionization Detector (mPID) (Aurora Scientific). Depending on the trial type, the appropriate 2-way valve opens, directing 0.5 L/min of air flow through the odor bottle containing a kimwipe blotted with 20 ul of odorant, except for 2PE and peanut oil, which were undetectable to human perception and the mPID after repeated presentation, and were provided in excess to ensure consistent detectability after numerous exposures.

Prior to imaging, mice were habituated to the head fixation device (Neurotar) and treadmill for at least 3 days for at least 5 minutes per session beginning at least 10 weeks after surgery. The treadmill parts were 3D printed using an LCD printer (EPAX) from publicly available designs.[116] Walking behaviors were measured using a quadrature encoder (Broadcom). A video feed of the animal's face was also recorded using a camera (Basler) with an 8-50mm zoom lens (Arducam)

at 20 Hz with infrared illumination (Lorex Technology). Animals were exposed to the following odors for 2 seconds: the appetitive odors 2-phenylethanol (Sigma-Aldrich) and peanut oil (Spectrum), the neutral odors 1-heptanol (Sigma-Aldrich) and isoamyl acetate (Sigma-Aldrich), and the aversive odors trimethylthiazoline (BioSRQ) and 4-methylthiazole (Sigma-Aldrich). Within a single contiguous exposure session, each of the 6 odors were provided 20 times with 12-18 seconds of inter-trial interval. Trials were organized into 6 blocks, each of which consisted of 20 trials of each of the 6 odors in counterbalanced order without any odors of similar innate valence adjacent to each other in the trial structure.

2-photon microscope data acquisition

Ca^{2+} imaging data was acquired using an Olympus FV-MPE-RS Multiphoton microscope with Spectra Physics MaiTai HPDS laser, tuned to 920 nm with 100 fs pulse width at 80 MHz. Each 128 × 128 pixel scan was acquired with a 20x air objective (LCPLN20XIR, Olympus), using a Galvo-Galvo scanner at 5 Hz. Stimulus delivery and behavioral measurements were controlled through a custom software written in LabVIEW (National Instruments) and operated through a DAQ (National Instruments). Each imaging session lasted up to 90 minutes and was synchronized with the stimulus delivery software through a TTL pulse. Animals were excluded from analysis if histology showed that either the GRIN lens or the jGCaMP8s virus was mistargeted or the motion during imaging was too severe for successful motion correction.

Behavioral Assays

Mice had been handled for 5 days prior to experiments and acclimated to the room for an hour prior to testing. All behavioral experiments were performed during the dark period of the light/dark cycle at least an hour away from the switch between the two photoperiods. Not all mice were run in all assays, as elevated plus maze and open field tests were added after a significant proportion of four-quadrant data was collected at targeted sample sizes and mice had already been sacrificed.

For all optogenetic experiments, optical fibers (200 mm, 0.39 numerical aperture, Thorlabs) were epoxied to 2.5 mm stainless steel ferrules (Precision Fibre Products), and polished with a fiber optic polishing kit (Thorlabs) to achieve a minimum of 80% transmission. After surgical implantation, the ferrules protruding from the mouse's head were coupled to an ADR-800A 100 mW 473 nm laser (LaserCentury) via custom-made patch cables with a single rotary joint (Doric Lenses) between the mouse and laser. Laser intensity was set to 5-8 mW at the end of the patch cable. For inhibition experiments, all mice were injected intraperitoneally 60 minutes prior to the beginning of the behavioral trial with either sterile PBS vehicle or with clozapine-N-oxide (CNO) dihydrochloride (Hello Bio) dissolved in sterile PBS for a dosage of 2 mg/kg.

Four quadrant open field assay

The four-quadrant open-field task was performed as previously described.[3] In short, all behavioral assays took place in a four-quadrant open field chamber. Airflow was pumped into each quadrant via gas-mass flow controllers 150 mL/min (Cole-Parmer). Airflow exited the

chamber via a 1-inch outlet in the center of the chamber's floor covered by steel mesh, and the outlet was connected a vacuum line with a gas-mass controller set to 750 ml/min. The chamber was housed in the dark and illuminated from below by infrared lighting. A Basler A601FM camera (Edmund Optics) mounted above the chamber recorded videos of behavioral trials at 4 Hz, and custom software written in Labview (National Instruments) tracked the position of the mouse in real time for each frame. The symmetrical four-quadrant open field chamber was contained in a lightproof structure (0-10 lux) and illuminated by infrared lights, removing any potential spatial cues available to the animals with respect to the room or its surroundings. In optogenetic experiments, an additional 5 cm spacer was added to the chamber flush with the walls to raise their height for more naturalistic behavior, and an acrylic ceiling with a top with a circular opening 30.5 cm in diameter was added to prevent escape while allowing the fiber optic cable to move freely.

In optogenetic experiments, the laser was pulsed with 50 ms bins at 10 Hz, and there was a steep gradient from 1 to 10 Hz along the perimeter of the quadrant, increasing as proximity to the corner of the quadrant decreased. Preliminary experiments in topographical stimulation animals identified no clear behavioral effects from the location of the stimulus quadrant itself (data not shown), and all other downstream stimulation experiments exclusively used the lower right quadrant for stimulation to simplify data analysis. The lasers were controlled by TTL modulation from custom Labview software synchronized to the video capture system.

For inhibition experiments, odor was applied by solenoid valves redirecting airflow through 100 mL glass bottles containing 1 µL of a pure odorant on a small piece of Kimwipes. Odorants used were either the previously-validated innately aversive 2,5-dihydro-2,4,5-trimethylthiazoline (BioSRQ) or the innately appetitive 2-phenylethanol (Sigma-Aldrich) on a small piece of Kimwipe.[3] All odors were presented in the lower-right quadrant, and all trials were spaced out with at least an hour between runs, during which vacuum was applied to the chamber. Odors and injection treatments were given in counterbalanced, independent order within experimental groups.

Open field test

The open field is a square arena illuminated to 100-150 lux by ambient lighting. Mice were habituated to the room for at least an hour prior to testing, but otherwise had no prior experience in the arena prior to exposure. Mice were placed in the center of a square arena (27.3 × 27.3 × 20.3 cm, Med Associates) with four transparent plexiglass walls. Overall locomotion, immobility, and time spent in corners and center regions of arena during each epoch was analyzed for each mouse. Immobility was defined as movement under 0.5 cm/s for a period of at least 1 s, while the center was defined as the middle 13.7 × 13.7 cm square in the center of the arena and the corners as the corner regions that do not overlap with the center square in either direction (25% of arena area for each region). For optogenetic experiments, mice were allowed to move freely throughout the arena for 25 min total, with 5-8 mW 473 nm light stimulation pulsed with 50 ms bins at 20 Hz, alternately delivered during the 5-10 min and 15-20 min epochs (OFF, ON, OFF, ON, OFF). For chemogenetic experiments, mice were allowed to freely move through the area for 10 min total.

Elevated plus maze

The arms of the elevated plus maze were 30.5 × 5.5 cm. The height of the closed arm walls was 15 cm. The maze was elevated 40 cm from the floor and was placed in the center of the behavior room away from other stimuli. Arms were illuminated to 0-10 lux, with infrared illumination. Mice were placed in the center of maze at the beginning of each trial. For optogenetic experiments, mice were allowed to move freely throughout the maze for 15 min total, with 5-8 mW 473 nm light stimulation pulsed with 50 ms bins at 20 Hz delivered during the 5-10 min epoch (OFF, ON, OFF). For chemogenetic experiments, mice were allowed to freely move through the area for 10 min total.

Histology

Non-RNAscope section preparation

All sacrifices were performed during the dark period of the light cycle. Animals were anesthetized prior to sacrifice via combined intraperitoneal injection of 150 mg/kg ketamine (Zetamine, Vet One) and 15 mg/kg xylazine (AnaSed, AMRI Rensselaer). Except for animals used in sequencing studies, animals were subject to transcardial perfusion with 10 mL of sterile phosphate-buffered saline (PBS), followed by 10 mL 4% paraformaldehyde (PFA) solution. The brain was then extracted from the animal and placed into a 4% (PFA) solution in PBS for at least 36 hours until it was sectioned on a VT1000S vibratome (Leica). For tissue extracted for non-RNAscope histology, mice were transcardially perfused with 20 ml phosphate buffered saline (PBS) followed by 20 ml 4% paraformaldehyde (PFA) in PBS. All brains were extracted and post-fixed for at least 24 hours in 4% PFA. For tissue extracted for RNAscope, mice under 6 months of age were decapitated once unconscious and their brains were extracted into a square Peel-A-Way embedding mold (Polysciences) and embedded in OCT (Fisher), and then snap-frozen a dry-ice/isopentane slurry and stored at -80˚C until cryosectioning within a month of sacrifice.

Tissue was mounted in 5% agarose and sectioned sagittally on a vibratome for retrograde experiments, or sectioned coronally without mounting for all other non-RNAscope experiments. These sections were cut at 50 µm and stored in PBS before processing. All connectomic quantitation was performed on samples using epifluorescence without immunolabeling to avoid potential bias due to non-stoichiometric antibody binding, while all others were immunolabeled for visualization of viral targeting accuracy and collection of representative images. Immunolabeling of eYFP and other GFP-derived fluorophores was performed using goat anti-GFP primary antibodies (Abcam) and Alexa Fluor 488-conjugated anti-goat secondary antibodies (Invitrogen), while immunolabeling of mCherry and other DsRed-derived fluorophores used rabbit anti-DsRed primary antibodies (Takara) and Alexa Fluor 588-conjugated anti-rabbit antibodies (Invitrogen), all diluted 1:1000 in PBS-T. All non-RNAscope sections were mounted on Superfrost Plus microscope slides (Fisher) and counterstained with Fluoromount-G containing DAPI (SouthernBiotech). Sections were stored long-term at 4˚C.

RNAscope fluorescence in situ *hybridization*

RNAscope sections were cut at 15 µm on a CM 1950 cryostat (Leica) and mounted on Superfrost Plus slides and stored at -80˚C until processing via RNAscope within a month of mounting. RNAscope was performed in an RNA-free environment according to manufacturer instructions using the Multiplex Fluorescent Reagent Kit v2 (Advanced Cell Diagnostics).[107] RNAscope was performed using the probes *mm-Slc17a7* in the C2 channel, and *mm-Slc17a6* in the C3 channel, dyed with Opal 520 and Opal 690 in a counterbalanced manner at 1:15,000 concentration to reduce background fluorescence and allow quantitation of unsaturated, clearly-distinguishable puncta.[108] Processed RNAscope sections were then mounted with Prolong Antifade Diamond (ThermoFisher) and stored long-term at 4˚C.

Fluorescence image acquisition

Non-RNAscope Images were acquired at 10X magnification with an VS120 slide scanner (Olympus), with settings held constant within experiments. Confocal fluorescence images for RNAscope were acquired on an SP8 (Leica) confocal laser scanning microscope using a 40x/1.30NA oil immersion objective. Serial Z-stack images were acquired using the LASX software at a thickness of 1 µm per Z stack, with 14-21 planes taken per image. Images were acquired with identical settings for laser power, detector gain, and amplifier offset for each set of counterbalanced probe-fluorophore combinations.

Sequencing Data Acquisition

Tissue extraction and cryopreservation for single-cell sequencing

Once unconscious, mice animals were transcardially perfused with ice-cold, carbogen-bubbled (95% O2, 5% CO2), nuclease-free, 0.22 µm sterile-filtered artificial cerebrospinal fluid (ACSF) with a composition of 93 mM N-methyl-D-glucamine, 2.5 mM KCl, 1.2 mM NaH2PO4, 30 mM NaHCO3, 20 mM HEPES, 25 mM glucose, 5 mM sodium ascorbate, 2 mM thiourea, 3 mM sodium pyruvate, 13.2 mM trehalose, 12 mM N-acetyl-cysteine, 0.5 mM CaCl2, 10 mM MgSO4, and 93 mM HCl, at pH 7.3-7.4.[42,109] Following transcardial perfusion, brains were immediately extracted and submerged into ice-cold carbogen-bubbled ACSF, with less than 5 minutes between the beginning of perfusion and final submersion after extraction. Brains were serially sectioned in ice-cold, carbogen-bubbled ACSF on a VT1000S vibratome (Leica) with polytetrafluoroethane-coated razor blades (Ted Pella) at 0.15 mm/sec and 100 Hz, dividing the whole cerebrum into 400 µm coronal slices. Target regions were microdissected from these slices under a stereomicroscope using a sterile blunt-end needle (22 gauge for CeA, ASt, and tail of striatum, 16 gauge for dorsal striatum). All regions were targeted using Paxinos & Franklin, 5th Edition, as reference.[36] Extracted tissue samples were recovered in ice-cold, nuclease-free, 0.22 µm sterile-filtered cryoprotective nuclear storage buffer, composed of 0.32 M sucrose, 5 mM CaCl2, 3 mM magnesium acetate, 10 mM Trizma hydrochloride buffer (pH 8.0), 1 mM dithiothreitol, 0.02 U/µl SUPERase•In RNAse Inhibitor (Invitrogen), and 1X cOmplete Protease Inhibitor Cocktail with EDTA (Roche). Tissue was then snap frozen using a metal CoolRack M90 (Biocision) pre-chilled to -80˚C and stored at -80˚C until nuclear isolation. Following extraction of tissue regions of interest, remaining portions of sections were fixed in 4% paraformaldehyde and 4′,6-diamidino-2-phenylindole (DAPI) was applied to sections at 1 µg/ml.

After fixation and staining, sections were mounted and imaged on an VS120 slide scanner (Olympus). From these images, dissection accuracy was assessed for each region, and individual samples were only selected for downstream nuclear isolation if the extracted tissue fell entirely within the defined target regions.

Nuclear isolation procedures were adapted from multiple methods described previously.[102,110] All procedures were performed on ice, and all solutions were ice-cold, nuclease-free, and 0.22 µm sterile-filtered. Cryopreserved tissue pieces were slow thawed by incubation at 4˚C for 1 hour prior to isolation. Tissue pieces were then pooled and resuspended in nuclear isolation medium composed of 0.25 M sucrose, 25 mM KCl, 5 mM MgCl2, 10 mM Trizma hydrochloride buffer (pH 7.4), 1 mM dithiothreitol, 0.04 U/µl RNasin Plus RNAse Inhibitor (Promega), 1X cOmplete Protease Inhibitor Cocktail with EDTA (Roche), and 0.1% Triton-X. The pooled tissue pieces in nuclear isolation medium were transferred to a 2 mL Dounce tissue grinder. Tissue was homogenized by 5 strokes from the loose pestle and 15 followed by the tight pestle, and the resulting homogenate was filtered through a 40 µm Flowmi cell strainer (Bel-Art) into a 1.5 ml Lo-Bind tube (Eppendorf). The homogenate was then centrifuged with a swinging bucket rotor at 4˚C and 1000 x g for 8 minutes. Nuclei were then washed with nuclear flow buffer composed of DPBS with 1% bovine serum albumin, 1 mM dithiothreitol, and 0.04 U/µl RNasin Plus RNAse Inhibitor (Promega) and centrifuged at 4˚C and 500 x g for 5 minutes, which was subsequently repeated. Nuclei were finally resuspended in nuclear flow buffer containing 3 µm DRAQ7 (Cell Signaling Technology) and again filtered through a 40 µm Flowmi cell strainer into a 5 ml round-bottom polystyrene tube. Each isolation took under 45 minutes to perform, from homogenization to final suspension.

Fluorescence-activated nuclei sorting (FANS)

FANS was carried out on a FACSAria II SORP (BD Biosciences) using a 70 µm nozzle at 52 PSI sheath pressure. For FANS, debris was first excluded by gating on forward and side scatter pulse area parameters (FSC-A and SSC-A), followed by exclusion of aggregates (FSC-W and SSC-W), and finally gating for nuclei based on DRAQ7 fluorescence (APC-Cy7). Nuclei were successively sorted into 1.5 ml LoBind tubes (Eppendorf) under the purity sort mode. The tube contained 10X RT master mix without RT Buffer C. 16,000 total nuclei were targeted for downstream processing, and to account for cytometer errors and subsequent loss of nuclei, 21,000 were sorted into the tube. Nuclei were then immediately processed for snRNA-seq. FANS conditions were optimized for isolation of debris-free nuclei using the LIVE/DEAD Viability/Cytotoxicity Kit for Mammalian Cells (Molecular Probes), adding to the final suspension according to manufacturer instructions and examining on a hemocytometer using an EVOS FL Cell Imaging System (Thermo Fisher) for enrichment of ethidium homodimer-1-positive nuclei and the absence of Calcein AM-labeled cellular debris.

Tissue extraction and sample preparation for spatial transcriptomics

Mice were euthanized with CO_2 followed by decapitation, either in the dark or in the light. Brain hemispheres were collected and placed in OCT and then flash frozen in isopentane in liquid nitrogen. One hemibrain from each mouse was cryosectioned at -18°C sagittally to a thickness

of 10 mm (~2.8 mm from the midline) using a standard Leica CM1860 cryostat and processed according to the recommended protocols (Tissue optimization: CG000240 Visium 10X Genomics; Gene expression: CG000239). The tissue was immediately mounted on a Visium spatially barcoded slide (10X Genomics). The tissue was covered with OCT and kept at -80 degrees C until it was cryosectioned again starting at the same position to a thickness of 10mm and mounted onto a Superfrost plus microscope slide (Fisherbrand) for staining. Each section covered approximately 80% of the 5,000 total spots within their fiducial frame. Slides were stored at -80˚C until use.

Library Preparation

Library preparation for single nucleus sequencing

Nuclear suspensions were converted into barcoded snRNA-seq libraries using the Chromium Next GEM Single Cell 3' v3.1 Reagent Kits v3.1 Single Index (10X Genomics). Library preparation for both assays was performed in accordance with the manufacturer's instructions. 10,000 nuclei were targeted during each snRNA-seq library preparation run. 10X libraries were first sequenced at low depth on a NextSeq 550 Sequencing System (Illumina) to estimate quality and number of nuclei for each library, followed by deep sequencing on a NovaSeq 6000 Sequencing System. All runs were performed using 2 x 100-bp paired-end reads, outputting data in 28/8/91-bp read format for snRNA-seq runs.

Library preparation for Visium spatial transcriptomics

Visium spatial gene expression slides and reagents were used according to the manufacturer instructions (10X Genomics). Each capture area was 6.5mm x 6.5 mm and contained 5,000 barcoded spots that were 55 µm in diameter (100 µm center to center between spots) provide an average resolution of about 1 to 10 cells per spot. Optimal permeabilization time was measured at 24 min. Libraries were prepared according to the Visium protocol (10X Genomics) and sequenced on a NovaSeq4 (Illumina) at a sequencing depth of 182 million read pairs. Sequencing was performed with the recommended protocol in a 28/10/10/100-bp read format. H&E (Hematoxylin, Thermo; Dako bluing buffer, Dako; Eosin Y, Sigma) staining and image preparation was performed according to the Visium protocol. H&E-stained sections were imaged using a Nanozoomer slide scanner (Hamamatsu) Spatial gene expression assay was performed according to the protocol CG000239.

QUANTIFICATION AND STATISTICAL ANALYSIS

Statistical Analysis

All statistical details can be found in the figure legends. Sample sizes for behavioral studies were chosen based on past optogenetic studies for each behavior, which had used 6-15 animals per group. Blinding experimenters was not possible for behavioral, imaging, or sequencing experiments, given familiarity with subjects, but manual quantitation for connectivity experiments was performed blinded to group with random assignment. All statistical tests were performed in R (v4.2.3) unless otherwise specified. All statistical tests were performed with two

tails. Group comparisons were made using two-way analysis of variance (ANOVA) followed by Bonferroni post hoc tests, except where otherwise specified. All behavioral experiments were performed by multiple experimenters across multiple cohorts each composed of multiple litters, with littermates distributed across control and treatment groups, with all such cohorts yielding similar results (data not shown), and topography stimulation experiments were performed across multiple facilities and institutions. Numbers of mice used for all non-sequencing experiments are reported within the relevant figures, figure legends, and the text.

Calcium Imaging Data Analysis

Image processing

Data analysis for calcium imaging experiments was adapted from methods previously described elsewhere.[25] Ca^{2+} imaging data were first motion-corrected using the non-rigid motion correction algorithm NoRMCorre.[111] Afterwards, neural traces were extracted from the motion-corrected data using constrained nonnegative matrix factorization (CNMF).[112,113] Spatial components identified by CNMF were inspected by eye to ensure they were not artifacts. A Gaussian Mixture Model (GMM) was used to estimate the baseline fluorescence of each neuron. To account for potential low-frequency drift in the baseline, the GMM was applied along a moving window of 2,500 frames (500 seconds). The fluorescence of each neuron at each time point t was then normalized to the moving baseline to calculate $\Delta F/F = F_t - F_{baseline} / F_{baseline}$. All subsequent analysis was performed using custom code written in MATLAB (R2022b).

Hierarchical clustering of pooled averaged responses

ΔF/F in response to all 6 odors were averaged across trials then Z-scored. The resulting trial-average values from the following time bins were averaged across time: the first second during each odor, the last second during each odor, and the first second after each odor. The resulting 18-element vectors were sorted into 6 clusters after agglomerative hierarchical clustering using Euclidean distance and Ward linkage.

Responsiveness criteria

To determine how many neurons were responsive to a given odor, we compared ΔF/F at each frame during the 2 second odor period against a pooled distribution of ΔF/F values from the 2-seconds prior to odor onset using a Wilcoxon rank sum test. The resulting p-values were evaluated with Holm-Bonferroni correction to ensure that familywise error rate (FWER) was below 0.05. We also counted the number of neurons that were significantly responsive for at least 4 frames during the odor period to report the total percentage of responsive neurons during odor.

Single-neuron 6-odor classifiers

To test how reliably a single neuron's fluorescence could discriminate between the 6 odors, we assessed the performance of multinomial regression (MNR) classifiers trained on a single neuron's responses to 6 odors. For each neuron and odor pair, we averaged the ΔF/F during

the last second of the odor exposure for each trial then Z-scored across all trials. The resulting 120-element vector was used to train the MNR classifiers. The 5-fold cross-validated accuracies are reported and plotted as violin plots.[114] As a control for each neuron, 100 shuffled classifiers were trained on the data with the odor labels randomly assigned.

Pairwise euclidean distance

To quantify the differences among population-level responses to the 6 odors, we quantified the pairwise Euclidean distance between the trajectories of odor responses. First, we subtracted the ΔF/F values during the 2 seconds prior to odor delivery from each frame then averaged these values across trials for each odor. The pairwise Euclidean distance at each frame was computed for each odor pair and normalized to the maximum pairwise distance measured in all odor pairs at any time bin. These calculations were carried out separately for each animal and then averaged across biological replicates to report the mean and the standard error.

Population classifiers

To assess the discriminability of odor responses in high-dimensional space, we measured the accuracy of error-correcting output codes (ecoc) classifiers. At each time point relative to odor delivery, we pooled ΔF/F values from all trials during which either odor was presented. These values were then normalized and used to train a multinomial ecoc classifier using a Support Vector Machine (SVM). The accuracy of the classifier was evaluated via 5-fold cross-validation. To compare the classifier accuracies across different numbers of neurons used for training, we randomly selected varying numbers of pooled neurons and used the ΔF/F values during the last second of odor exposure for training.

Behavioral Data Analysis

Behavioral metrics (i.e. performance index, port distance, center distance, open field time, and total distance) for the four-quadrant preference test, open field test, and elevated plus maze were calculated on sets of coordinates created by identifying the centroid of the mouse in real time in video collected from an overhead camera (Basler) at 4 Hz using custom Labview code and outputting the centroid's coordinates for each frame. The mouse was automatically identified by taking a background greyscale image of the behavioral assay's environment at the beginning of each trial and detecting shapes of a minimum size deviating from the background image by a specific threshold. The centroid was then determined by automated generation of a bounding box for the mouse in each frame in real time and recording the coordinate of the centroid of this rectangle.

Four quadrant task data analysis

Mice were tested as previously described.[3] Mice were placed in the chamber for 25 min experiments and tested no more than once per day. The first 10 min served as a baseline test for spatial or temporal bias within the chamber during the trial, and no stimulus of any sort was provided, while the last 15 min were the test of the manipulation. 15 minutes was chosen to balance time courses of odor responses observed in previous experiments, where appetitive

odors tend to yield initial responses that decay, while aversive odors tend to yield responses that grow in magnitude over time. To ensure effects did not arise from ceiling or floor effects in the baseline or from a nonstandard baseline internal state, the mouse had to remain within the stimulus quadrant during the baseline test between ~20-30% of the time or else the experiment was terminated, and the mouse was tested again later. The first 2 minutes of data after the stimulus was introduced were excluded from the analysis to reduce variance and account for novelty of the stimulus without affecting the overall valence of the behavioral response, and the last minute of data was excluded to ensure no minor differences in frames captured could affect analysis. For chemogenetic odor response silencing experiments, animals with vehicle odor responses below an absolute value of 0.1 were excluded from experiments to avoid false negatives from attempting to silence a response that was not observed at baseline, which applied to less than a quarter of overall animals tested across experimental conditions. Performance index represents the percent difference from chance occupancy in the manipulation quadrant, calculated as PI = (P - 25) / 0.25*;* where P is the percentage of time the animal spends in the manipulation quadrant. Mean port distance represents the mean distance of each point to the deepest point into the manipulation quadrant observed at baseline.

Open field test data analysis

For elevated plus maze analysis, all chemogenetic inhibition trials used the entirely of the 10 min test length as a single period, while optogenetic stimulation trials used the mean of the three “OFF” periods to compare to the mean of the two “ON” periods. Three metrics of interest were calculated. Center time was calculated as the proportion of time spent in the middle square of the open field comprising 50% of its total area. Corner time was calculated as the proportion of time spent in the corner squares bounded by the walls and the lines bounding the center region. Time immobile was calculated as the proportion of time when the animal moved less than 1 cm/s for at least a one-second period. Location of the open field and bounding regions was kept constant from trial to trial by registering the apparatus to a bounding box with the same top-down dimensions, and every measured centroid outside of the registered region resulting from shadows cast and other artifacts was interpolated between the closest points before and after within the region.

Elevated plus maze data analysis

For elevated plus maze analysis, all chemogenetic inhibition trials used the entirely of the 10 min test length as a single period, while optogenetic stimulation trials used the mean of the two “OFF” periods to compare to the “ON” period. Three metrics of interest were calculated. Time in the open arms was calculated as the proportion of time spent in the open arms compared to the whole period of interest and did not include time in the center between the two arms. Open arm entries measures number of episodes where the centroid is observed outside of the bounds of the closed arms or the center region, without any minimum time or distance out onto the open arms. Finally, distance was simply calculated as the distance traveled during each period of interest. Location of open and closed arms was kept constant from trial to trial by registering the apparatus to a cross-shaped bounding box with the same top-down dimensions, and every measured centroid outside of the registered region due to factors like the mouse leaning over

the edge of the open arms, among others, was interpolated between the closest points before and after within the region.

Analysis of Single-Nucleus RNA Sequencing Data

Sequence alignment

All samples were processed using Cell Ranger (v5.0.0).[37] All processing was done by using Cell Ranger's implementation of STAR to align sample sequence reads to their pre-built mm10 vm23/Ens98 reference transcriptome index 2020-A, with predicted and non-validated transcripts removed. All sequencing reads were aligned to both the exons and the introns present in the index. Samples were demultiplexed to produce a pair of FASTQ files for each sample. FASTQ files containing raw read sequence information were aligned to the Cell Ranger index using the cellranger count command with --chemistry SC3Pv3 and --include-introns flags enabled. Cell Ranger corrected sequencing errors in cell barcodes to pre-defined sequences in the 10X v3 single-index whitelist within Hamming distance 1. PCR duplicates were removed by selecting unique combinations of corrected cell barcodes, unique molecular identifiers, gene names, and location within the transcript. Raw unfiltered count data was read into R (v4.2.1) using the Seurat package (v4.2.0).[115–118] The final result of the pipeline was a barcode x gene expression matrix for further analysis downstream.

Quality control

We used the raw, unfiltered matrix output from Cell Ranger as the input to the beginning of the pipeline. However, to apply a more stringent filter, the emptyDrops dirichlet-multinomial model from the DropletUtils package (v1.10.2) was applied to each library individually.[119,120] Droplets with less than 100 total counts were used to construct the ambient RNA profile and an FDR threshold below 0.001 was used to select putatively occupied droplets. All barcodes with greater than 1000 UMIs were further assumed non-empty. Most quality filtration choices were heavily influenced by the recommendations presented in pipeComp.[121] All quality control was performed on each library individually prior to merging. Minimal quality filtering for each barcode was performed by setting a floor of 1000 features per barcode for downstream inclusion to ensure the dataset is entirely composed of high-quality nuclei. Next, to remove highly likely multiplet barcodes, barcodes were filtered out if their count depth was more than 5 median absolute deviations above the median count depth. Barcodes were then removed if their proportion of ribosomal or mitochondrial reads was more than 5 interquartile ranges above the 75th percentile (median absolute deviations cannot be used, because in many cases the median absolute deviation is 0). Heterotypic doublets were identified by creating simulated artificial doublets in scDblFinder (v1.4.1), which uses a DoubletFinder-like model to remove barcodes similar to simulated doublets, with an assumed doublet rate of 1% per 1000 nuclei in the library.[122,123] Scater (v1.18.3) was used to produce initial diagnostic tSNE and UMAP plots for visually checking the influence of each above metric on the structure of the data.[124]

Data processing/transformation

All datasets (initially for all nuclei and again for selected subclusters) were formatted into Seurat objects (v4.0.0), merged, and then normalized and transformed individually using the SCTransform (v2) variance stabilizing transform, which performs best according to prior comparisons in pipeComp.[121,125,126] Following the merge, all genes expressed in 3 or fewer nuclei of interest were removed from analysis. SCTransform was run returning Pearson residuals regressing out mitochondrial gene expression, retaining the top 5000 highly variable features. Dimensionality of the dataset was first reduced using principal component analysis, as implemented in Seurat's RunPCA function, retaining the top 50 principal components.[127] Principal components were selected for downstream use by using the lower value of either the number of principal components where the lowest contributes 5% of standard deviation and all cumulatively contribute 90% of the standard deviation, or the number of principal components where the percent change in variation between the consecutive components is lower than 0.1%. These principal components were used as input to the non-linear tSNE and UMAP dimensionality reduction methods as implemented by Seurat's RunTSNE and/or RunUMAP functions with 1000 epochs at 0.5 minimum distance, with otherwise default settings.[128–130]

Clusters were identified via Leiden clustering in latent space using the previously selected principal components as input.[131] Optimal clustering resolution was identified in a supervised manner using clustree, finding the highest resolution for each dataset where clustering remains stable.[132] Cluster annotation was performed in a semi-hierarchical semi-supervised manner, where known marker genes were first used to separate all nuclei into neuronal and non-neuronal cell types, and then these cells were re-analyzed and neurons were respectively separated into glutamatergic and GABAergic neurons, while non-neuronal cells were separated into astrocytes, microglia, macrophages, oligodendrocytes and their precursors/lineage, mural cells, endothelia, and vascular leptomeningeal cells. This lower level of cells was then reanalyzed, and novel cell types were then identified within these more-granular known cell types. For identification of known cell types, clusters expressing the same marker genes were manually merged to ensure all cells of a known type were analyzed together, which did not occur for novel cell type identification. Clusters resulting from specific difference in nuclei quality instead of true changes in gene expression (i.e. markedly lower mean UMI/features per nucleus, increased ribosomal/mitochondrial gene expression proportion) were removed prior to final clustering. Relationships between cell type proportion and plCoA zone were quantitated using propeller, treating each library as an independent replicate.[133]

Differential expression

Marker genes were identified using Wilcoxon rank-sum test as implemented by the FindConservedMarkers function in Seurat, using the region as a grouping variable. Genes were accepted as differentially expressed with a minimum proportion cutoff at 0.1 and minimum fold change at 1.5-fold (log2-fold change of 0.585), with a p-value cutoff of 0.01 after Bonferroni correction. To identify genes differentially expressed by region, single-cell values were converted to pseudo-bulk by batch using the run_de function as implemented in the Libra package (v1.0.0) using default settings with a minimum proportion cutoff at 0.1, and tested for differential expression using edgeR's likelihood ratio test.[134] Zone-specific gene expression was identified by comparing batches from the two isolated zones.

Analysis of Spatial Transcriptomics Data

Sequence and image alignment

All samples were processed using Space Ranger (v1.3.0). All processing was done by using Space Ranger's implementation of STAR to align sample sequence reads to their pre-built mm10 vm23/Ens98 reference transcriptome index 2020-A, with predicted and non-validated transcripts removed, as in snRNA-seq data alignment. Samples were demultiplexed to produce a pair of FASTQ files for each sample. FASTQ files containing raw read sequence information were aligned to the index using the spaceranger count command. Space Ranger corrected sequencing errors in cell barcodes to pre-defined sequences in the single-index whitelist within Hamming distance 1. PCR duplicates were removed by selecting unique combinations of corrected cell barcodes, unique molecular identifiers, gene names, and location within the transcript. Imaging data was processed using automatic fiducial alignment and tissue detection on a brightfield input.

Data processing/transformation

We used the image-filtered matrix output from Space Ranger as the input to the beginning of the pipeline. In a similar manner to snRNA-seq data, all datasets were formatted into Seurat objects (v5.0.0), merged, and then normalized and transformed using the SCTransform (v2) variance stabilizing transform. SCTransform was run returning Pearson residuals regressing out mitochondrial gene expression, retaining the top 5000 highly variable features. Dimensionality of the dataset was first reduced using principal component analysis, as implemented in Seurat's RunPCA function, retaining the top 50 principal components, all of which were used in downstream processing. These principal components were used as input to the non-linear tSNE and UMAP dimensionality reduction methods as implemented by Seurat's RunTSNE and/or RunUMAP functions with 1000 epochs at 0.2 minimum distance, with otherwise default settings. Clusters were identified via Leiden clustering in latent space using all 50 principal components as input. Optimal clustering resolution was identified in a supervised manner using clustree, finding the highest resolution for each dataset where clustering remains stable, choosing a resolution of 0.7. Cluster annotation was performed in a semi-supervised manner, observing where in captured plCoA regions each cluster’s spots localized to. For clusters that could not be annotated from spatial location alone (e.g. OLG), marker genes were examined to determine the molecular identity of relevant spots. Spatial data was projected onto neuronal molecular cell types from snRNA-seq data and cell type likelihood was predicted using Seurat’s FindTransferAnchors and TransferData functions using snRNA-seq data as a reference and plCoA spatial data as the query, using all 50 PCs. Prediction of a minority of subtypes failed, likely due to low abundance in tissue and/or due to mediolateral spatial differences, alluded to in a separate study, causing the section not to intersect with the part of the tissue containing the relevant neuronal subtypes.[135] Glutamatergic and GABAergic molecular subtype likelihoods were predicted separately to remove noise and increase modeled prediction confidence.

Histological Image Analysis

Registration and localization

Histology for all animals and samples was examined prior to inclusion. Localization within the coronal plane was determined by registering the coronal slice to the Allen Brain Atlas via the ABBA plugin, using elastix to sequentially perform affine and spline registration of the DAPI channel of the slice to the Nissl channel of the atlas.[136,137] The region of interest was then compared to the Paxinos and Franklin atlas to confirm localization, and find the region's anteroposterior distance from bregma.[36] This combined method was used because sections cannot be accurately registered to the Paxinos and Franklin atlas due to low Z-resolution, while the Allen Brain Atlas lacks information about anteroposterior distance from bregma. Exclusion based on histology would occur when most of the intervention fell outside of the region of interest. Due to these differences, individual representative images use the individually registered Allen Reference Atlas schematics with the comparable Paxinos and Franklin anteroposterior coordinates noted, while consolidated targeting schematics use the Paxinos and Franklin atlas for visualization.

Quantification of histological fluorescence

In anterograde tracing experiments, output quantification was performed based on background-corrected total fluorescence. For all non-collateralization anterograde experiments, fluorescence intensities were quantified using FIJI (v2.9.0) throughout the whole brain in a series of evenly-space 50 µm coronal sections, manually segmenting by region with all settings held constant within experiments.[138] For collateralization experiments, we exclusively examined fluorescence in the MeA and NAc. We calculated background-corrected total fluorescence using the equation $F_{total} = ID - (Area \times F_{background})$, where F_{total} is the background-corrected total fluorescence, *ID* is the integrated density, and $F_{background}$ is the mean background fluorescence measured from four randomly selected areas per section not receiving input from plCoA. Overall proportion was calculated by taking the sum of background-corrected fluorescence values across all sections for a given region and dividing it by the sum of all background-corrected values. For retrograde experiments, we quantified number of cells using the Cell Counter plugin (v3.0.0) in FIJI. The sagittal brain slices containing the plCoA were then compared to Paxinos and Franklin, 5th Edition to count the number of cells found per distance away from bregma from -1.3 to -2.5 mm in increments of 100 µm.[36] At least two sections per region per animal were analyzed. Representative images were produced from slide scanner image output, with background subtraction and uniform brightness and contrast thresholds applied equally to all fluorescent channels in FIJI to avoid potential distortion of visible fluorescence levels.

Quantification and analysis of RNAscope images

RNAscope images were analyzed as previously described.[86] Images were opened in FIJI and individual Z-planes encompassing the entire ROI were selected from each image for further image processing. Background was subtracted from all channels in all images using the subtract background feature. Masks of each region were drawn based on the mouse brain atlas, and images were then saved as 8bit TIFFs for further cell and puncta identification in CellProfiler (v4.2.4).[36,139] Image TIFFs were run through CellProfiler using an optimized version of the CellProfiler Colocalization pipeline. The pipeline was optimized to identify DAPI labelled cells (15-45 pixels in diameter) and then subsequently identify mRNA puncta (4-10 pixels in

diameter). DAPI cell detection was further restricted by shrinking DAPI ROIs by 1 pixel. Puncta overlapping with DAPI-identified cells (using the relate objects module) were considered for analysis to assess the level of mRNA expression per cell. To determine if cells were expressing mRNA, a threshold of 5 or more puncta within twice the diameter of nucleus centered over the nucleus was used.[140] Total number and density of *Slc17a6*+ and *Slc17a7*+ cells in each region of interest were calculated from CellProfiler .csv outputs using custom R scripts.

References

1. Stowers, L., Cameron, P., and Keller, J.A. (2013). Ominous Odors: olfactory control of instinctive fear and aggression in mice. Curr. Opin. Neurobiol. *23*, 339–345. https://doi.org/10.1016/j.conb.2013.01.007.

2. Stowers, L., and Kuo, T.-H. (2015). Mammalian pheromones; emerging properties and mechanisms of detection. Curr. Opin. Neurobiol. *34*, 103–109. https://doi.org/10.1016/j.conb.2015.02.005.

3. Root, C.M., Denny, C.A., Hen, R., and Axel, R. (2014). The participation of cortical amygdala in innate, odour-driven behaviour. Nature *515*, 269–273. https://doi.org/10.1038/NATURE13897.

4. Li, Q., and Liberles, S.D. (2015). Aversion and Attraction through Olfaction. Curr. Biol. *25*, R120–R129. https://doi.org/10.1016/j.cub.2014.11.044.

5. Hayden, S., Bekaert, M., Crider, T.A., Mariani, S., Murphy, W.J., and Teeling, E.C. (2010). Ecological adaptation determines functional mammalian olfactory subgenomes. Genome Res. *20*, 1–9. https://doi.org/10.1101/gr.099416.109.

6. Saraiva, L.R., Riveros-McKay, F., Mezzavilla, M., Abou-Moussa, E.H., Arayata, C.J., Makhlouf, M., Trimmer, C., Ibarra-Soria, X., Khan, M., Van Gerven, L., et al. (2019). A transcriptomic atlas of mammalian olfactory mucosae reveals an evolutionary influence on food odor detection in humans. Sci. Adv. *5*, eaax0396. https://doi.org/10.1126/sciadv.aax0396.

7. Ibarra-Soria, X., Nakahara, T.S., Lilue, J., Jiang, Y., Trimmer, C., Souza, M.A., Netto, P.H., Ikegami, K., Murphy, N.R., Kusma, M., et al. (2017). Variation in olfactory neuron repertoires is genetically controlled and environmentally modulated. eLife *6*, e21476. https://doi.org/10.7554/eLife.21476.

8. Tye, K.M. (2018). Neural Circuit Motifs in Valence Processing. Neuron *100*, 436–452. https://doi.org/10.1016/j.neuron.2018.10.001.

9. Dewan, A., Pacifico, R., Zhan, R., Rinberg, D., and Bozza, T. (2013). Non-redundant coding of aversive odours in the main olfactory pathway. Nature *497*, 486–489. https://doi.org/10/f4xchh.

10. Li, Q., Korzan, W.J., Ferrero, D.M., Chang, R.B., Roy, D.S., Buchi, M., Lemon, J.K., Kaur, A.W., Stowers, L., Fendt, M., et al. (2013). Synchronous Evolution of an Odor Biosynthesis Pathway and Behavioral Response. Curr. Biol. *23*, 11–20. https://doi.org/10.1016/j.cub.2012.10.047.

11. Semmelhack, J.L., and Wang, J.W. (2009). Select Drosophila glomeruli mediate innate olfactory attraction and aversion. Nature *459*, 218–223. https://doi.org/10.1038/nature07983.

12. Beyeler, A., Namburi, P., Glober, G.F., Simonnet, C., Calhoon, G.G., Conyers, G.F., Luck, R., Wildes, C.P., and Tye, K.M. (2016). Divergent Routing of Positive and Negative

Information from the Amygdala during Memory Retrieval. Neuron *90*, 348–361. https://doi.org/10.1016/j.neuron.2016.03.004.

13. Chen, Y., Chen, X., Baserdem, B., Zhan, H., Li, Y., Davis, M.B., Kebschull, J.M., Zador, A.M., Koulakov, A.A., and Albeanu, D.F. (2022). High-throughput sequencing of single neuron projections reveals spatial organization in the olfactory cortex. Cell *185*, 4117-4134.e28. https://doi.org/10.1016/j.cell.2022.09.038.

14. Sosulski, D.L., Lissitsyna Bloom, M., Cutforth, T., Axel, R., and Datta, S.R. (2011). Distinct representations of olfactory information in different cortical centres. Nature *472*, 213–219. https://doi.org/10/fdwfsk.

15. Miyamichi, K., Amat, F., Moussavi, F., Wang, C., Wickersham, I., Wall, N.R., Taniguchi, H., Tasic, B., Huang, Z.J., He, Z., et al. (2011). Cortical representations of olfactory input by trans-synaptic tracing. Nature *472*, 191–199. https://doi.org/10/bmj88g.

16. Wang, I.-H., Murray, E., Andrews, G., Jiang, H.-C., Park, S.J., Donnard, E., Durán-Laforet, V., Bear, D.M., Faust, T.E., Garber, M., et al. (2022). Spatial transcriptomic reconstruction of the mouse olfactory glomerular map suggests principles of odor processing. Nat. Neurosci. *25*, 484–492. https://doi.org/10.1038/s41593-022-01030-8.

17. Iurilli, G., and Datta, S.R. (2017). Population Coding in an Innately Relevant Olfactory Area. Neuron *93*, 1180-1197.e7. https://doi.org/10/f9tpmx.

18. Beyeler, A., Chang, C.-J., Silvestre, M., Lévêque, C., Namburi, P., Wildes, C.P., and Tye, K.M. (2018). Organization of Valence-Encoding and Projection-Defined Neurons in the Basolateral Amygdala. Cell Rep. *22*, 905–918. https://doi.org/10/gg6473.

19. Kim, J., Pignatelli, M., Xu, S., Itohara, S., and Tonegawa, S. (2016). Antagonistic negative and positive neurons of the basolateral amygdala. Nat. Neurosci. *19*, 1636–1646. https://doi.org/10.1038/nn.4414.

20. Tsuji, T., Tsuji, C., Lozic, M., Ludwig, M., and Leng, G. (2019). Coding of odors in the anterior olfactory nucleus. Physiol. Rep. *7*, e14284. https://doi.org/10.14814/phy2.14284.

21. Malnic, B., Hirono, J., Sato, T., and Buck, L.B. (1999). Combinatorial Receptor Codes for Odors. Cell *96*, 713–723. https://doi.org/10.1016/S0092-8674(00)80581-4.

22. Stettler, D.D., and Axel, R. (2009). Representations of Odor in the Piriform Cortex. Neuron *63*, 854–864. https://doi.org/10.1016/j.neuron.2009.09.005.

23. Nara, K., Saraiva, L.R., Ye, X., and Buck, L.B. (2011). A Large-Scale Analysis of Odor Coding in the Olfactory Epithelium. J. Neurosci. *31*, 9179–9191. https://doi.org/10.1523/JNEUROSCI.1282-11.2011.

24. Soucy, E.R., Albeanu, D.F., Fantana, A.L., Murthy, V.N., and Meister, M. (2009). Precision and diversity in an odor map on the olfactory bulb. Nat. Neurosci. *12*, 210–220. https://doi.org/10.1038/nn.2262.

25. Lee, D., Liu, L., and Root, C.M. (2023). Transformation of value signaling in a striatopallidal circuit. eLife *12*. https://doi.org/10.7554/eLife.90976.

26. Chae, H., Kepple, D.R., Bast, W.G., Murthy, V.N., Koulakov, A.A., and Albeanu, D.F. (2019). Mosaic representations of odors in the input and output layers of the mouse olfactory bulb. Nat. Neurosci. *22*, 1306–1317. https://doi.org/10.1038/s41593-019-0442-z.

27. Ma, L., Qiu, Q., Gradwohl, S., Scott, A., Yu, E.Q., Alexander, R., Wiegraebe, W., and Yu, C.R. (2012). Distributed representation of chemical features and tunotopic organization of glomeruli in the mouse olfactory bulb. Proc. Natl. Acad. Sci. *109*, 5481–5486. https://doi.org/10.1073/pnas.1117491109.

28. Roland, B., Deneux, T., Franks, K.M., Bathellier, B., and Fleischmann, A. (2017). Odor identity coding by distributed ensembles of neurons in the mouse olfactory cortex. eLife *6*, e26337. https://doi.org/10.7554/eLife.26337.

29. Payton, C.A., Wilson, D.A., and Wesson, D.W. (2012). Parallel odor processing by two anatomically distinct olfactory bulb target structures. PloS One *7*, e34926. https://doi.org/10.1371/journal.pone.0034926.

30. Cousens, G.A. (2020). Characterization of odor-evoked neural activity in the olfactory peduncle. IBRO Rep. *9*, 157–163. https://doi.org/10.1016/j.ibror.2020.07.010.

31. Peng, Y., Gillis-Smith, S., Jin, H., Tränkner, D., Ryba, N.J.P., and Zuker, C.S. (2015). Sweet and bitter taste in the brain of awake behaving animals. Nature *527*, 512–515. https://doi.org/10.1038/nature15763.

32. Pashkovski, S.L., Iurilli, G., Brann, D., Chicharro, D., Drummey, K., Franks, K., Panzeri, S., and Datta, S.R. (2020). Structure and flexibility in cortical representations of odor space. Nature *583*, 253–258. https://doi.org/10.1038/s41586-020-2451-1.

33. Wiltschko, A.B., Johnson, M.J., Iurilli, G., Peterson, R.E., Katon, J.M., Pashkovski, S.L., Abraira, V.E., Adams, R.P., and Datta, S.R. (2015). Mapping Sub-Second Structure in Mouse Behavior. Neuron *88*, 1121–1135. https://doi.org/10.1016/j.neuron.2015.11.031.

34. Wang, L., Gillis-Smith, S., Peng, Y., Zhang, J., Chen, X., Salzman, C.D., Ryba, N.J.P., and Zuker, C.S. (2018). The coding of valence and identity in the mammalian taste system. Nature *558*, 127–131. https://doi.org/10/gdq4gk.

35. Chen, X., Gabito, M., Peng, Y., Ryba, N.J.P., and Zuker, C.S. (2011). A Gustotopic Map of Taste Qualities in the Mammalian Brain. Science *333*, 1262–1266. https://doi.org/10/cv4x7s.

36. Paxinos and Franklin's the Mouse Brain in Stereotaxic Coordinates, Compact - 5th Edition https://www.elsevier.com/books/paxinos-and-franklins-the-mouse-brain-in-stereotaxic-coordinates-compact/franklin/978-0-12-816159-3.

37. Zheng, G.X.Y., Terry, J.M., Belgrader, P., Ryvkin, P., Bent, Z.W., Wilson, R., Ziraldo, S.B., Wheeler, T.D., McDermott, G.P., Zhu, J., et al. (2017). Massively parallel digital transcriptional profiling of single cells. Nat. Commun. *8*, 14049. https://doi.org/10/f9mbtp.

38. Tasic, B., Menon, V., Nguyen, T.N., Kim, T.K., Jarsky, T., Yao, Z., Levi, B., Gray, L.T., Sorensen, S.A., Dolbeare, T., et al. (2016). Adult mouse cortical cell taxonomy revealed by single cell transcriptomics. Nat. Neurosci. *19*, 335–346. https://doi.org/10/f778w5.

1774 39. Zeisel, A., Hochgerner, H., Lönnerberg, P., Johnsson, A., Memic, F., van der Zwan, J.,
1775 Häring, M., Braun, E., Borm, L.E., La Manno, G., et al. (2018). Molecular Architecture of the
1776 Mouse Nervous System. Cell *174*, 999-1014.e22. https://doi.org/10/gdxxnt.

1777 40. Marques, S., Zeisel, A., Codeluppi, S., van Bruggen, D., Mendanha Falcão, A., Xiao, L., Li,
1778 H., Häring, M., Hochgerner, H., Romanov, R.A., et al. (2016). Oligodendrocyte
1779 heterogeneity in the mouse juvenile and adult central nervous system. Science *352*, 1326–
1780 1329. https://doi.org/10.1126/science.aaf6463.

1781 41. Yasuda, K., Cline, C., Vogel, P., Onciu, M., Fatima, S., Sorrentino, B.P., Thirumaran, R.K.,
1782 Ekins, S., Urade, Y., Fujimori, K., et al. (2013). Drug Transporters on Arachnoid Barrier
1783 Cells Contribute to the Blood–Cerebrospinal Fluid Barrier. Drug Metab. Dispos. *41*, 923–
1784 931. https://doi.org/10.1124/dmd.112.050344.

1785 42. Tasic, B., Yao, Z., Graybuck, L.T., Smith, K.A., Nguyen, T.N., Bertagnolli, D., Goldy, J.,
1786 Garren, E., Economo, M.N., Viswanathan, S., et al. (2018). Shared and distinct
1787 transcriptomic cell types across neocortical areas. Nature *563*, 72. https://doi.org/10/gfgqmf.

1788 43. Yao, Z., Velthoven, C.T.J. van, Nguyen, T.N., Goldy, J., Sedeno-Cortes, A.E., Baftizadeh,
1789 F., Bertagnolli, D., Casper, T., Chiang, M., Crichton, K., et al. (2021). A taxonomy of
1790 transcriptomic cell types across the isocortex and hippocampal formation. Cell *184*, 3222.
1791 https://doi.org/10.1016/j.cell.2021.04.021.

1792 44. Harris, J.A., Hirokawa, K.E., Sorensen, S.A., Gu, H., Mills, M., Ng, L.L., Bohn, P., Mortrud,
1793 M., Ouellette, B., Kidney, J., et al. (2014). Anatomical characterization of Cre driver mice for
1794 neural circuit mapping and manipulation. Front. Neural Circuits *8*, 76.
1795 https://doi.org/10.3389/fncir.2014.00076.

1796 45. Vong, L., Ye, C., Yang, Z., Choi, B., Chua, S., and Lowell, B.B. (2011). Leptin action on
1797 GABAergic neurons prevents obesity and reduces inhibitory tone to POMC neurons. Neuron
1798 *71*, 142–154. https://doi.org/10.1016/j.neuron.2011.05.028.

1799 46. Krashes, M.J., Koda, S., Ye, C., Rogan, S.C., Adams, A.C., Cusher, D.S., Maratos-Flier, E.,
1800 Roth, B.L., and Lowell, B.B. (2011). Rapid, reversible activation of AgRP neurons drives
1801 feeding behavior in mice. J Clin Invest *121*, 1424–1428. https://doi.org/10/bd3bv9.

1802 47. Ikemoto, S. (2007). Dopamine reward circuitry: two projection systems from the ventral
1803 midbrain to the nucleus accumbens-olfactory tubercle complex. Brain Res. Rev. *56*, 27–78.
1804 https://doi.org/10.1016/j.brainresrev.2007.05.004.

1805 48. Müller, M., and Fendt, M. (2006). Temporary inactivation of the medial and basolateral
1806 amygdala differentially affects TMT-induced fear behavior in rats. Behav. Brain Res. *167*,
1807 57–62. https://doi.org/10.1016/j.bbr.2005.08.016.

1808 49. Lebow, M.A., and Chen, A. (2016). Overshadowed by the amygdala: the bed nucleus of the
1809 stria terminalis emerges as key to psychiatric disorders. Mol. Psychiatry *21*, 450–463.
1810 https://doi.org/10.1038/mp.2016.1.

1811 50. Sedwick, V.M., and Autry, A.E. (2022). Anatomical and molecular features of the
1812 amygdalohippocampal transition area and its role in social and emotional behavior

processes. Neurosci. Biobehav. Rev. *142*, 104893. https://doi.org/10.1016/j.neubiorev.2022.104893.

51. Pardo-Bellver, C., Vila-Martin, M.E., Martínez-Bellver, S., Villafranca-Faus, M., Teruel-Sanchis, A., Savarelli-Balsamo, C.A., Drabik, S.M., Martínez-Ricós, J., Cervera-Ferri, A., Martínez-García, F., et al. (2022). Neural activity patterns in the chemosensory network encoding vomeronasal and olfactory information in mice. Front. Neuroanat. *16*. https://doi.org/10.3389/fnana.2022.988015.

52. Kaas, J.H. (1997). Topographic maps are fundamental to sensory processing. Brain Res. Bull. *44*, 107–112. https://doi.org/10.1016/s0361-9230(97)00094-4.

53. Garrett, M.E., Nauhaus, I., Marshel, J.H., and Callaway, E.M. (2014). Topography and Areal Organization of Mouse Visual Cortex. J. Neurosci. *34*, 12587–12600. https://doi.org/10.1523/JNEUROSCI.1124-14.2014.

54. Kaas, J.H., Nelson, R.J., Sur, M., Lin, C.-S., and Merzenich, M.M. (1979). Multiple Representations of the Body Within the Primary Somatosensory Cortex of Primates. Science *204*, 521–523. https://doi.org/10.1126/science.107591.

55. Schreiner, C.E., and Winer, J.A. (2007). Auditory Cortex Mapmaking: Principles, Projections, and Plasticity. Neuron *56*, 356–365. https://doi.org/10.1016/j.neuron.2007.10.013.

56. Imai, T., Sakano, H., and Vosshall, L.B. (2010). Topographic Mapping—The Olfactory System. Cold Spring Harb. Perspect. Biol. *2*, a001776. https://doi.org/10.1101/cshperspect.a001776.

57. Auffarth, B. (2013). Understanding smell--the olfactory stimulus problem. Neurosci. Biobehav. Rev. *37*, 1667–1679. https://doi.org/10.1016/j.neubiorev.2013.06.009.

58. Ressler, K.J., Sullivan, S.L., and Buck, L.B. (1993). A zonal organization of odorant receptor gene expression in the olfactory epithelium. Cell *73*, 597–609. https://doi.org/10/b7gqvk.

59. Zapiec, B., and Mombaerts, P. (2020). The Zonal Organization of Odorant Receptor Gene Choice in the Main Olfactory Epithelium of the Mouse. Cell Rep. *30*, 4220-4234.e5. https://doi.org/10.1016/j.celrep.2020.02.110.

60. Pacifico, R., Dewan, A., Cawley, D., Guo, C., and Bozza, T. (2012). An olfactory subsystem that mediates high-sensitivity detection of volatile amines. Cell Rep. *2*, 76–88. https://doi.org/10/gfgp62.

61. Kobayakawa, K., Kobayakawa, R., Matsumoto, H., Oka, Y., Imai, T., Ikawa, M., Okabe, M., Ikeda, T., Itohara, S., Kikusui, T., et al. (2007). Innate versus learned odour processing in the mouse olfactory bulb. Nature *450*, 503–508. https://doi.org/10/d899x4.

62. Midroit, M., Chalençon, L., Renier, N., Milton, A., Thevenet, M., Sacquet, J., Breton, M., Forest, J., Noury, N., Richard, M., et al. (2021). Neural processing of the reward value of pleasant odorants. Curr. Biol. CB *31*, 1592-1605.e9. https://doi.org/10.1016/j.cub.2021.01.066.

1851 63. Kermen, F., Midroit, M., Kuczewski, N., Forest, J., Thévenet, M., Sacquet, J., Benetollo, C.,
1852 Richard, M., Didier, A., and Mandairon, N. (2016). Topographical representation of odor
1853 hedonics in the olfactory bulb. Nat. Neurosci. *19*, 876–878. https://doi.org/10.1038/nn.4317.

1854 64. Choi, G.B., Dong, H., Murphy, A.J., Valenzuela, D.M., Yancopoulos, G.D., Swanson, L.W.,
1855 and Anderson, D.J. (2005). Lhx6 Delineates a Pathway Mediating Innate Reproductive
1856 Behaviors from the Amygdala to the Hypothalamus. Neuron *46*, 647–660.
1857 https://doi.org/10.1016/j.neuron.2005.04.011.

1858 65. Cohn, R., Morantte, I., and Ruta, V. (2015). Coordinated and Compartmentalized
1859 Neuromodulation Shapes Sensory Processing in Drosophila. Cell *163*, 1742–1755.
1860 https://doi.org/10.1016/j.cell.2015.11.019.

1861 66. Levitan, D., Lin, J.-Y., Wachutka, J., Mukherjee, N., Nelson, S.B., and Katz, D.B. (2019).
1862 Single and population coding of taste in the gustatory cortex of awake mice. J.
1863 Neurophysiol. *122*, 1342–1356. https://doi.org/10.1152/jn.00357.2019.

1864 67. Chen, K., Kogan, J.F., and Fontanini, A. (2021). Spatially Distributed Representation of
1865 Taste Quality in the Gustatory Insular Cortex of Behaving Mice. Curr. Biol. *31*, 247-256.e4.
1866 https://doi.org/10.1016/j.cub.2020.10.014.

1867 68. Fletcher, M.L., Ogg, M.C., Lu, L., Ogg, R.J., and Boughter, J.D. (2017). Overlapping
1868 Representation of Primary Tastes in a Defined Region of the Gustatory Cortex. J. Neurosci.
1869 *37*, 7595–7605. https://doi.org/10/gbsjxs.

1870 69. Lavi, K., Jacobson, G.A., Rosenblum, K., and Lüthi, A. (2018). Encoding of Conditioned
1871 Taste Aversion in Cortico-Amygdala Circuits. Cell Rep. *24*, 278–283.
1872 https://doi.org/10.1016/j.celrep.2018.06.053.

1873 70. Erö, C., Gewaltig, M.-O., Keller, D., and Markram, H. (2018). A Cell Atlas for the Mouse
1874 Brain. Front. Neuroinformatics *12*. https://doi.org/10/ggc9xg.

1875 71. Cembrowski, M.S., Phillips, M.G., DiLisio, S.F., Shields, B.C., Winnubst, J., Chandrashekar,
1876 J., Bas, E., and Spruston, N. (2018). Dissociable Structural and Functional Hippocampal
1877 Outputs via Distinct Subiculum Cell Classes. Cell *173*, 1280-1292.e18.
1878 https://doi.org/10/gdb82r.

1879 72. Cembrowski, M.S., and Spruston, N. (2019). Heterogeneity within classical cell types is the
1880 rule: lessons from hippocampal pyramidal neurons. Nat. Rev. Neurosci. *20*, 193–204.
1881 https://doi.org/10.1038/s41583-019-0125-5.

1882 73. Ding, S.-L., Yao, Z., Hirokawa, K.E., Nguyen, T.N., Graybuck, L.T., Fong, O., Bohn, P., Ngo,
1883 K., Smith, K.A., Koch, C., et al. (2020). Distinct Transcriptomic Cell Types and Neural
1884 Circuits of the Subiculum and Prosubiculum along the Dorsal-Ventral Axis. Cell Rep. *31*,
1885 107648. https://doi.org/10/gg63q5.

1886 74. Cembrowski, M.S., Wang, L., Lemire, A.L., Copeland, M., DiLisio, S.F., Clements, J., and
1887 Spruston, N. (2018). The subiculum is a patchwork of discrete subregions. eLife *7*, e37701.
1888 https://doi.org/10/gg63q4.

75. Scala, F., Kobak, D., Bernabucci, M., Bernaerts, Y., Cadwell, C.R., Castro, J.R., Hartmanis, L., Jiang, X., Laturnus, S., Miranda, E., et al. (2021). Phenotypic variation of transcriptomic cell types in mouse motor cortex. Nature *598*, 144–150. https://doi.org/10.1038/s41586-020-2907-3.

76. Gouwens, N.W., Sorensen, S.A., Baftizadeh, F., Budzillo, A., Lee, B.R., Jarsky, T., Alfiler, L., Baker, K., Barkan, E., Berry, K., et al. (2020). Integrated Morphoelectric and Transcriptomic Classification of Cortical GABAergic Cells. Cell *183*, 935-953.e19. https://doi.org/10.1016/j.cell.2020.09.057.

77. O'Leary, T.P., Sullivan, K.E., Wang, L., Clements, J., Lemire, A.L., and Cembrowski, M.S. (2020). Extensive and spatially variable within-cell-type heterogeneity across the basolateral amygdala. eLife *9*, e59003. https://doi.org/10.7554/eLife.59003.

78. Calvigioni, D., Fuzik, J., Le Merre, P., Slashcheva, M., Jung, F., Ortiz, C., Lentini, A., Csillag, V., Graziano, M., Nikolakopoulou, I., et al. (2023). Esr1+ hypothalamic-habenula neurons shape aversive states. Nat. Neurosci. *26*, 1245–1255. https://doi.org/10.1038/s41593-023-01367-8.

79. Phillips, J.W., Schulmann, A., Hara, E., Winnubst, J., Liu, C., Valakh, V., Wang, L., Shields, B.C., Korff, W., Chandrashekar, J., et al. (2019). A repeated molecular architecture across thalamic pathways. Nat. Neurosci. *22*, 1925. https://doi.org/10.1038/s41593-019-0483-3.

80. Mandelbaum, G., Taranda, J., Haynes, T.M., Hochbaum, D.R., Huang, K.W., Hyun, M., Venkataraju, K.U., Straub, C., Wang, W., Robertson, K., et al. (2019). Distinct Cortical-Thalamic-Striatal Circuits through the Parafascicular Nucleus. Neuron *102*, 636-652.e7. https://doi.org/10.1016/j.neuron.2019.02.035.

81. Hochgerner, H., Singh, S., Tibi, M., Lin, Z., Skarbianskis, N., Admati, I., Ophir, O., Reinhardt, N., Netser, S., Wagner, S., et al. (2023). Neuronal types in the mouse amygdala and their transcriptional response to fear conditioning. Nat. Neurosci. *26*, 2237–2249. https://doi.org/10.1038/s41593-023-01469-3.

82. Klingler, E. (2017). Development and Organization of the Evolutionarily Conserved Three-Layered Olfactory Cortex. eNeuro *4*. https://doi.org/10.1523/ENEURO.0193-16.2016.

83. Shi, H., He, Y., Zhou, Y., Huang, J., Maher, K., Wang, B., Tang, Z., Luo, S., Tan, P., Wu, M., et al. (2023). Spatial atlas of the mouse central nervous system at molecular resolution. Nature *622*, 552–561. https://doi.org/10.1038/s41586-023-06569-5.

84. Yao, Z., van Velthoven, C.T.J., Kunst, M., Zhang, M., McMillen, D., Lee, C., Jung, W., Goldy, J., Abdelhak, A., Aitken, M., et al. (2023). A high-resolution transcriptomic and spatial atlas of cell types in the whole mouse brain. Nature *624*, 317–332. https://doi.org/10.1038/s41586-023-06812-z.

85. Zhang, M., Pan, X., Jung, W., Halpern, A.R., Eichhorn, S.W., Lei, Z., Cohen, L., Smith, K.A., Tasic, B., Yao, Z., et al. (2023). Molecularly defined and spatially resolved cell atlas of the whole mouse brain. Nature *624*, 343–354. https://doi.org/10.1038/s41586-023-06808-9.

86. Mills, F., Lee, C.R., Howe, J.R., Li, H., Shao, S., Keisler, M.N., Lemieux, M.E., Taschbach, F.H., Keyes, L.R., Borio, M., et al. (2022). Amygdalostriatal transition zone neurons encode

sustained valence to direct conditioned behaviors. Preprint at bioRxiv, https://doi.org/10.1101/2022.10.28.514263 https://doi.org/10.1101/2022.10.28.514263.

87. Singer, W. (2021). Recurrent dynamics in the cerebral cortex: Integration of sensory evidence with stored knowledge. Proc. Natl. Acad. Sci. *118*, e2101043118. https://doi.org/10.1073/pnas.2101043118.

88. Floresco, S.B. (2015). The Nucleus Accumbens: An Interface Between Cognition, Emotion, and Action. Httpsdoiorg101146annurev-Psych-010213-115159. https://doi.org/10.1146/annurev-psych-010213-115159.

89. Petrulis, A. (2020). Chapter 2 - Structure and function of the medial amygdala. In Handbook of Behavioral Neuroscience Handbook of Amygdala Structure and Function., J. H. Urban and J. A. Rosenkranz, eds. (Elsevier), pp. 39–61. https://doi.org/10.1016/B978-0-12-815134-1.00002-7.

90. Day, H.E.W., Masini, C.V., and Campeau, S. (2004). The pattern of brain c-fos mRNA induced by a component of fox odor, 2,5-dihydro-2,4,5-trimethylthiazoline (TMT), in rats, suggests both systemic and processive stress characteristics. Brain Res. *1025*, 139–151. https://doi.org/10.1016/j.brainres.2004.07.079.

91. Saito, H., Nishizumi, H., Suzuki, S., Matsumoto, H., Ieki, N., Abe, T., Kiyonari, H., Morita, M., Yokota, H., Hirayama, N., et al. (2017). Immobility responses are induced by photoactivation of single glomerular species responsive to fox odour TMT. Nat. Commun. *8*, 1–10. https://doi.org/10.1038/ncomms16011.

92. Zador, A.M. (2019). A critique of pure learning and what artificial neural networks can learn from animal brains. Nat. Commun. *10*, 3770. https://doi.org/10.1038/s41467-019-11786-6.

93. Koulakov, A., Shuvaev, S., Lachi, D., and Zador, A. (2022). Encoding innate ability through a genomic bottleneck. Preprint at bioRxiv, https://doi.org/10.1101/2021.03.16.435261 https://doi.org/10.1101/2021.03.16.435261.

94. Barabási, D.L., Beynon, T., Katona, Á., and Perez-Nieves, N. (2023). Complex computation from developmental priors. Nat. Commun. *14*, 2226. https://doi.org/10.1038/s41467-023-37980-1.

95. Qiu, Q., Wu, Y., Ma, L., and Yu, C.R. (2021). Encoding innately recognized odors via a generalized population code. Curr. Biol. *31*, 1813-1825.e4. https://doi.org/10.1016/j.cub.2021.01.094.

96. Illig, K.R., and Haberly, L.B. (2003). Odor-evoked activity is spatially distributed in piriform cortex. J. Comp. Neurol. *457*, 361–373. https://doi.org/10.1002/cne.10557.

97. Tritsch, N.X., and Sabatini, B.L. (2012). Dopaminergic modulation of synaptic transmission in cortex and striatum. Neuron *76*, 33–50. https://doi.org/10.1016/j.neuron.2012.09.023.

98. Martiros, N., Kapoor, V., Kim, S.E., and Murthy, V.N. (2022). Distinct representation of cue-outcome association by D1 and D2 neurons in the ventral striatum's olfactory tubercle. eLife *11*, e75463. https://doi.org/10.7554/eLife.75463.

99. Millman, D.J., and Murthy, V.N. (2020). Rapid Learning of Odor–Value Association in the Olfactory Striatum. J. Neurosci. *40*, 4335–4347. https://doi.org/10.1523/JNEUROSCI.2604-19.2020.

100. Gadziola, M.A., Stetzik, L.A., Wright, K.N., Milton, A.J., Arakawa, K., Cortijo, M. del M., and Wesson, D.W. (2020). A Neural System that Represents the Association of Odors with Rewarded Outcomes and Promotes Behavioral Engagement. Cell Rep. *32*. https://doi.org/10.1016/j.celrep.2020.107919.

101. Gadziola, M.A., Tylicki, K.A., Christian, D.L., and Wesson, D.W. (2015). The olfactory tubercle encodes odor valence in behaving mice. J. Neurosci. Off. J. Soc. Neurosci. *35*, 4515–4527. https://doi.org/10.1523/JNEUROSCI.4750-14.2015.

102. Preissl, S., Fang, R., Huang, H., Zhao, Y., Raviram, R., Gorkin, D.U., Zhang, Y., Sos, B.C., Afzal, V., Dickel, D.E., et al. (2018). Single-nucleus analysis of accessible chromatin in developing mouse forebrain reveals cell-type-specific transcriptional regulation. Nat. Neurosci. *21*, 432–439. https://doi.org/10/gc9gx2.

103. Davis, A., Gao, R., and Navin, N.E. (2019). SCOPIT: sample size calculations for single-cell sequencing experiments. BMC Bioinformatics *20*, 566. https://doi.org/10/ggc9ws.

104. Sturchler-Pierrat, C., Abramowski, D., Duke, M., Wiederhold, K.-H., Mistl, C., Rothacher, S., Ledermann, B., Bürki, K., Frey, P., Paganetti, P.A., et al. (1997). Two amyloid precursor protein transgenic mouse models with Alzheimer disease-like pathology. Proc. Natl. Acad. Sci. *94*, 13287–13292. https://doi.org/10.1073/pnas.94.24.13287.

105. Oh, S.W., Harris, J.A., Ng, L., Winslow, B., Cain, N., Mihalas, S., Wang, Q., Lau, C., Kuan, L., Henry, A.M., et al. (2014). A mesoscale connectome of the mouse brain. Nature *508*, 207–214. https://doi.org/10.1038/nature13186.

106. Knowland, D., Lilascharoen, V., Pacia, C.P., Shin, S., Wang, E.H.-J., and Lim, B.K. (2017). Distinct Ventral Pallidal Neural Populations Mediate Separate Symptoms of Depression. Cell *170*, 284-297.e18. https://doi.org/10.1016/j.cell.2017.06.015.

107. Wang, F., Flanagan, J., Su, N., Wang, L.C., Bui, S., Nielson, A., Wu, X., Vo, H.T., Ma, X.J., and Luo, Y. (2012). RNAscope: A novel in situ RNA analysis platform for formalin-fixed, paraffin-embedded tissues. J. Mol. Diagn. *14*, 22–29. https://doi.org/10/dp2pmw.

108. Pratelli, M., Thaker, A., Li, H., Godavarthi, S., and Spitzer, N.C. (2022). Phencyclidine and methamphetamine cause cognitive deficits by changing pyramidal neuron transmitter identity in the prefrontal cortex. Preprint at bioRxiv, https://doi.org/10.1101/2022.06.16.496480 https://doi.org/10.1101/2022.06.16.496480.

109. Ting, J.T., Daigle, T.L., Chen, Q., and Feng, G. (2014). Acute Brain Slice Methods for Adult and Aging Animals: Application of Targeted Patch Clamp Analysis and Optogenetics. In (Humana Press, New York, NY), pp. 221–242. https://doi.org/10.1007/978-1-4939-1096-0_14.

110. Krishnaswami, S.R., Grindberg, R.V., Novotny, M., Venepally, P., Lacar, B., Bhutani, K., Linker, S.B., Pham, S., Erwin, J.A., Miller, J.A., et al. (2016). Using single nuclei for RNA-

seq to capture the transcriptome of postmortem neurons. Nat. Protoc. *11*, 499–524. https://doi.org/10/f8d3qc.

111. Pnevmatikakis, E.A., and Giovannucci, A. (2017). NoRMCorre: An online algorithm for piecewise rigid motion correction of calcium imaging data. J. Neurosci. Methods *291*, 83–94. https://doi.org/10.1016/j.jneumeth.2017.07.031.

112. Pnevmatikakis, E.A., Soudry, D., Gao, Y., Machado, T.A., Merel, J., Pfau, D., Reardon, T., Mu, Y., Lacefield, C., Yang, W., et al. (2016). Simultaneous Denoising, Deconvolution, and Demixing of Calcium Imaging Data. Neuron *89*, 285–299. https://doi.org/10.1016/j.neuron.2015.11.037.

113. Giovannucci, A., Friedrich, J., Gunn, P., Kalfon, J., Brown, B.L., Koay, S.A., Taxidis, J., Najafi, F., Gauthier, J.L., Zhou, P., et al. (2019). CaImAn an open source tool for scalable calcium imaging data analysis. eLife *8*, e38173. https://doi.org/10.7554/eLife.38173.

114. Bechtold, B., Fletcher, P., seamusholden, and Gorur-Shandilya, S. (2021). bastibe/Violinplot-Matlab: A Good Starting Point. Version v0.1 (Zenodo). https://doi.org/10.5281/zenodo.4559847 https://doi.org/10.5281/zenodo.4559847.

115. Butler, A., Hoffman, P., Smibert, P., Papalexi, E., and Satija, R. (2018). Integrating single-cell transcriptomic data across different conditions, technologies, and species. Nat. Biotechnol. *36*, 411–420. https://doi.org/10/gc87v6.

116. Hao, Y., Hao, S., Andersen-Nissen, E., Mauck, W.M., Zheng, S., Butler, A., Lee, M.J., Wilk, A.J., Darby, C., Zager, M., et al. (2021). Integrated analysis of multimodal single-cell data. Cell *184*, 3573-3587.e29. https://doi.org/10.1016/j.cell.2021.04.048.

117. Satija, R., Farrell, J.A., Gennert, D., Schier, A.F., and Regev, A. (2015). Spatial reconstruction of single-cell gene expression data. Nat. Biotechnol. *33*, 495–502. https://doi.org/10.1038/NBT.3192.

118. Stuart, T., Butler, A., Hoffman, P., Hafemeister, C., Papalexi, E., Mauck, W.M., Hao, Y., Stoeckius, M., Smibert, P., and Satija, R. (2019). Comprehensive Integration of Single-Cell Data. Cell *177*, 1888-1902.e21. https://doi.org/10.1016/j.cell.2019.05.031.

119. Griffiths, J.A., Richard, A.C., Bach, K., Lun, A.T.L., and Marioni, J.C. (2018). Detection and removal of barcode swapping in single-cell RNA-seq data. Nat. Commun. *9*. https://doi.org/10/gdw373.

120. Lun, A.T.L., Riesenfeld, S., Andrews, T., Dao, T.P., Gomes, T., Marioni, J.C., and participants in the 1st Human Cell Atlas Jamboree (2019). EmptyDrops: distinguishing cells from empty droplets in droplet-based single-cell RNA sequencing data. Genome Biol. *20*, 63. https://doi.org/10/gfxdhf.

121. Germain, P.-L., Sonrel, A., and Robinson, M.D. (2020). pipeComp, a general framework for the evaluation of computational pipelines, reveals performant single cell RNA-seq preprocessing tools. Genome Biol. *21*, 227. https://doi.org/10/ghb3tq.

122. Germain, P.-L., and Lun, A. (2021). scDblFinder: scDblFinder. Version 1.4.0 (Bioconductor version: Release (3.12)). https://doi.org/10.18129/B9.bioc.scDblFinder https://doi.org/10.18129/B9.bioc.scDblFinder.

123. McGinnis, C.S., Murrow, L.M., and Gartner, Z.J. (2019). DoubletFinder: Doublet Detection in Single-Cell RNA Sequencing Data Using Artificial Nearest Neighbors. Cell Syst. *8*, 329-337.e4. https://doi.org/10/gg5m57.

124. McCarthy, D.J., Campbell, K.R., Lun, A.T.L., Wills, Q.F., and Hofacker, I. (2017). Scater: pre-processing, quality control, normalization and visualization of single-cell RNA-seq data in R. Bioinformatics *33*, btw777. https://doi.org/10/gfgp3m.

125. Choudhary, S., and Satija, R. (2022). Comparison and evaluation of statistical error models for scRNA-seq. Genome Biol. *23*, 27. https://doi.org/10.1186/s13059-021-02584-9.

126. Hafemeister, C., and Satija, R. (2019). Normalization and variance stabilization of single-cell RNA-seq data using regularized negative binomial regression. Genome Biol. *20*, 296. https://doi.org/10.1186/s13059-019-1874-1.

127. Jolliffe, I.T., and Cadima, J. (2016). Principal component analysis: a review and recent developments. Philos. Trans. R. Soc. Math. Phys. Eng. Sci. *374*, 20150202. https://doi.org/10.1098/rsta.2015.0202.

128. Becht, E., McInnes, L., Healy, J., Dutertre, C.-A., Kwok, I.W.H., Ng, L.G., Ginhoux, F., and Newell, E.W. (2019). Dimensionality reduction for visualizing single-cell data using UMAP. Nat. Biotechnol. *37*, 38–44. https://doi.org/10.1038/nbt.4314.

129. McInnes, L., Healy, J., and Melville, J. (2018). UMAP: Uniform Manifold Approximation and Projection for Dimension Reduction. ArXiv180203426 Cs Stat.

130. Maaten, L. van der, and Hinton, G. (2008). Visualizing Data using t-SNE. J. Mach. Learn. Res. *9*, 2579–2605.

131. Traag, V.A., Waltman, L., and van Eck, N.J. (2019). From Louvain to Leiden: guaranteeing well-connected communities. Sci. Rep. *9*, 5233. https://doi.org/10.1038/s41598-019-41695-z.

132. Zappia, L., and Oshlack, A. (2018). Clustering trees: a visualization for evaluating clusterings at multiple resolutions. GigaScience *7*, giy083. https://doi.org/10.1093/gigascience/giy083.

133. Phipson, B., Sim, C.B., Porrello, E.R., Hewitt, A.W., Powell, J., and Oshlack, A. (2022). propeller: testing for differences in cell type proportions in single cell data. Bioinformatics *38*, 4720–4726. https://doi.org/10.1093/bioinformatics/btac582.

134. Squair, J.W., Gautier, M., Kathe, C., Anderson, M.A., James, N.D., Hutson, T.H., Hudelle, R., Qaiser, T., Matson, K.J.E., Barraud, Q., et al. (2021). Confronting false discoveries in single-cell differential expression. Nat. Commun. *12*, 5692. https://doi.org/10.1038/s41467-021-25960-2.

135. Costantini, D. (2020). Neuronal Topography in a Cortical Circuit for Innate Odor Valence. https://doi.org/10.7916/d8-ryea-m313.

136. Klein, S., Staring, M., Murphy, K., Viergever, M.A., and Pluim, J.P.W. (2010). elastix: a toolbox for intensity-based medical image registration. IEEE Trans. Med. Imaging *29*, 196–205. https://doi.org/10.1109/TMI.2009.2035616.

137. Shamonin, D.P., Bron, E.E., Lelieveldt, B.P.F., Smits, M., Klein, S., Staring, M., and Alzheimer's Disease Neuroimaging Initiative (2013). Fast parallel image registration on CPU and GPU for diagnostic classification of Alzheimer's disease. Front. Neuroinformatics *7*, 50. https://doi.org/10.3389/fninf.2013.00050.

138. Schindelin, J., Arganda-Carreras, I., Frise, E., Kaynig, V., Longair, M., Pietzsch, T., Preibisch, S., Rueden, C., Saalfeld, S., Schmid, B., et al. (2012). Fiji: an open-source platform for biological-image analysis. Nat. Methods *9*, 676–682. https://doi.org/10.1038/nmeth.2019.

139. Carpenter, A.E., Jones, T.R., Lamprecht, M.R., Clarke, C., Kang, I.H., Friman, O., Guertin, D.A., Chang, J.H., Lindquist, R.A., Moffat, J., et al. (2006). CellProfiler: image analysis software for identifying and quantifying cell phenotypes. Genome Biol. *7*, R100. https://doi.org/10.1186/gb-2006-7-10-r100.

140. McCullough, K.M., Morrison, F.G., Hartmann, J., Carlezon, W.A., and Ressler, K.J. (2018). Quantified Coexpression Analysis of Central Amygdala Subpopulations. eNeuro *5*. https://doi.org/10.1523/ENEURO.0010-18.2018.

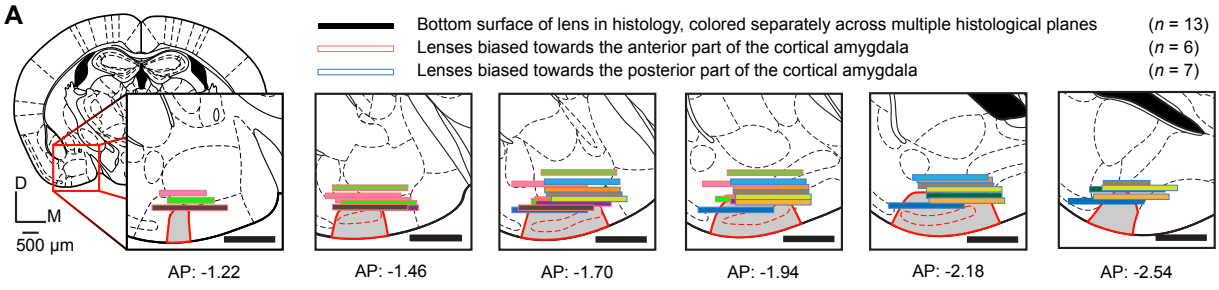

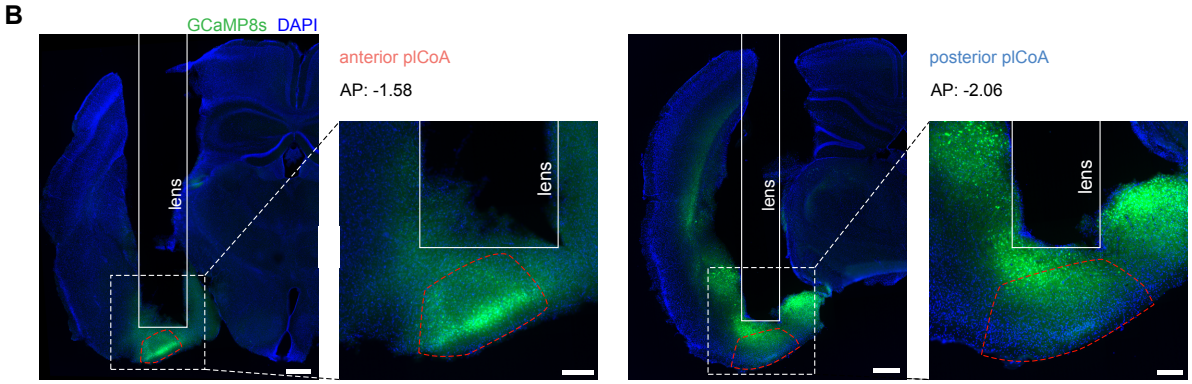

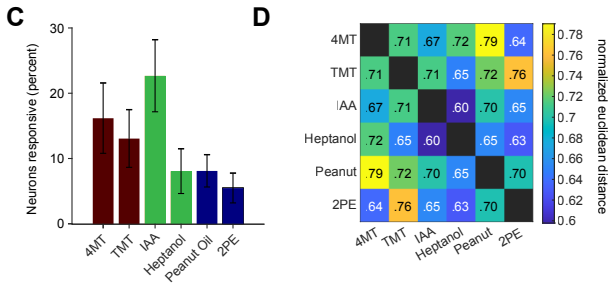

Figure S1. Additional information for imaging experiments. Related to **Figure 2.**

(A) Histologically verified placements for GRIN lenses (bars) in wild type animals infected with AAV-hSyn-GCaMP8s for calcium imaging experiments. Horizontal lines indicate locations where lens placements were visible in coronal sections at various positions in the plCoA anterior-posterior axis. Different color bars represent placements in each of 13 animals. Those scored as anterior are outlined in red, and those in posterior are outlined in blue.
(B) Histology for anterior plCoA (left) and posterior plCoA (right) lens implant and jGCaMP8s (green) viral injection sites in representative animals. Scale bar for full size images, 500 μm; scale bar for magnified images, 200 μm.
(C) Proportion responsive to each odor, pooled across regions.
(D) Heatmap of the normalized average pairwise Euclidean distance of odor response vectors across biological replicates.

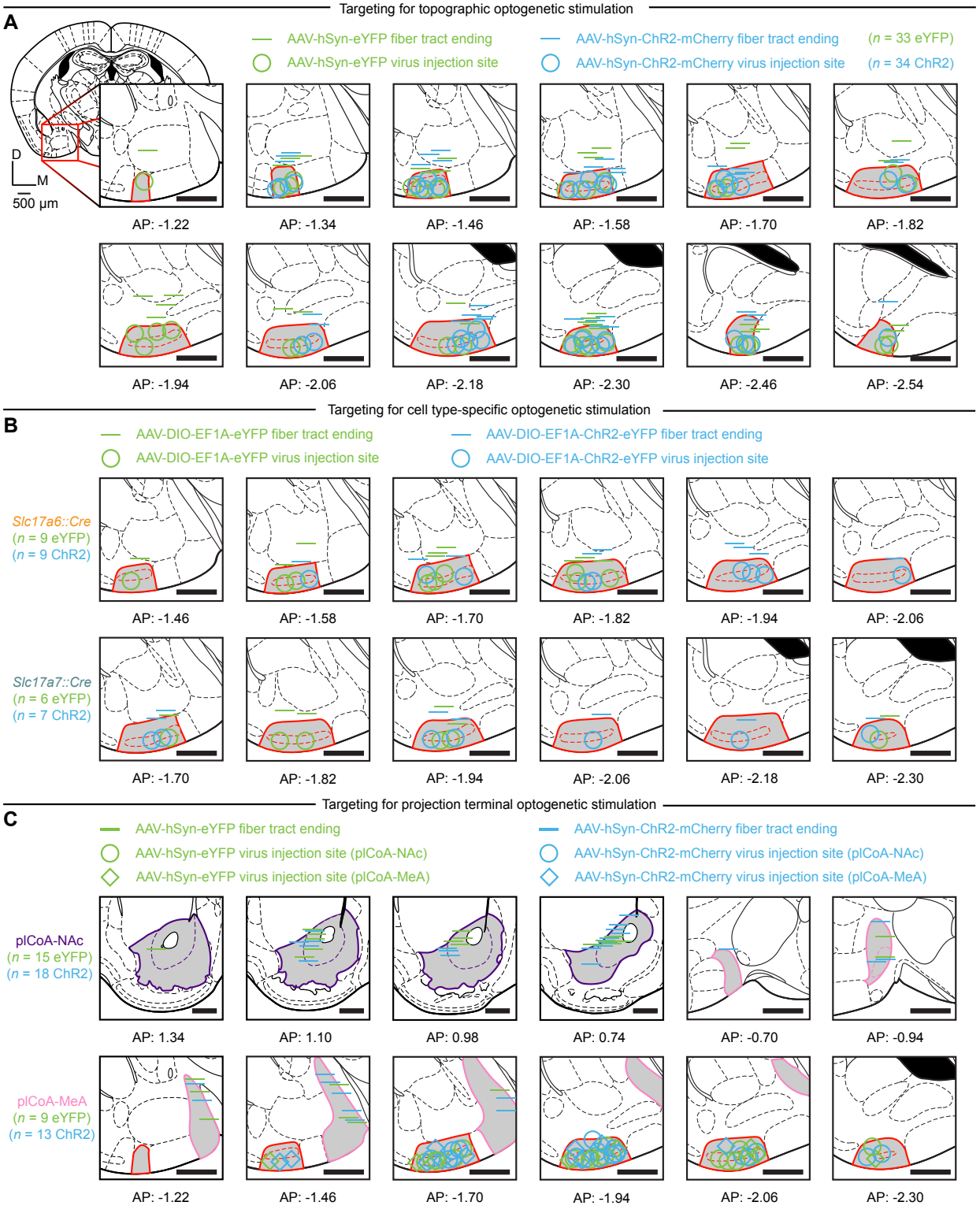

Fig. S2. Targeting of plCoA neurons for optogenetic stimulation. Related to **Figures 2**, **5**, **7**, **S3**, and **S8**.

(**A**) Histologically verified placements for optic fiber implants (bars) and viral injection sites (circles) in wild type animals infected with AAV-hSyn-ChR2-mCherry (blue) or AAV-hSyn-eYFP (green) in topographic optogenetic cell body stimulation experiments in **Figure 1** and **S2**.
(**B**) Same as (**A**), but for cell-type specific optogenetic cell body stimulation experiments for *Slc17a7::Cre* (top) and *Slc17a6::Cre* (bottom) animals infected with AAV-DIO-EF1A-ChR2-eYFP (blue) or AAV-EF1A-DIO-eYFP (green) in **Figure 5**.
(**C**) Respective placements for fiber implants (bars) and injection sites (plCoA-NAc, circles; plCoA-MeA, diamonds) in wild-type animals infected with AAV-hSyn-ChR2-mCherry (blue) or AAV-hSyn-eYFP (green) in projection-specific optogenetic axon terminal stimulation experiments in **Figure 7** and **S8.**
n denotes number of mice per group batched across 4-quad, elevated plus maze, and open field test experiments, exceeding *n* values for individual experiments due to behavioral cohort design (see STAR Methods). Relevant regions are highlighted in grey and outlined: plCoA (red), NAc (purple, only in **C**), and MeA (pink, only in **C**). All mouse brain sections reproduced from Paxinos and Franklin, 5th Edition, and numbers below all images denote its anterior-posterior distance from bregma in this atlas.[36] All scale bars, 500 μm.

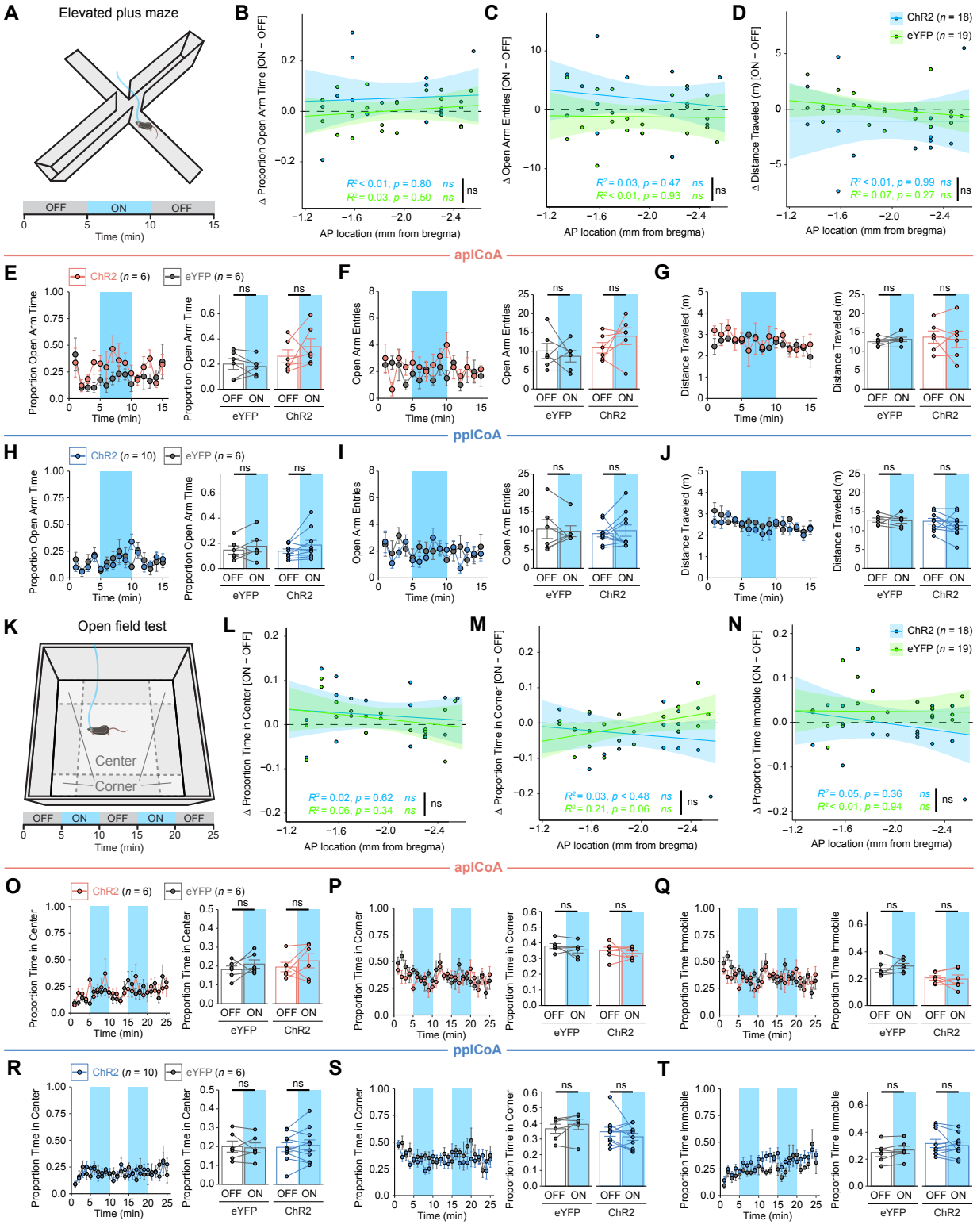

Fig. S3. Behavioral effects of topographic plCoA stimulation are limited to valence alone. Related to **Figure 2**.

(A) Behavioral paradigm for optogenetic stimulation in the open field test.
(B-D) Optogenetic stimulation-induced change in time spent (**B**) and number of entries (**C**) into the open arms, as well as distance traveled (**D**) in the elevated plus maze is not correlated to anteroposterior axis position in plCoA.
(E-G) Effects of optogenetic stimulation of aplCoA neurons in the elevated plus maze in 1 minute bins over time (left) and during off and on periods (right).Photostimulation of aplCoA neurons does not induce a significant change in time spent (**E**) and number of entries (**F**) into the open arms, as well as distance traveled (**G**) in the elevated plus maze.
(H-J) Effects of optogenetic stimulation of pplCoA neurons in the elevated plus maze in 1minute bins over time (left) and during off and on periods (right). Photostimulation of pplCoA neurons does not induce a significant change in time spent (**H**) and number of entries (**I**) into the open arms, as well as distance traveled (**J**) in the elevated plus maze.
(K) Behavioral paradigm for optogenetic stimulation in the open field test.
(L-N) Optogenetic stimulation-induced change in time spent in the center (**L**) and corners (**M**), as well as distance traveled (**N**) in the open field test is not correlated to anteroposterior axis position in plCoA.
(O-Q) Effects of optogenetic stimulation of aplCoA neurons in the open field test in 1 mintue time bins (left) and during off and on periods (right). Photostimulation of aplCoA neurons does not induce a significant change time spent in the center (**O**) and corners (**P**), as well as distance traveled (**Q**) in the open field test.
(R-T) Effects of optogenetic stimulation of pplCoA neurons in the open field test in 1 minute time bins (left) and during off and on periods (right). Photostimulation of pplCoA neurons does not induce a significant change time spent in the center (**R**) and corners (**S**), as well as distance traveled (**T**) in the open field test.
All “ON” and “OFF” comparisons in bar graphs and linear regressions are on a per 5-minute basis. **(B-D, L-M)** Least-squares linear regression ± 95% confidence interval. Across panels: ns, not significant. Additional specific details of statistical tests can be found in Supplemental Table 1.

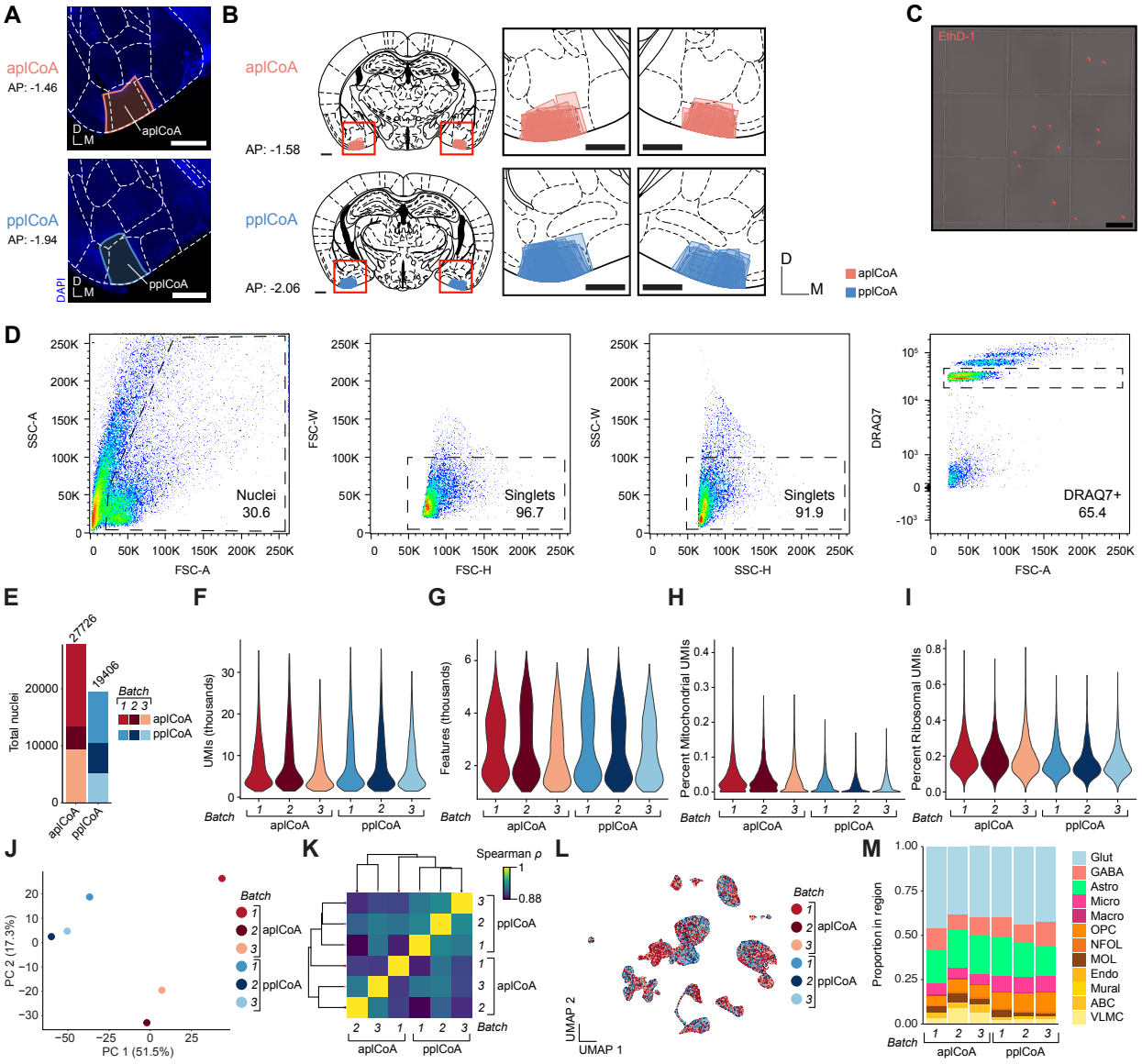

Fig. S4. Additional information and quality-control for single-nucleus sequencing experiments. Related to **Figure 3**.

(A) Representative images of tissue microdissection sites from aplCoA and pplCoA following extraction and DAPI staining (blue). Scale bars, 500 µm.
(B) Location of all tissue sample sites for used for snRNA-seq, color coded by plCoA zone (n = 3 pools per zone, 4-11 sections per pool). Scale bars, 500 µm.
(C) Validation of nuclear enrichment after FANS. Ethidium homodimer-1 (EthD-1, red) labels nuclei on a hemocytometer after sorting, with an absence of non-nuclear, EthD-1-negative debris. Scale bar, 100 µm.
(D) Common gating strategy for FANS sorts for snRNA-seq in a representative sample.[102] Far left, morphology gate on forward and side scatter area excludes likely debris. Middle left, forward scatter gate excludes nuclear doublets with high forward scatter width. Middle right, side scatter gate excludes nuclear multiplets with high side scatter width. Far right, stoichiometric DRAQ7+ fluorescence allows enrichment of single nuclei and exclusion of debris and multiplets.
(E) Absolute number and proportion of snRNA-seq nuclei passing quality control filters from each replicate in each plCoA zone (n = 27,726 in aplCoA, 19,406 in pplCoA, 3 libraries/batches each).
(F) Violin plot of UMIs detected per snRNA-seq nucleus for each replicate, filtered at the median per library + five times the median absolute deviation within each library (median 6081 UMIs/nucleus).
(G) Violin plot of genes detected per nucleus from each replicate, filtered at a minimum of 1000 features per nucleus (median 2547 genes/nucleus).
(H) Percent mitochondrial gene UMIs per snRNA-seq nucleus, filtered at median + five times the median absolute deviation per library (median 0.02% mitochondrial UMIs/nucleus).
(I) Percent ribosomal gene UMIs per snRNA-seq nucleus, filtered at median + five times the median absolute deviation per library (median 0.17% ribosomal UMIs/nucleus).
(J) Principal component analysis of pseudobulk snRNA-seq samples created from each batch, colored based on their combination of zone and batch identity.
(K) Evaluation of transcriptomic homology between batches, where the distance matrix is based on Spearman correlation between median expression of highly variable features for the whole dataset, and the dendrogram was created via hierarchical clustering of batches on this correlation matrix.
(L) UMAP of all snRNA-seq nuclei colored by both target region and batch identity.
(M) Relative proportion of nuclei of each type for all snRNA-seq batches.
Brain diagrams were reproduced from Paxinos and Franklin (2005).[36]

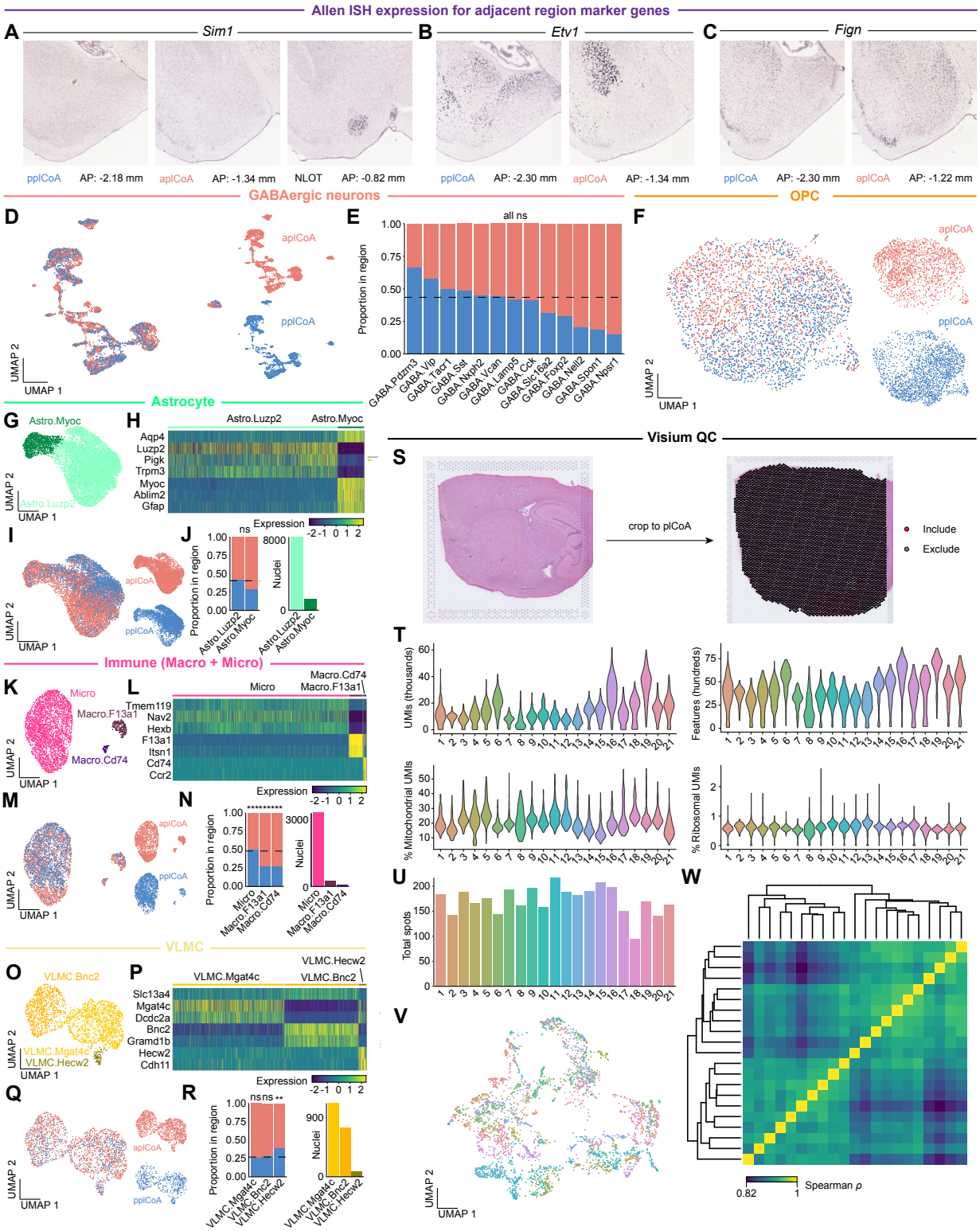

Fig. S5. Additional information and quality control for spatial gene expression. Related to **Figure 4**.

(**A-C**) Allen ISH data for marker genes from molecular cell types adjacent to, but not within plCoA. *Sim1* (**A**) marks cells in the NLOT, *Etv1* (**B**) marks cells in the BLA and posterior basomedial amygdala, and *Fign* (**C**) marks cells in the cortex-amygdalar transition area, but none of these mark cells in the plCoA.
(**D**) UMAP of all plCoA GABAergic neurons, colored by domain of origin.
(**E**) Relative proportion of molecular subtype nuclei from each domain within GABAergic neurons. Dotted line indicates chance level for plCoA GABAergic neuron nuclei.
(**F**) UMAP of all plCoA OPCs, colored by domain of origin.
(**G**) Two-dimensional UMAP of astrocytes, colored by molecular cell type.
(**H**) Heatmap of astrocyte subtype marker genes.
(**I**) UMAP of all plCoA astrocytes, colored by domain of origin.
(**J**) Left, relative proportion of molecular subtype nuclei from each domain within astrocytes. Dotted line indicates chance level for plCoA astrocyte nuclei. Right, relative abundance of each astrocyte subtype within plCoA.
(**K**) Two-dimensional UMAP of immune cells, colored by molecular cell type.
(**L**) Heatmap of immune cell subtype marker genes.
(**M**) UMAP of all plCoA immune cells, colored by domain of origin.
(**N**) Left, relative proportion of molecular subtype nuclei from each domain within immune cells. Dotted line indicates chance level for plCoA immune cell nuclei. Right, relative abundance of each immune cell type within plCoA.
(**O**) Two-dimensional UMAP of VLMC nuclei, colored by molecular cell type.
(**P**) Heatmap of VLMC subtype marker genes.
(**Q**) UMAP of all plCoA VLMC nuclei, colored by domain of origin.
(**R**) Left, relative proportion of molecular subtype nuclei from each domain within VLMCs. Dotted line indicates chance level for plCoA VLMC nuclei. Right, relative abundance of each VLMC subtype within plCoA.
(**S**) Left, representative section on a Visium slide capture area stained with hematoxylin and eosin. Right, representative section with capture spots overlaid (grey) and plCoA-overlapping spots highlighted (red).
(**T**) Violin plots of quality metrics for individual Visium sections on a per-spot basis in plCoA-overlapping spots (N = 21 sections). Upper left, UMIs per spot; upper right, features per spot; lower left, proportion mitochondrial UMIs per spot; lower right, proportion ribosomal UMIs per spot.
(**U**) Number of plCoA-overlapping capture spots per section (n = 3,616 total spots).
(**V**) Two-dimensional UMAP of all plCoA-overlapping capture spots, colored by section of origin.
(**W**) Evaluation of transcriptomic homology between sections, where the distance matrix is based on Spearman correlation between median expression of highly variable features for the whole dataset, and the dendrogram was created via hierarchical clustering of sections on this correlation matrix.
Across panels: ** $p < 0.01$; *** $p < 0.001$; ns, not significant. Additional specific details of statistical tests can be found in Supplemental Table 1.

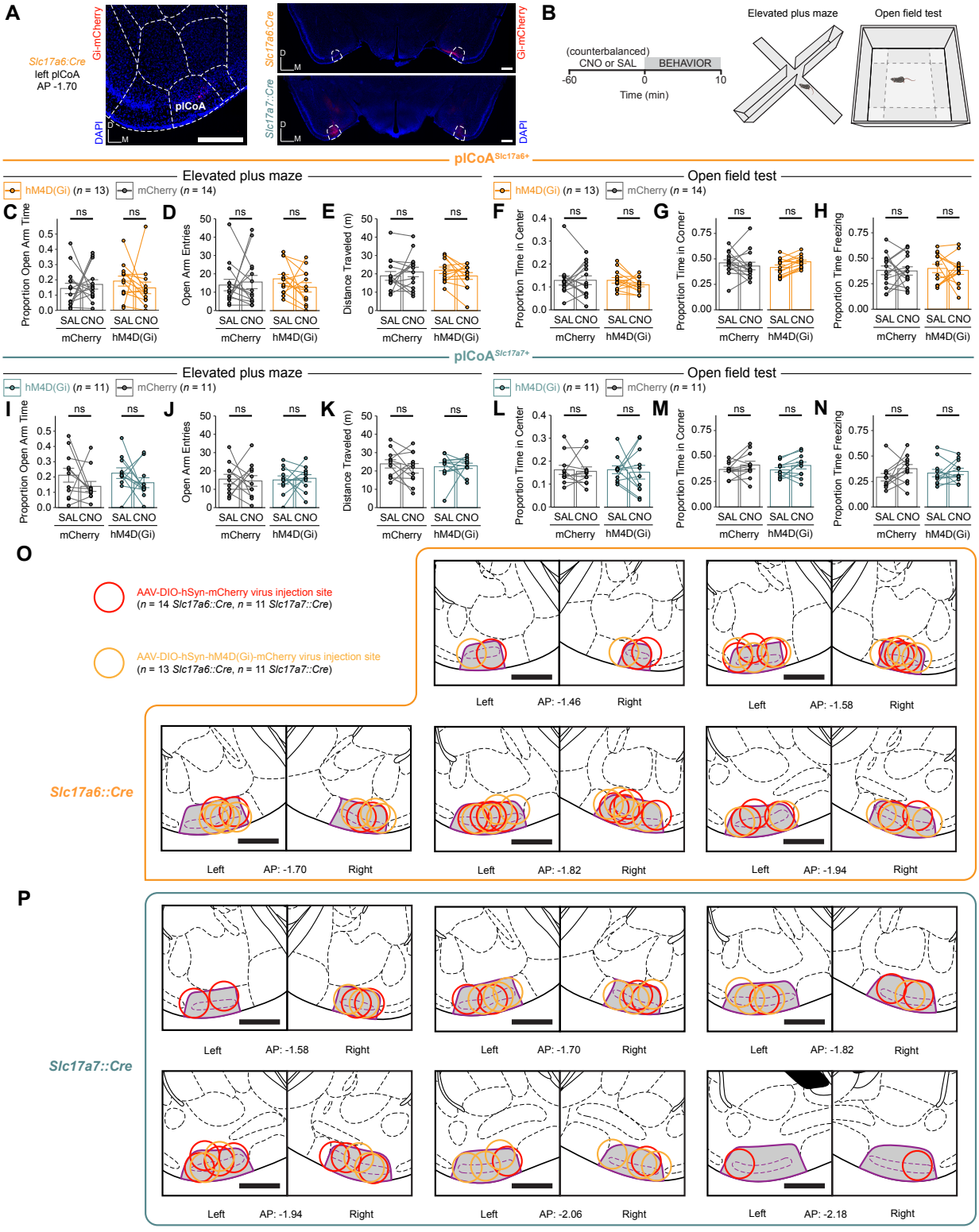

Fig. S6. Additional information for Cre-dependent molecularly targeted chemogenetic inhibition experiments. Related to **Figure 5**.

(A) Representative histology for inhibition experiments for AAV-hM4D(Gi)-mCherry-infected *Slc17a6::Cre* (left) or *Slc17a7::Cre* (right) animals.
(**B**) Strategy for chemogenetic inhibition in the open field test and elevated plus maze.
(C-E) Effect of chemogenetic inhibition of plCoA$^{Slc17a6+}$ neurons in the elevated plus maze. Inhibition does not induce a significant change in time spent (**C**) or number of entries (**D**) into the open arms, as well as distance traveled (**E**) in the elevated plus maze.
(F-H) Effect of chemogenetic inhibition of plCoA$^{Slc17a6+}$ neurons in the open field test. Inhibition does not induce a significant change in time spent in the center (**F**) or corners (**G**), as well as distance traveled (**H**) in the open field test.
(I-K) Effect of chemogenetic inhibition of plCoA$^{Slc17a7+}$ neurons in the elevated plus maze. Inhibition does not induce a significant change in time spent (**I**) and number of entries (**J**) into the open arms, as well as distance traveled (**K**) in the elevated plus maze.
(L-N) Effect of chemogenetic inhibition of plCoA$^{Slc17a7+}$ neurons in the open field test. Inhibition does not induce a significant change in time spent in the center (**L**) or corners (**M**), as well as distance traveled (**N**) in the open field test.
(**O**) Histologically verified placements for viral injection sites in *Slc17a6::Cre* animals infected with AAV-DIO-hSyn-mCherry (red) or AAV-DIO-hSyn-hM4D(Gi) (light orange) in molecularly targeted chemogenetic inhibition experiments.
(**P**) Same as (**O**), but in *Slc17a7::Cre* animals.
n denotes number of mice per group batched across 4-quad, elevated plus maze, and open field test experiments, exceeding *n* values for individual experiments due to behavioral cohort design (see STAR Methods). All mouse brain sections reproduced from Paxinos and Franklin, 5th Edition, with plCoA highlighted in grey and outlined in purple, and numbers below all images denote its anterior-posterior distance from bregma in this atlas.[36] All scale bars, 500 μm. Across panels: ns, not significant. Additional specific details of statistical tests can be found in Supplemental Table 1.

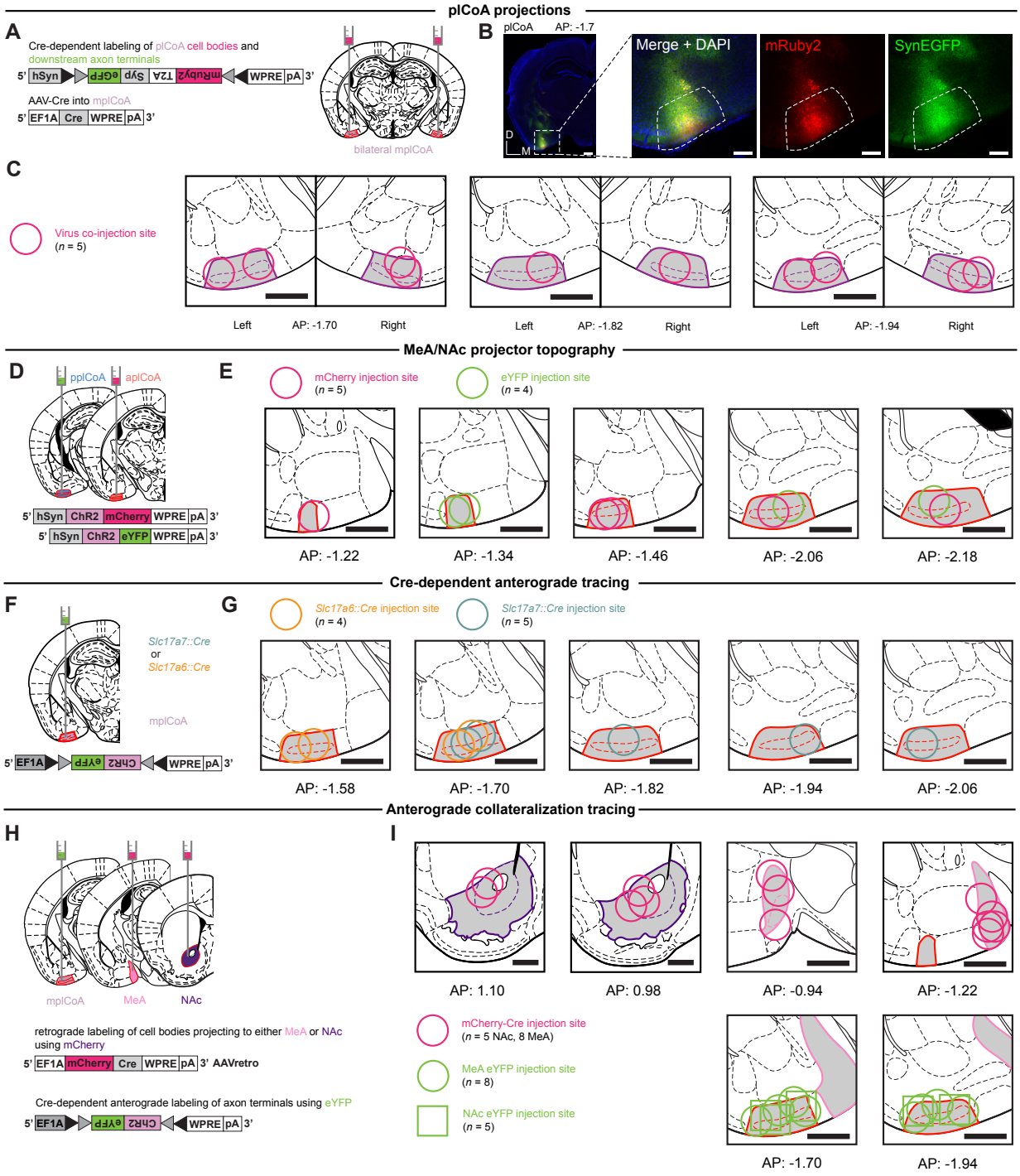

Fig. S7. Additional information for plCoA anterograde tracing experiments. Related to **Figure 6**.

(A) Schematic for general anterograde output mapping strategy, where a virus labeling cell bodies in plCoA with mRuby and presynaptic terminals in downstream regions with synaptophysin-bound eYFP.
(B) Histological image of plCoA injection site in a representative animal. Scale bar, 200 µm.
(C) Histologically verified placements for viral injection sites in initial anterograde tracing experiments.
(D) Schematic for dual-color topographic anterograde tracing: two counterbalanced fluorophores were injected into aplCoA and pplCoA, and each color was quantified in major projection targets of plCoA.
(E) Histologically verified placements for viral injection sites in dual-color anterograde tracing experiments.
(F) Schematic for Cre-dependent anterograde output mapping strategy: a Cre-dependent virus expressing eYFP was injected into either an *Slc17a6::Cre* or *Slc17a7::Cre* animal to determine relative output enrichment for either broad cell type.
(G) Histologically verified placements for viral injection sites in Cre-dependent molecular anterograde tracing experiments.
(H) Schematic of anterograde viral strategy to explore collateralization of plCoA MeA and NAc projection neurons to other regions.
(I) Histologically verified placements for viral injection sites in collateralization experiments. Relevant regions are highlighted in grey and outlined: plCoA (red), NAc (purple, only in **I**), and MeA (pink, only in **I**). All mouse brain sections reproduced from Paxinos and Franklin, 5th Edition, and numbers below all images denote its anterior-posterior distance from bregma in this atlas.[36] All scale bars 500 µm unless noted elsewhere.

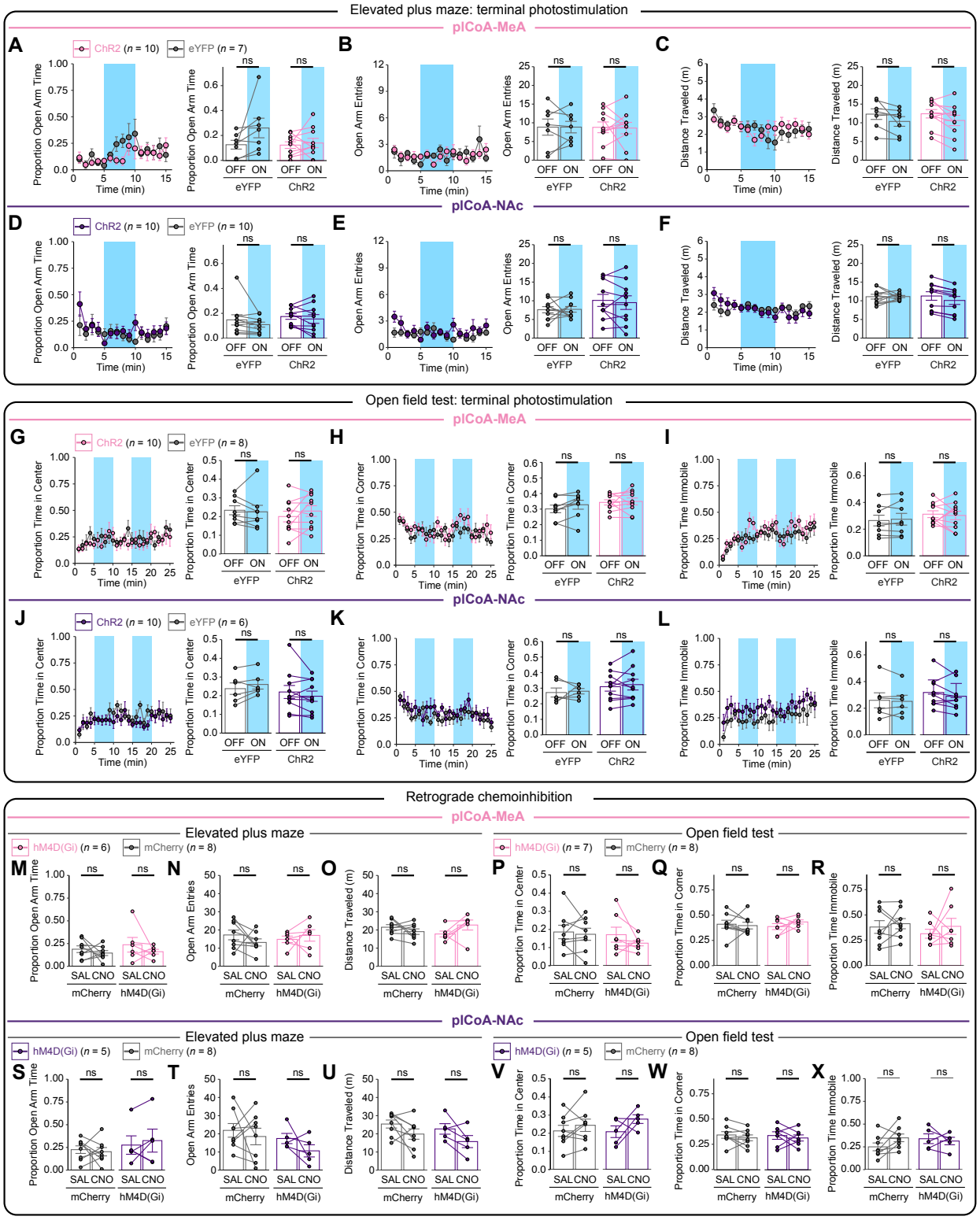

Fig. S8. Manipulation of plCoA projections to MeA or NAc in either direction does not change features of behavior unrelated to innate valence. Related to **Figure 7**.

(A-C) Effects of optogenetic stimulation of plCoA terminals in MeA in the elevated plus maze in time bins of 1 minute (left) and during off and on periods (right). Photostimulation does not induce a significant change in time spent (**A**) and number of entries (**B**) into the open arms, as well as distance traveled (**C**) in the elevated plus maze.
(D-F) Effects of optogenetic stimulation of plCoA terminals in NAc in the elevated plus maze in time bins of 1 minute (left) and during off and on periods (right). Photostimulation does not induce a significant change in time spent (**H**) and number of entries (**I**) into the open arms, as well as distance traveled (**J**) in the elevated plus maze.
(G-I) Effects of optogenetic stimulation of plCoA terminals in MeA in the open field test in time bins of 1 minute (left) and during off and on periods (right). Photostimulation does not induce a significant change time spent in the center (**G**) and corners (**H**), as well as distance traveled (**I**) in the open field test.
(J-L) Effects of optogenetic stimulation of plCoA terminals in NAc in the open field test in time bins of 1 minute (left) and during off and on periods (right). Photostimulation does not induce a significant change time spent in the center (**G**) and corners (**H**), as well as distance traveled (**I**) in the open field test.
(**M-O**) Effects of chemogenetic inhibition of plCoA-MeA projection neurons in the elevated plus maze. Inhibition does not induce a significant change in time spent (**M**) and number of entries (**N**) into the open arms, as well as distance traveled (**O**) in the elevated plus maze.
(**P-R**) Effects of chemogenetic inhibition of plCoA-MeA projection neurons in the open field test. Inhibition does not induce a significant change in time spent in the center (**P**) and corners (**Q**), as well as distance traveled (**R**) in the open field test.
(**S-U**) Effects of chemogenetic inhibition of plCoA-NAc projection neurons in the elevated plus maze. Inhibition does not induce a significant change in time spent (**S**) and number of entries (**T**) into the open arms, as well as distance traveled (**U**) in the elevated plus maze.
(**V-X**) Effects of chemogenetic inhibition of plCoA-NAc projection neurons in the open field test. Inhibition does not induce a significant change in time spent in the center (**V**) and corners (**W**), as well as distance traveled (**X**) in the open field test.
Across panels: ns, not significant. Additional specific details of statistical tests can be found in Supplemental Table 1.